NUMERICAL RELATIVITY STUDIES IN BLACK HOLE ASTROPHYSICS

A Dissertation
Presented to
The Academic Faculty

By

Christopher William Evans

In Partial Fulfillment
of the Requirements for the Degree
Doctor of Philosophy in the
School of Physics

Georgia Institute of Technology

December 2021

NUMERICAL RELATIVITY STUDIES IN BLACK HOLE ASTROPHYSICS

Thesis committee:

Tamara Bogdanović
School of Physics
Georgia Institute of Technology

Deirdre Shoemaker
Department of Physics
The University of Texas at Austin

Pablo Laguna
Department of Physics
The University of Texas at Austin

Laura Cadonati
School of Physics
Georgia Institute of Technology

Gongjie Li
School of Physics
Georgia Institute of Technology

Date approved: August 27, 2021

To Karissa and Woordow,

for their endless love and support.

ACKNOWLEDGMENTS

I would like to Pablo Laguna for his unending support, guidance, and mentorship over the last eight years. The work in this thesis would not have been possible if not for his enthusiasm for the field and his unrivaled ability to share it with his students. I would also like to thank Deirdre Shoemaker, who has not only been a an unparalleled academic resource, but has also mentored me as if I were her own student. I want thank Tamara Bogdanović who has been an endless source of guidance and encouragement as my advisor over the last year, and as a trusted mentor long before that.

I extend a special thanks to my friends and colleagues Bhavesh Khamesra, Deborah Ferguson, Miguel Gracia, Karan Jani, Juan Calderón Bustillo, Michael Clark, and Matt Kinsey, who have all been great partners for pursuing new ideas.

Finally, I would like to extend my deepest thanks to Karissa, Woodrow, Mom, Dad, Steve, Kitty, and all of my family members for their unconditional love and support, without which I would have never made it this far.

TABLE OF CONTENTS

LIST OF TABLES

LIST OF FIGURES

SUMMARY

Black holes have long fascinated both physicists and the general population alike. In an astrophysical context, black holes participate in interesting interactions with not only stars, but also other black holes. Moreover, the recent detections of gravitational waves from both black hole-black hole and black hole-neutron star systems have only served to amplify excitement in the field of black hole astrophysics. Over the last few decades, numerical relativity has come to be a versatile tool for studying both of these classes of encounter. In this thesis, I present a collection of numerical relativity studies of black holes in the context of binary black hole mergers and tidal disruption events.

CHAPTER 1
INTRODUCTION

Ever since they were established as a generic prediction of general relativity (GR) in the 1960s, black holes (BHs) have remained at the forefront of astrophysical research. Through their interactions with each other and with stars, BHs have the capability to produce a wide variety of highly unique observable events. An example of this is the merger of a binary black hole (BBH) system, which (in isolation) is not observable electromagnetically because no matter is evolved. Instead, such events are only observable through gravitational waves (GWs), which have the ability to shed light on not only the strong-field regime of GR, but also details about the astrophysical population of BHs.

Beyond just BBH mergers, events that involve the interaction of a BH and a star have the capability to produce both GWs and electromagnetic (EM) radiation. Such events can be used to study not only the BHs, but also the stars themselves. For example, GWs from the merger of a BH and a neutron star have the potential to provide insight into the the equation of state for neutron stars and more broadly the nucleosynthesis of heavy elements in the universe. Though less exotic, tidal disruptions of main-sequence stars by supermassive ($\gtrsim 10^6\ M_\odot$) BHs can not only shed light on the internal structure of the stars, but also have the potential to be one of the only viable tools to probe the population demographics of BHs in nearby galaxies.

In recent years, interest in the field has even further intensified with the successful detection GWs by Advanced Laser Interferometer Gravitational-Wave Observatory (LIGO) [1]. Through the first half of the third observing run (O3), the Advanced LIGO [1] and Advanced Virgo [2] observatories have reported a total of 50 GW detections as part of their Gravitational-Wave Transient Catalog (GWTC) [3, 4]. These catalog events (shown in Figure 1.1) include 46 confident BBH mergers [5, 6], two binary neutron star (BNS) mergers [7,

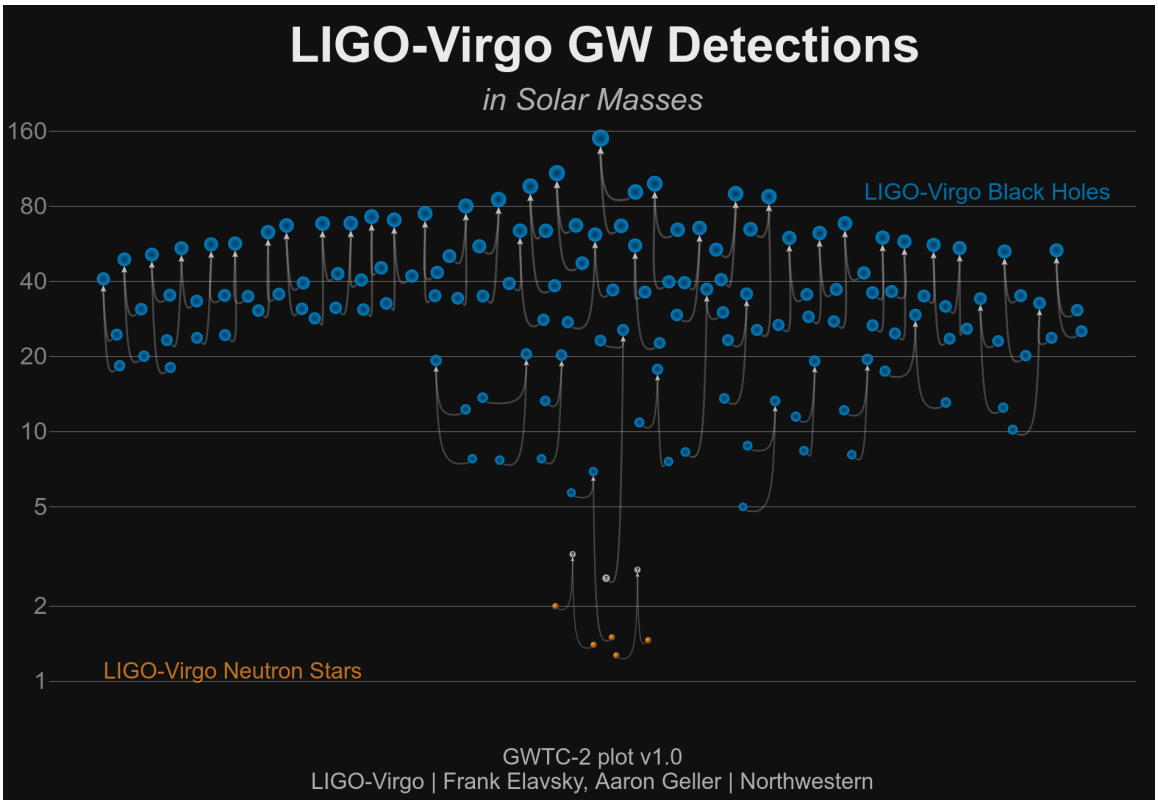

Figure 1.1: Source masses and classifications for the gravitational wave events reported in the Gravitational-Wave Transient Catalog. Image credit: LIGO-Virgo, Northwestern, Frank Elavsky, Aaron Geller.

8], and two potential neutron star black hole mergers [9]. Additionally, the LIGO Scientific Collaboration announced the detection of two separate confirmed neutron star black hole events during the second half of O3 [10]. Over the next two decades, our ability to detect GWs is expected to drastically improve with the addition of space-based (such as Laser Interferometer Space Antenna (LISA) [11]) and third generation ground-based detectors (Einstein Telescope [12] and Cosmic Explorer [13]) to the growing network of GW observatories.

In order to interpret the rapidly growing number of GW and EM observations of BH systems, researchers will need to draw upon a strong theoretical understanding of their dynamics. Unfortunately, relatively few analytical solutions to the Einstein field equations of GR are known. Even further, those solutions that are known to exist are generally not appropriate for use in dynamical systems like BBHs and tidal disruption events (TDEs).

Instead one must turn to the field of numerical relativity (NR), which is based on the idea of restating of Einstein's equations with the goal of making them more amenable to numerical evolution.

In this thesis, I describe a series of numerical relativity studies in black hole astrophysics. To begin, in the remaining sections of this chapter I describe the foundations of NR and the MAYA computational framework, which I use to perform these NR simulations.

Following this, in Part I I describe two studies that involve NR simulations of BBH systems. The first of these, presented in Chapter 2, focuses on the ultimate fate of the horizons of the two BHs that comprise the binary, and how they evolve after the merger takes place. In Chapter 3, I focus on the dynamics of the remnant BH horizon itself after merger and how they correlate to the spatial distribution of the resulting GW emission.

In Part II, I shift my attention to NR simulations of TDEs. To begin, in Chapter 4 I present a new initial data framework called BOOSTEDSTAR, which I have developed with the goal of simulating TDEs in mind. Using this new framework, in Chapter 5 I present the results of a study into the effects of stellar rotation in TDEs, and how it could potentially be a significant driver of tidal debris circularization.

1.1 Notation and conventions

As is common in NR, throughout this thesis I use geometric units with $G = c = 1$. For all numerical simulations, I have chosen units in which the total mass of the system is equal to unity $M = 1$. For BBH systems with masses m_1 and m_2, this means that $m_1 + m_2 = 1$ and the component masses of the binary can be expressed in terms of the mass ratio $q = m_1/m_2$. All TDE systems discussed have mass ratios of $m_h/m_* \geq 10^5$, so effectively $M \approx m_h \approx 1$.

Unless stated otherwise, Greek indices (such as μ, ν, ρ, σ, ...) denote full spacetime indices from 0 to 3, while Latin indices (such as i, j, k, l, ...) are spatial and range from 1 to 3. I take the signature of the spacetime metric to be $(-, +, +, +)$.

1.2 $3+1$ Numerical relativity

In the traditional formulation of GR, the spacetime metric

$$ds^2 = g_{\mu\nu}\, dx^\mu\, dx^\nu \tag{1.1}$$

is governed by the Einstein field equations

$$G_{\mu\nu} = R_{\mu\nu} - \frac{1}{2} R g_{\mu\nu} = 8\pi T_{\mu\nu}. \tag{1.2}$$

Here $T_{\mu\nu}$ is the *stress-energy tensor*, which encodes the matter content of the spacetime. The coupling of matter to the field equations will be discussed in Section 1.2.3.

This formulation is manifestly covariant, meaning that the field equations are stated entirely in terms of tensors and that time and space are placed on equal footing. While this property is fundamental to the ideas of GR, traditional numerical simulations involve the dynamical time evolution of some initial data that is specified at a given instant in time. This means that the field equations of Equation 1.2 must be adapted in some way in order to approach them with standard numerical methods.

The most common method to accomplish this in NR is the $3+1$ formalism, in which four dimensional spacetime is split into three spatial dimensions and one time dimension. Explicitly, consider a foliation of spacetime into spacelike hypersurfaces Σ_t (or *time slices*) with coordinates x^i that are labeled by a coordinate time parameter t. The coordinate or gauge freedom inherent to GR can be absorbed into two gauge functions: the lapse α and the shift vector β^i. The lapse function dictates the passage of proper time between adjacent time slices, while the shift vector determines how the coordinate system changes from one time slice Σ_t to the next $\Sigma_{t+\Delta t}$. Note that α and β^i are *freely specifiable* according to pure GR, since they encode the gauge choice.

With this foliation, the normal vector to a hypersurface Σ_t can be written as

$$n^\mu = \alpha^{-1} \left(t^\mu - \beta^\mu \right), \tag{1.3}$$

where $t^\mu = (\partial_t)^\mu$ is the tangent vector to lines of constant spatial coordinates x^i. One can then define the spatial metric γ_{ij} as the projection of $g_{\mu\nu}$ onto Σ_t:

$$\gamma_{\mu\nu} = g_{\mu\nu} + n_\mu n_\nu. \tag{1.4}$$

As is clear from this definition, γ_{ij} is just the projection operator onto Σ_t. Explicitly, $g_{\mu\nu}$ can be fully expressed in terms of α, β^i, and γ_{ij} as

$$ds^2 = g_{\mu\nu}\, dx^\mu\, dx^\nu = -\alpha^2\, dt^2 + \gamma_{ij} \left(dx^i + \beta^i\, dt \right) \left(dx^j + \beta^j\, dt \right). \tag{1.5}$$

In addition to the metric itself, the field equations of Equation 1.2 involve the curvature of spacetime through contractions of the Riemann tensor

$$R^\alpha{}_{\beta\mu\nu} = \partial_\mu \Gamma^\alpha{}_{\nu\beta} - \partial_\nu \Gamma^\alpha{}_{\mu\beta} + \Gamma^\alpha{}_{\mu\sigma} \Gamma^\sigma{}_{\nu\beta} - \Gamma^\alpha{}_{\nu\sigma} \Gamma^\sigma{}_{\mu\beta}\ , \tag{1.6}$$

where

$$\Gamma^\sigma{}_{\mu\nu} = \frac{1}{2} g^{\sigma\rho} \left(\partial_\mu g_{\nu\rho} + \partial_\nu g_{\mu\rho} - \partial_\rho g_{\mu\nu} \right) \tag{1.7}$$

are the Christoffel symbols. Under the $3+1$ formalism, there are two distinct contributions to the Riemann tensor: the *intrinsic* and *extrinsic* curvatures. The intrinsic curvature is fully specified by quantities on a single time slice and is simply given by the Riemann curvature tensor for the spatial metric ${}^{(3)}R^\alpha{}_{\beta\mu\nu}$. On the other hand, the extrinsic curvature K_{ij} is the result of how Σ_t is embedded in the full spacetime and must therefore depend on how γ_{ij} changes from one time slice to the next, or equivalently how it evolves in time. In terms of

the quantities defined above, the extrinsic curvature can be written as

$$K_{ij} = -\gamma_i^\alpha \gamma_j^\beta \nabla_\alpha n_\beta = -\frac{1}{2}\mathcal{L}_n \gamma_{ij}, \tag{1.8}$$

where $\mathcal{L}_n$ denotes the Lie derivative along the normal vector n^μ. To see that K_{ij} encodes the time evolution of γ_{ij}, one can expand this Lie derivative using Equation 1.3 to find

$$\partial_t \gamma_{ij} = -2\alpha K_{ij} + D_i \beta_j + D_j \beta_i, \tag{1.9}$$

where D_i is the covariant derivative associated with the spatial metric γ_{ij}.

1.2.1 Constraint and evolution equations

Under the $3+1$ formalism, it is convenient to explicitly decompose the Riemann tensor into intrinsic and extrinsic curvature contributions:

$$\gamma_\mu^\alpha \gamma_\nu^\beta \gamma_\rho^\delta \gamma_\sigma^\lambda R_{\alpha\beta\delta\lambda} = {}^{(3)}R_{\mu\nu\rho\sigma} + K_{\mu\rho}K_{\nu\sigma} - K_{\mu\sigma}K_{\nu\rho} \tag{1.10}$$

$$\gamma_\mu^\alpha \gamma_\nu^\beta \gamma_\rho^\delta n^\lambda R_{\alpha\beta\delta\lambda} = D_\nu K_{\mu\rho} - D_\mu K_{\nu\rho} \tag{1.11}$$

$$\gamma_\mu^\alpha \gamma_\nu^\beta n^\delta n^\lambda R_{\alpha\beta\delta\lambda} = \mathcal{L}_n K_{\mu\nu} + K_{\mu\delta}K_\nu^\delta + \alpha^{-1} D_\mu D_\nu \alpha. \tag{1.12}$$

Equations 1.10 and 1.11 are called the Gauss-Codazzi and Codazzi-Mainardi equations, respectively.

Note that the field equations Equation 1.2 have ten independent components, since $G_{\mu\nu}$ is a symmetric second rank tensor in four dimensional space. Using Equations 1.10 and 1.11, four of these components can be found by taking the contractions $n^\mu n^\nu G_{\mu\nu}$ and $\gamma^{\alpha\mu} n^\nu G_{\mu\nu}$ of the Einstein tensor and plugging the result into the field equations. These contractions

(respectively) result in the *constraint* equations

$$ {}^{(3)}R + K^2 - K_{ij}K^{ij} = 16\pi\rho_H \tag{1.13} $$

$$ D_j \left(K^{ij} - \gamma^{ij}K \right) = 8\pi S^i. \tag{1.14} $$

Here $\rho_H = n^\mu n^\nu T_{\mu\nu}$ and $S^i = -\gamma^{i\mu} n^\nu T_{\mu\nu}$ are the local energy and momentum densities as measured by Eulerian observers. Equations 1.13 and 1.14 are called the Hamiltonian and momentum constraints, respectively.

The constraint equations are so called because they do not involve any time derivatives. Instead, they are four equations (the Hamiltonian constraint and a component of the momentum constraint for each spatial direction) that must be satisfied by γ_{ij} and K_{ij} in order for the time slice to be part of a spacetime that satisfies the field equations. For this reason, the constraint equations lie at the heart of the initial data problem in NR; producing initial data for a NR simulation boils down to finding a solution to Equations 1.13 and 1.14 that models the desired physical system. Furthermore, any viable evolution system must conserve the constraint equations. Namely, if the initial data satisfies the constraints, then so should its time evolution.

Since α and β^i are freely specifiable, and with the evolution equation Equation 1.9 for γ_{ij} in hand, all that remains in order to fully describe the dynamics of GR is to find an evolution equation for K_{ij} from the field equations. This is in fact given by the remaining six components (ten less the four components used for the constraints) of the field equations. By expanding the Lie derivative in Equation 1.12 and using Equation 1.10, one can express the time evolution of K_{ij} as

$$ \begin{aligned} \partial_t K_{ij} = {} & \beta^k \partial_k K_{ij} + K_{li}\partial_j \beta^k + K_{kj}\partial_i \beta^k - D_i D_j \alpha \\ & + \alpha \left[{}^{(3)}R_{ij} + K K_{ij} - 2K_{ik}K^k_j \right] + 4\pi\alpha \left[\gamma_{ij} \left(S - \rho_H \right) - 2S_{ij} \right], \end{aligned} \tag{1.15} $$

where $S_{ij} = \gamma^\alpha_\mu \gamma^\beta_\nu T_{\alpha\beta}$ is the spatial stress tensor as measured by an Eulerian observer, and S its trace. These evolution equations (Equation 1.9 and Section 1.2.1) along with

the Hamiltonian and momentum constraints (Equations 1.13 and 1.14) are known as the Arnowitt-Deser-Misner (ADM) equations.

1.2.2 The BSSNOK formulation

While they serve as a mathematically complete description of GR, the ADM equations derived in the previous section are not numerically well-posed (see [14] for details). This is not a problem fundamental to the $3+1$ formalism, but rather it can be avoided by restating the ADM equations in a different form. This can be accomplished by transforming the ADM equations to different variables and by adding or subtracting multiples of the constraints (which must vanish for physical spacetimes) to the evolution equations.

One such restatement that is popular in NR is the Baumgarte-Shapiro-Shibata-Nakamura-Oohara-Kojima (BSSNOK) formulation [15, 14], for which the spatial metric is split into a conformal metric $\tilde{\gamma}_{ij}$ and a conformal factor ϕ such that

$$\gamma_{ij} = e^{4\phi}\,\tilde{\gamma}_{ij}. \tag{1.16}$$

The conformal metric is defined to have unit determinant $\tilde{\gamma} = 1$, meaning that the determinant of the spatial metric is given by $\gamma = e^{12\phi}$. Additionally, the extrinsic curvature K_{ij} is separated into its trace K and a conformal rescaling of its trace-free part:

$$\tilde{A}_{ij} = e^{-4\phi}A_{ij} = e^{-4\phi}\left(K_{ij} - \frac{1}{3}K\gamma_{ij}\right). \tag{1.17}$$

Finally, the BSSNOK formulation also defines the conformal connection functions

$$\tilde{\Gamma}^{i} = -\partial_j\tilde{\gamma}^{ij} = \tilde{\gamma}^{jk}\tilde{\Gamma}^{i}_{jk}. \tag{1.18}$$

The equations of motion for the BSSNOK variables are given by

$$\partial_t \phi = -\frac{1}{6}\alpha K + \beta^k \partial_k \phi + \frac{1}{6}\partial_k \beta^k \tag{1.19}$$

$$\partial_t \tilde{\gamma}_{ij} = -2\alpha \tilde{A}_{ij} + \beta^k \partial_k \tilde{\gamma}_{ij} + \tilde{\gamma}_{ik}\partial_j \beta^k + \tilde{\gamma}_{jk}\partial_i \beta^k - \frac{2}{3}\tilde{\gamma}_{ij}\partial_k \beta^k \tag{1.20}$$

$$\partial_t K = -\gamma^{ij} D_i D_j \alpha + \alpha\left(\tilde{A}_{ij}\tilde{A}^{ij} + \frac{1}{3}K^2\right) + 4\pi\alpha\left(\rho_H + S\right) + \beta^k \partial_k K \tag{1.21}$$

$$\partial_t \tilde{A}_{ij} = e^{-4\phi}\left\{-D_i D_j \alpha + \alpha R_{ij} + 4\pi\alpha\left[\gamma_{ij}\left(S - \rho_H\right) - 2S_{ij}\right]\right\}^{\text{TF}} \tag{1.22}$$

$$+ \alpha\left(K\tilde{A}_{ij} - 2\tilde{A}_{ik}\tilde{A}^k_j\right) + \beta^k \partial_k \tilde{A}_{ij} + \tilde{A}_{ik}\partial_j \beta^k + \tilde{A}_{jk}\partial_i \beta^k - \frac{2}{3}\tilde{A}_{ij}\partial_k \beta^k \tag{1.23}$$

$$\partial_t \tilde{\Gamma}^i = \tilde{\gamma}^{jk}\partial_j \partial_k \beta^i + \frac{1}{3}\tilde{\gamma}^{ij}\partial_j \partial_k \beta^k - 2\tilde{A}^{ik}\partial_k \alpha \tag{1.24}$$

$$+ 2\alpha\left(\tilde{\Gamma}^i_{jk}\tilde{A}^{jk} + 6\tilde{A}^{ij}\partial_j \phi - \frac{2}{3}\tilde{\gamma}^{ik}\partial_k K - 8\pi e^{4\phi} S^i\right) \tag{1.25}$$

$$+ \beta^k \partial_k \tilde{\Gamma}^i - \tilde{\Gamma}^k \partial_k \beta^i + \frac{2}{3}\tilde{\Gamma}^i \partial_k \beta^k. \tag{1.26}$$

Alternatively, for spacetimes involving BHs it can be beneficial to formulate the BSSNOK equation in terms of $\chi = e^{-4\phi}$ instead of using ϕ directly [16].

1.2.3 General relativistic hydrodynamics

When matter is present in a spacetime, it is coupled to the field equations through the stress-energy tensor $T_{\mu\nu}$, which takes the form

$$T_{\mu\nu} = \left(\rho + p\right) u_\mu u_\nu + p g_{\mu\nu} \tag{1.27}$$

for a perfect fluid. Here ρ is the energy density of the fluid, p is the pressure, and u^μ is the four-velocity. As a matter of convenience, the energy density is typically split into contributions from the rest mass density ρ_0 and the specific internal energy ϵ:

$$\rho = \rho_0\left(1 + \epsilon\right). \tag{1.28}$$

Additionally, instead of using the four-velocity of the fluid directly one can adopt the Valencia formulation [17] and define a three-velocity as

$$v^i = \frac{1}{\alpha}\left(u^i/u^t + \beta^i\right), \tag{1.29}$$

which is the velocity of fluid elements as seen by an Eulerian observer. A perfect fluid is completely described by $(\rho_0,\, \epsilon,\, p,\, v^i)$, which are collectively called the *primitive variables*. While not a primitive variable strictly speaking, it is also useful to define the Lorentz factor

$$W = -n_\mu u^\mu = \alpha u^t = \frac{1}{\sqrt{1-\gamma_{ij}v^i v^j}}. \tag{1.30}$$

In addition to the field equations, the fluid is subject to the continuity equation

$$\nabla_\mu\left(\rho_0 u^\mu\right) = 0 \tag{1.31}$$

and the conservation of energy-momentum

$$\nabla_\mu T^{\mu\nu} = 0. \tag{1.32}$$

For the purposes of numerical evolution, it is useful to write these equations in a conservative form by defining conserved variables $(D,\, S_i,\, \tau)$ as

$$D = \sqrt{\gamma}\rho_0 W \tag{1.33}$$

$$S_i = \sqrt{\gamma}\alpha T^0_i \tag{1.34}$$

$$\tau = \sqrt{\gamma}\alpha^2 T^{00} - D. \tag{1.35}$$

In terms of these variables, Equations 1.31 and 1.32 can be written as

$$\partial_t D = -\partial_j \left(\sqrt{\gamma} D \left(\alpha v^j - \beta^j \right) \right) \tag{1.36}$$

$$\partial_t S_i = -\partial_j \left(\sqrt{\gamma} \alpha T_i^j \right) + \frac{1}{2} \alpha \sqrt{\gamma} T^{kl} \partial_i g_{kl} \tag{1.37}$$

$$\partial_t \tau = -\partial_j \left(\sqrt{\gamma} \left(\alpha^2 T^{0i} - D \left(\alpha v^i - \beta^i \right) \right) \right) + \alpha \sqrt{\gamma} \left(T^{0k} \partial_k \alpha - \alpha \Gamma^0{}_{kl} T^{kl} \right). \tag{1.38}$$

Finally, in order to close this system it must be supplemented by an equation of state $F(\rho_0, p, \epsilon) = 0$ that describes the fluid.

1.3 MAYA infrastructure

All NR simulations in this thesis were completed using the MAYA infrastructure [18, 19, 20, 21, 22, 23], which is the local version of the EINSTEINTOOLKIT code [24] used a Georgia Tech. At its core MAYA is based on the CACTUS[18] framework, which provides a modular structure upon which NR code can be built. The computational grid takes the form of a hierarchy of nested *refinement levels*, where each level is a uniform three-dimensional Cartesian grid. Throughout evolution, MAYA relies on the CARPET [25, 26] adaptive mesh refinement driver to ensure that all regions of the computational domain are properly resolved.

For spacetime evolution, MAYA uses KRANC[19] to generate highly efficient C code to evolve the BSSNOK equations described in Section 1.2.2 along with the moving punctures gauge condition [16, 27]

$$\partial_t \alpha = \beta^i \partial_i \alpha - 2\alpha K \tag{1.39}$$

$$\partial_t \beta^i = \beta^j \partial_j \beta^i + \frac{3}{4} B^i \tag{1.40}$$

$$\partial_t B^i = \beta^j \partial_j B^i + \partial_t \tilde{\Gamma}^i - \beta^j \partial_j \tilde{\Gamma}^i - 2B^i, \tag{1.41}$$

which is one of the most popular gauge choices used in NR. Equation 1.39 is called the

$1 + \log$ slicing condition, while Equations 1.40 and 1.41 are collectively called the Gamma-driver shift condition. $1 + \log$ slicing instrumental to the stability of NR simulations in the presence of BHs because it ensures that the divergence of the normal vectors n^μ vanishes. As such, it avoids coordinate observers converging to a point leading to the development of coordinate singularities. The Gamma-driver shift condition acts to control changes in the shape of volume elements by minimizing changes in the conformal metric $\tilde{\gamma}_{ij}$.

For hydrodynamical evolution, I use the publicly available ILLINOISGRMHD code [28]. While ILLINOISGRMHD is technically a full general relativistic magnetohydrodynamics (GRMHD) code, no simulations presented in this thesis involve magnetic fields, so the evolution reduces to general relativistic hydrodynamics (GRHD) as described in subsection 1.2.3.

MAYA includes the built in capability to generate initial data for quasi-circular BBH systems. This starts with a script that solves the post-Newtonian equations of motion for the binary [29, 30] given the mass ratio $q = m_1/m_2$ and the spins of the BHs in order to determine the appropriate spins and momenta at the desired initial binary separation. These masses and spins are then provided as input to the TWOPUNCTURES code [31], which solves the Hamiltonian constraint using a Bowen-York extrinsic curvature solution [32]. For TDE initial data, MAYA uses the BOOSTEDSTAR initial data framework. BOOSTEDSTAR was developed as part of the work presented in this thesis and is described in detail in Chapter 4.

During the course of evolution, MAYA uses the AHFINDERDIRECT thorn [33] to locate and analyze apparent horizons (AHs). Additionally, it extracts GW signals from the simulations by means of the Newman-Penrose scalar Ψ_4 [34], which is calculated using the WEYLSCAL4 thorn of the EINSTEINTOOLKIT.

Part I

Binary Black Holes

Overview

The detection of GWs has given birth to a new field of astronomy: GW astronomy. At the time of this writing, the GWTC [3, 4] contains a total of 50 GW detections of compact object mergers, including 46 confident BBH mergers. These GW detections provide the opportunity to strengthen our understanding of compact objects along with their populations [35] and formation channels [36, 37]. Additionally, they allow us to test the concepts of GR [38, 39, 40] in the strong-field regime. So far, all detections are consistent with the predictions of GR [41, 42].

To date, all GW observations display a relatively simple *chirp* morphology [3] consisting of a monotonic increase of both frequency and amplitude as can be seen in the top left panel of Figure 3.1. The slow initial increase of both quantities reflects the low frequency and tightening of the orbit as the two BHs approach each other [43]. This early phase of the BBH system is known as the *inspiral* and can be well-approximated using post-Newtonian methods [29]. Just before merger, the two BHs reach speeds comparable to that of light, leading to a rapid rise of both frequency and amplitude [43, 44]. Once the they merge, the initially highly distorted remnant BH settles into a Kerr solution by radiating exponentially decaying *ringdown* emission [45, 46, 5, 47].

Despite the numerous recent successes of GW astronomy, detailed observations of the ringdown emission from a merger remnant still lie beyond the sensitivity of LIGO and Virgo. It is during this period just after merger that the strong-field regime of dynamical gravity is on full display. As the sensitivity of both LIGO and Virgo improves and the next generation of detectors (such as LISA and the Einstein Telescope (ET)) become operational, GWs will finally provide us with an unprecedented view of this post-merger regime. This will allow us test fundamental aspects of GR such as the no-hair theorem [39, 47] and quantum properties of BHs [48] in further detail.

To prepare for these observations, studies that contribute to a deep understanding of the dynamical properties of BHs in BBH systems and how GW signals encode these properties

are of fundamental importance. Furthermore, it is important to investigate how GWs reflect not only the common properties of BBHs such as BH masses and spins, orbital eccentricity, and orientation, but also any other fundamental aspects of a dynamical BH that can be inferred from the morphology of the signal.

To this end, in this part I describe two studies that investigate the properties of dynamical BHs in BBH systems. In Chapter 2, I describe the evolution and ultimate fate of the two BHs that comprise the binary system. While these BHs are hidden behind the horizon of the remnant post-merger, these results provide insight into the dynamics of the remnant BH which in turn inform the GW emission. Building on this idea, in Chapter 3 I describe the results of a second study investigating the curvature of the remnant BH horizon and how it correlates to the spatial distribution of the resulting GW emission.

CHAPTER 2

PUNCTURE AND TRAPPED SURFACE DYNAMICS

An essential element in NR simulations involving BHs is tracking the location and properties of the holes. A natural structure to accomplish this would be the event horizon of the BH. The problem with these horizons is that they are teleological in nature; that is, we require knowledge of the entire space-time in order to identify their location and dynamics. An alternative is to track AHs [49] since to find them one only needs the intrinsic metric and extrinsic curvature of the spacetime hypersurface at a given time. An AH is the outer-most marginally outer trapped surfaces (MOTSs), and a MOTS is a closed spacelike 2-surface for which the divergence of its outgoing null normals vanishes. AHs can be used to determine the mass and angular momentum of the BHs [50]. Once the common AH forms during the merger, one can also estimate mass and spin multipole moments [51, 52] to quantify the rate at which the final BH approaches equilibrium and potentially identify when the ringdown phase begins [53]. In addition, studies [54, 55, 56, 53, 57] have shown that fields at the AH are correlated with fields in the wave-zone and thus the GW signal itself.

The fate of the common AH resulting from a BH merger has been studied extensively and is fairly well understood [58, 59, 52, 53]. Generally, after a common MOTS forms it bifurcates into two surfaces. The outermost of these two surfaces expands and forms the AH for the final BH, while the innermost surface contracts. Furthermore, the two MOTSs that were initially the AHs of the two original BHs continue to exist well after the formation of the common horizon. While these three interior MOTSs have been studied in some detail [59, 60, 61, 53, 62], their ultimate fate remains uncertain and is the main focus of this chapter.

Since the interior MOTS are hidden behind the common AH, it is not possible to know about their dynamics from the GWs emitted. Nonetheless, investigating the final state of the

punctures and their MOTSs provides insights on the global structure of a strongly nonlinear and dynamical spacetime geometry, a topic of great interest to numerical and mathematical relativists.

In this chapter I present a study published in Classical and Quantum Gravity Letters investigating the dynamics of MOTSs in the head-on collision of BHs for various separations and mass ratios, with the holes modeled as punctures [63]. We find that the MOTSs of the merging punctures will in general intersect. For the situations in which they do not intersect, we show that it is due to the singularity avoidance properties of the moving puncture gauge condition [16, 27] used in the study. Our simulations are not long enough to show the ultimate fate of the MOTSs and their punctures. At the same time, the results provide evidence that the punctures, although close enough to each other to act effectively as a single puncture, do not merge and the MOTSs do not fully overlap. Section 2.1 provides a review of the MOTS involved in the evolutions. In Section 2.2, I outline the computational methods used for the simulations. I present the results of this study in Section 2.3, and provide the conclusions in Section 2.4.

2.1 Marginally trapped surfaces in a black hole binary

Consider a foliation of spacelike hypersurfaces Σ_t as described in Section 1.2. The initial slice Σ_0 consists of two BHs at a coordinate separation d_0. Depending on the value of d, Σ_t could have up to four MOTSs [59, 60, 61, 53, 62]. For large enough d, Σ_t will have two non-connected MOTSs $\mathcal{S}_1$ and $\mathcal{S}_2$, which correspond to the AH of each individual BH. At some separation d_c, a slice Σ_t will also have a MOTS $\mathcal{S}_c$ surrounding $\mathcal{S}_1$ and $\mathcal{S}_2$. Since $\mathcal{S}_c$ is the outermost MOTS for Σ_t, the surface is an AH and referred to as the *common* AH. After some time, $\mathcal{S}_c$ will become the event horizon of the final BH. For separations $d < d_c$, a fourth MOTS $\mathcal{S}_i$ peels off from the interior of $\mathcal{S}_c$, shrinking and hugging $\mathcal{S}_1$ and $\mathcal{S}_2$. These four MOTSs, $\mathcal{S}_1$, $\mathcal{S}_2$, $\mathcal{S}_c$, and $\mathcal{S}_i$, are slices of four different dynamical horizons [58, 51, 64, 52]. However, for $\mathcal{S}_i$ this only applies for a short time before the surface becomes

timelike [59]. For sufficiently small initial separations, $\mathcal{S}_1$ and $\mathcal{S}_2$ are at all times *nearly* null surfaces [59] and thus they are isolated horizons to good approximation [65].

The primary difficulty in studying the eventual fate of $\mathcal{S}_1$ and $\mathcal{S}_2$ is that for the coordinate conditions typically used with punctures in NR simulations, the surfaces shrink after the formation of $\mathcal{S}_c$, requiring progressively finer spatial resolution to properly resolve them. As a result, it is challenging to make any definitive statements as to whether or not the MOTSs exist based solely on the fact that they could not be located numerically.

Many investigations into $\mathcal{S}_1$ and $\mathcal{S}_2$ have focused on locating them on a series of initial data slices with varying separations, thereby avoiding the computational cost of performing high resolution evolutions in time. Jaramillo, Ansorg, and Vasset [60] studied Bowen-York [32] initial data and found that at decreasing separations, $\mathcal{S}_1$ and $\mathcal{S}_2$ shrink progressively smaller and show no indications of intersecting. Instead, $\mathcal{S}_i$ becomes highly distorted while $\mathcal{S}_1$ and $\mathcal{S}_2$ 'accumulate' against it. Pook-Kolb et al. [62] studied an analogous series of time symmetric Brill-Lindquist initial data [66, 67] and found that $\mathcal{S}_1$ and $\mathcal{S}_2$ intersect and merge with $\mathcal{S}_i$ at the exact moment of intersection. Schnetter, Krishnan, and Beyer [59] carried out simulations of head-on collision of Brill-Lindquist initial data. While they did lose the ability to track $\mathcal{S}_i$ rather early due to its high distortion, they made no statements about its ultimate fate or what happens to $\mathcal{S}_1$ and $\mathcal{S}_2$. They did however speculate that if these three surfaces do in fact merge, it is more likely that $\mathcal{S}_1$ and $\mathcal{S}_2$ merge first to form a new surface that then merges with $\mathcal{S}_i$. This question was recently resolved by Pook-Kolb et al. [68, 69], who have shown numerically that $\mathcal{S}_i$ merges with $\mathcal{S}_1$ and $\mathcal{S}_2$ precisely when they first touch.

2.2 Numerical methods

All simulations in this study use Brill-Lindquist initial data [66, 67] representing two initially at rest, non-spinning BHs with total mass $M = m_1 + m_2$, mass ratio $q = m_1/m_2$, and separated by a coordinate distance d_0. During the evolution, we use AHFINDERDIRECT [33] to locate the MOTSs.

As $\mathcal{S}_1$ and $\mathcal{S}_2$ approach each other, they will shrink in coordinate radius. The spatial resolution required to properly resolve and track them will thus increase accordingly. To ensure sufficient resolution, we activate additional refinement levels (one level each time the MOTS radius reduces by half) thereby maintaining roughly the same number of points across each MOTS. When $\mathcal{S}_c$ is first located, $\mathcal{S}_1$ and $\mathcal{S}_2$ are each completely covered by three refinement levels, with each level consisting of 60^3 points. The resolutions for each refinement are: $M/100$, $M/200$ and $M/400$. By the end of the simulations we use up to five additional refinement levels, with a resolution of $M/12800$ at the finest level.

The MAYA code solves the χ formulation of the BSSNOK equations (see Section 1.2.2 for details) and enforces a floor value $\chi \geq \chi_\epsilon$ to handle regions where the conformal factor diverges, e.g. at the punctures or singularities where $\chi = 0$. We carried out a series of $q = 1$ and fixed d_0 simulations in the range $10^{-3} > \chi_\epsilon > 10^{-6}$ and found that the time after which we can no longer locate $\mathcal{S}_1$ and $\mathcal{S}_2$ varies as $t_f \sim \chi_\epsilon^{-0.05}$. With a floor value of $\chi_\epsilon = 10^{-6}$, we obtain stable evolutions lasting $t_f \approx 20\,M$.

2.3 Ultimate fate of $\mathcal{S}_1$ and $\mathcal{S}_2$

Figure 2.1 shows the parameter space q vs. d_0 of the simulations, where q is the mass ratio and d_0 the initial coordinate separation. There are two distinct regions: one in the lower right corner (shaded gray) in which $\mathcal{S}_1$ and $\mathcal{S}_2$ do not intersect and the rest of parameter space in which they do. The boundary separating these two regions is given by

$$q \approx 1.135 + \sqrt{4.065\,(d_0/M) - 6.674}. \tag{2.1}$$

Since all the simulations are head-on collisions with the punctures separated along the z-axis, we track the coordinate separation between $\mathcal{S}_1$ and $\mathcal{S}_2$ with $\Delta z = z_1 - z_2$ where z_1 and z_2 are respectively the z-components at the surfaces of $\mathcal{S}_1$ and $\mathcal{S}_2$ that face each other (as seen in Figure 2.2). The coordinate origin is set at the center of mass of the initial

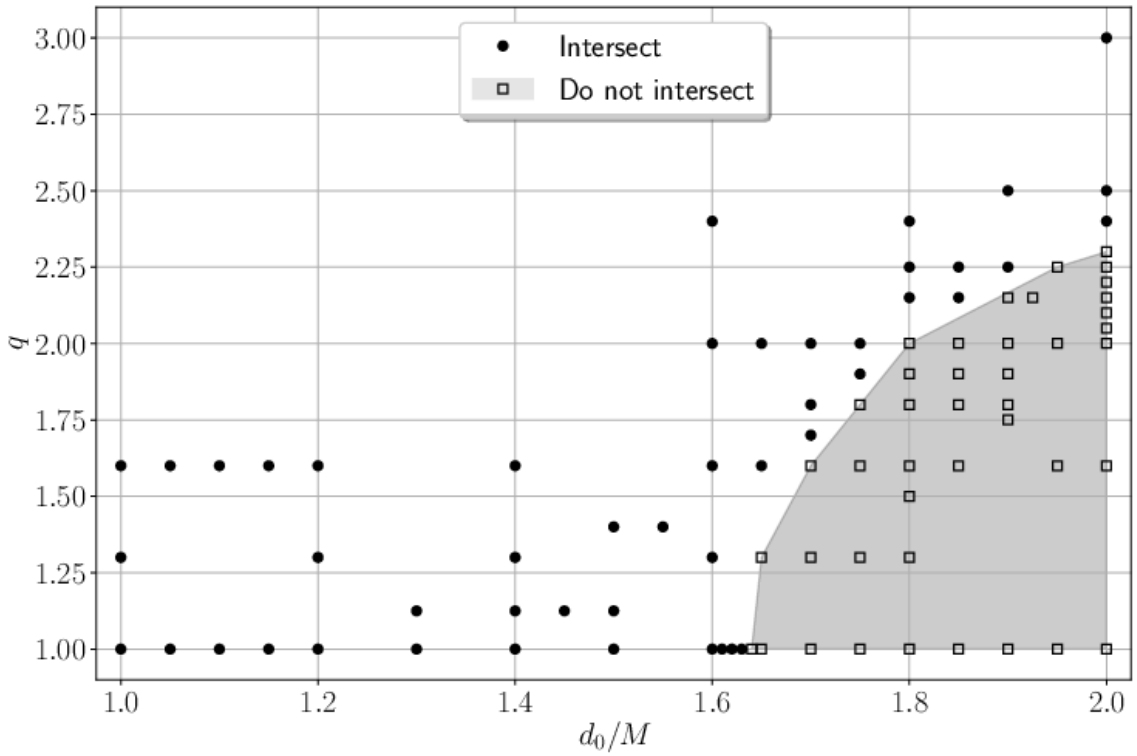

Figure 2.1: Parameter space of simulations. Simulations are characterized by mass ratio q and initial coordinate separation d_0. Cases for which $\mathcal{S}_1$ and $\mathcal{S}_2$ intersect are denoted by filled circles and non-intersecting by open boxes. In gray is the region of non-intersecting simulations.

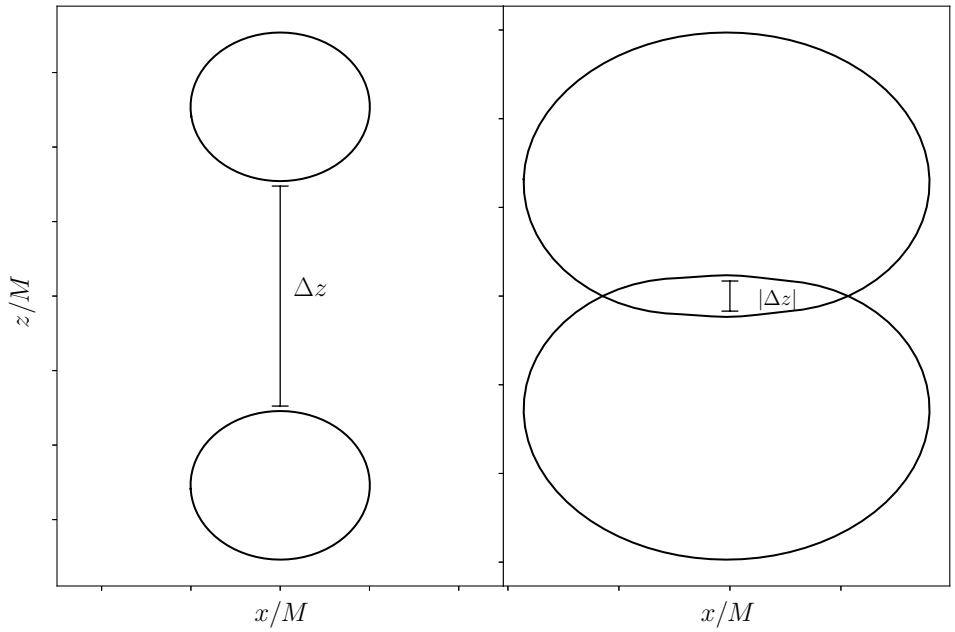

Figure 2.2: Definition of the coordinate separation Δz between $\mathcal{S}_1$ and $\mathcal{S}_2$.

configuration. Initially $z_1 > 0$ and $z_2 < 0$, thus when the two surfaces intersect we have $z_1 < z_2$ and Δz becomes negative. Figure 2.3 shows $|\Delta z|$ as a function of coordinate time t for a few equal-mass ($q = 1$) configurations. The left panel shows three cases in which $\mathcal{S}_1$ and $\mathcal{S}_2$ intersect. The time axis has been shifted so the cases align when the surfaces intersect at time t_*, which depends on d_0. The right panel shows three cases in which $\mathcal{S}_1$ and $\mathcal{S}_2$ *do not* intersect. From these two panels it is clear that, at late times, both the separation for the non-intersecting cases and the overlap for the intersecting cases decrease as $|\Delta z| \sim e^{-t/\lambda}$. The same exponential decay extends to the unequal-mass ($q > 1$) cases. For all configurations, we find that $\lambda \approx 2M$. The exponential decay in the surface separation is also present in the coordinate separation d of the two punctures. Beginning shortly after the formation of $\mathcal{S}_c$, we find again that $d \propto e^{-t/\lambda}$ with $\lambda \approx 2M$.

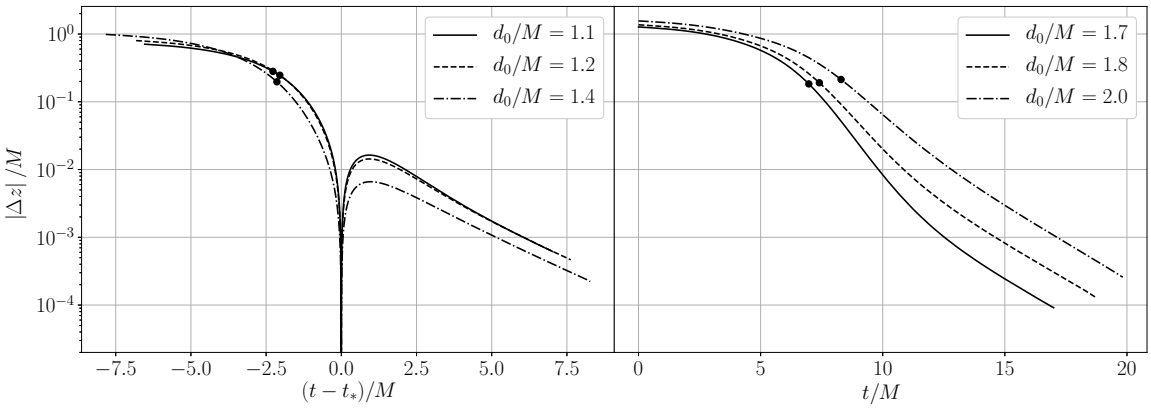

Figure 2.3: Coordinate separation $|\Delta z|$ between $\mathcal{S}_1$ and $\mathcal{S}_2$ for a few $q = 1$ examples as a function of coordinate time t. The left panel depicts three intersecting cases aligned at the time of intersection. The right panel shows three non-intersecting cases. Solid dots denote the time at which the common AH appears.

2.3.1 Collapse of the lapse

To understand the exponential decay in both the separation between $\mathcal{S}_1$ and $\mathcal{S}_2$ and the distance between the two punctures, recall that in the moving puncture gauge the lapse function α satisfies the $1 + \log$ type slicing condition

$$\left(\partial_t - \beta^i \partial_i\right) \alpha = -n\alpha K, \tag{2.2}$$

where β^i is the shift vector, K the trace of the extrinsic curvature, and n a constant. As is customary, we choose $n = 2$. With this choice, stationary slices of a single Schwarzchild puncture are given by a family of *trumpet slices* [70], for which the surface of zero isotropic radius (the trumpet surface) has a non-zero areal radius. Furthermore, the lapse on the trumpet surface vanishes thereby avoiding the singularity at the puncture. With the moving puncture gauge, the positions of the punctures $x^i_{1,2}$ are found by integrating [16].

$$\partial_t \, x^i_{1,2} = -\beta^i_{1,2}. \tag{2.3}$$

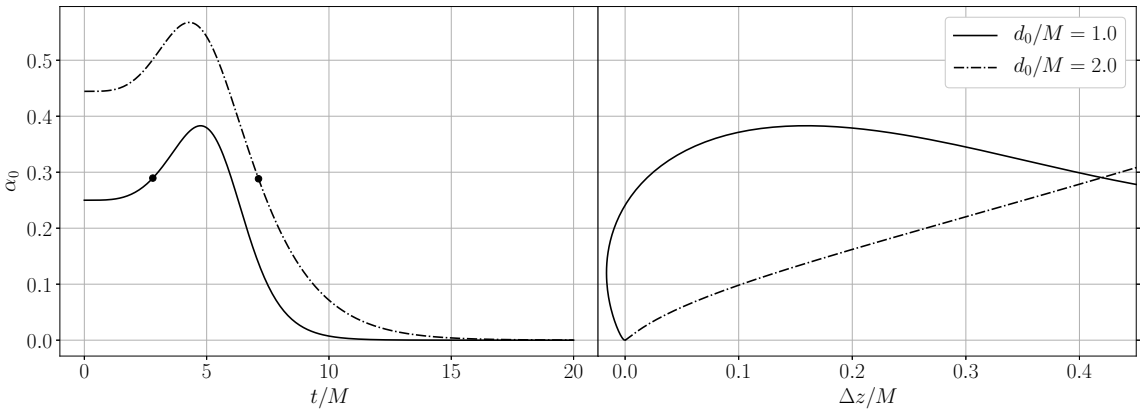

Figure 2.4: Lapse at the coordinate origin α_0 for $q = 1$ and $d_0/M = 1,\ 2$. The left panel shows how α_0 changes as a function of coordinate time t. The right panel shows how α_0 changes with Δz. For $d_0/M = 2$, by the time $\Delta z = 0$, the lapse has already collapsed. In contrast, for $d_0/M = 1$, $\Delta z = 0$ is reached when $\alpha_0 \approx 0.25$. After this point, as α_0 collapses, Δz reaches a minimum and at late times $\Delta z \to 0$.

For Schwarzchild trumpet slices, $\beta^r = r/\lambda$ near the puncture [70, 71]. As a result, the radial coordinate distance to each puncture is given by $r_{1,2} \propto e^{-t/\lambda}$, with the decay rate λ computed from

$$\lambda^2 = \frac{1}{r}\beta^r \partial_r \beta^r. \tag{2.4}$$

Substituting the solution for $1 + \log$ trumpet slices found by Hannam et al. [72] into this expression yields

$$(\lambda/M)^2 \approx \frac{(R_0/M)^3}{(2 - R_0/M)}\,, \tag{2.5}$$

where $R_0 \approx 1.3124\,M$. This gives a decay rate of $\lambda \approx 1.82\ M$, which is consistent with the numerical value from our simulations. The minor disagreement is easily explained by the fact that our numerical simulations do not reach full stationarity before completion and the shift vector is evaluated slightly away from the puncture.

To demonstrate how the lapse function is connected to the observed behavior of $\mathcal{S}_1$ and $\mathcal{S}_2$, in Figure 2.4 we show the lapse function at the origin α_0 as a function of coordinate time t (left panel) and as function of Δz (right panel). Two cases are plotted: one in which the surfaces do not intersect ($d_0/M = 2$) and another in which they do ($d_0/M = 1$). From

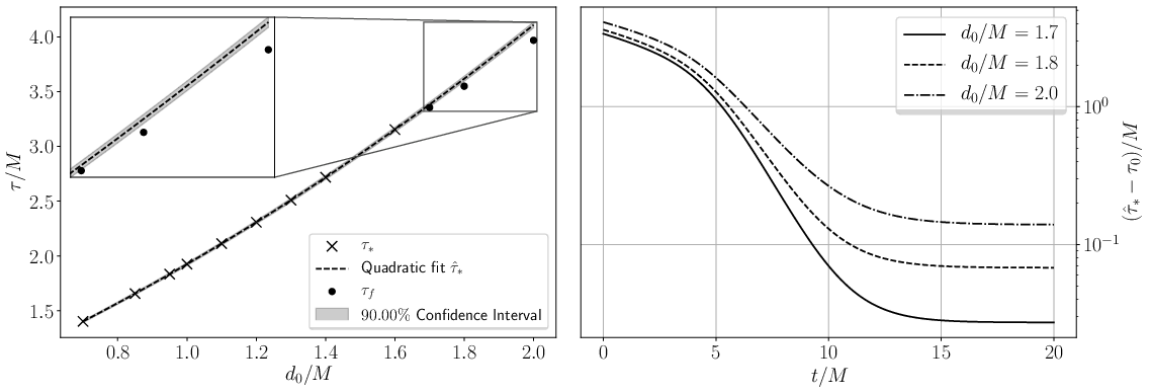

Figure 2.5: Left panel shows proper time τ_* (crosses) at the origin when $\mathcal{S}_1$ and $\mathcal{S}_2$ intersect at time t_* for $q = 1$ as a function of d_0. Included is also a quadratic fit $\hat{\tau}_*$ and in gray the 90% confidence interval. With solid dots are the proper time τ_f elapsed at the origin by the end of the simulations for three non-intersecting cases. The right panel shows $\hat{\tau}_* - \tau_0$ as a function of t for those three non-intersecting cases.

the left panel it is clear that, that in both cases, the lapse eventually collapses and thus halts the evolution. The difference in how the collapse proceeds in each case and how this affects the final outcome is more evident in the right panel. We see in this panel that at $\Delta z \approx 0.42$ both cases have the same value of α_0, shown as solid dots in the left panel. For the non-intersecting case ($d_0/M = 2$) , α_0 is already starting to collapse at this separation. On the other hand, for the intersecting case ($d_0/M = 1$), α_0 is still growing; thus, the evolution lives longer and the surfaces are able to intersect before the end of the simulation. It is also interesting to note that the degree of intersection or surface overlap reaches a maximum and then decreases as the lapse enters collapse. Later in this chapter, I will show that this is only a coordinate effect.

2.3.2 Proper time to intersection

To further support the importance of lapse collapse to the behavior of $\mathcal{S}_1$ and $\mathcal{S}_2$, we calculate the the proper time elapsed at the origin since the beginning of the simulation

$$\tau_0(t) = \int_0^t dt' \, \alpha_0(t'). \tag{2.6}$$

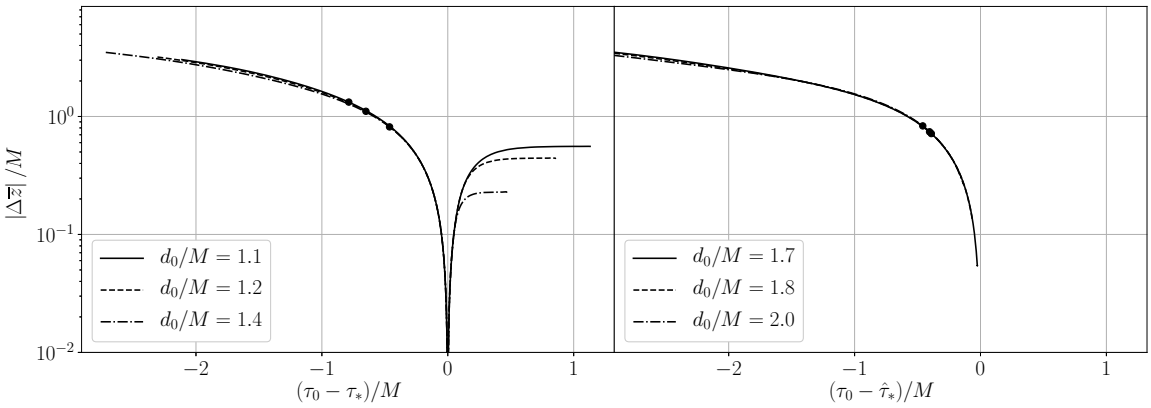

Figure 2.6: Proper separation $|\Delta\bar{z}|$ between $\mathcal{S}_1$ and $\mathcal{S}_2$ for a few $q = 1$ examples as a function of proper time τ_0 measured at the origin of the coordinate system. The left panel depicts three intersecting cases aligned at the time of intersection. The right panel shows three non-intersecting cases. Solid dots denote the time at which the common AH appears.

In the left panel of Figure 2.5 we denote with crosses $\tau_* \equiv \tau_0(t_*)$, where t_* is the coordinate time when $\mathcal{S}_1$ and $\mathcal{S}_2$ intersect. Also plotted is a quadratic fit

$$\hat{\tau}_*/M = 0.337\,(d_0/M)^2 + 1.170\,(d_0/M) + 0.417 \tag{2.7}$$

along with the 90% confidence interval in gray. The inset shows an extrapolation of $\hat{\tau}_*/M$ beyond the intersecting cases, along with three solid dots denoting $\tau_f = \tau_0(t_f)$ for non-intersecting cases, where t_f is the time at the end of the simulation. Notice that in all non-intersecting cases $\tau_f < \hat{\tau}_*$, meaning that none of these simulations reached the time at which we would expect $\mathcal{S}_1$ and $\mathcal{S}_2$ to intersect. The right panel in Figure 2.5 shows the remaining proper time before the two surfaces are expected to intersect $\hat{\tau}_* - \tau_0$ as a function of coordinate time t for the three non-intersecting cases, which tends towards a positive constant as the lapse collapses, signaling that the progression of proper time has halted.

2.3.3 Invariant length measures

As mentioned previously in this chapter, tracking the separation or overlap of $\mathcal{S}_1$ and $\mathcal{S}_2$ using coordinate distances comes with the complication that the outcome is influenced

by the choice of gauge. To circumvent this, in Figure 2.6 we show the proper distance separation $|\Delta\bar{z}|$ as a function of proper time τ_0 corresponding to the cases in Figure 2.3. The left panel depicts the intersecting cases, with time shifted by the time at intersection τ_*. The right panel shows three non-intersecting cases with the time also shifted but in this case by $\hat{\tau}_*$ from the fit shown in Figure 2.5. It is clear from both panels that for $\tau_0 - \tau_* < 0$ and $\tau_0 - \hat{\tau}_* < 0$, the proper separation is independent of d_0. Also, if we were to combine the data from both panels, it would show that for these times all cases lie on top of each other; thus, there is no difference between intersecting and non-intersecting cases. Therefore, here again the data suggest that if the evolutions for the non-intersecting cases were able to proceed, then the surfaces would eventually intersect. The differences in $|\Delta\bar{z}|$ with d_0 only arise when $\tau_0 > \tau_*$, namely after the surfaces overlap. The left panel shows that at late times $\mathcal{S}_1$ and $\mathcal{S}_2$ reach a constant proper overlap, with smaller values of d_0 corresponding to larger final overlaps. Furthermore, we find that the final overlap volume is never large enough to contain the punctures; they remain in the non-overlapping regions.

To gain further insight about the final state of the MOTSs and punctures, in Figure 2.7 we plot the evolution of the areal radius $R = \sqrt{A/4\pi}$ (where A the area of the MOTS) for a few equal-mass intersecting cases with. It is clear that toward the end of the simulation, the surfaces $\mathcal{S}_1$ and $\mathcal{S}_2$ reach a constant areal radius and thus become isolated horizons [49]. This, together with the finding that $\mathcal{S}_1$ and $\mathcal{S}_2$ have a constant proper overlap, strongly suggests that the configuration is effectively frozen and the punctures will not merge.

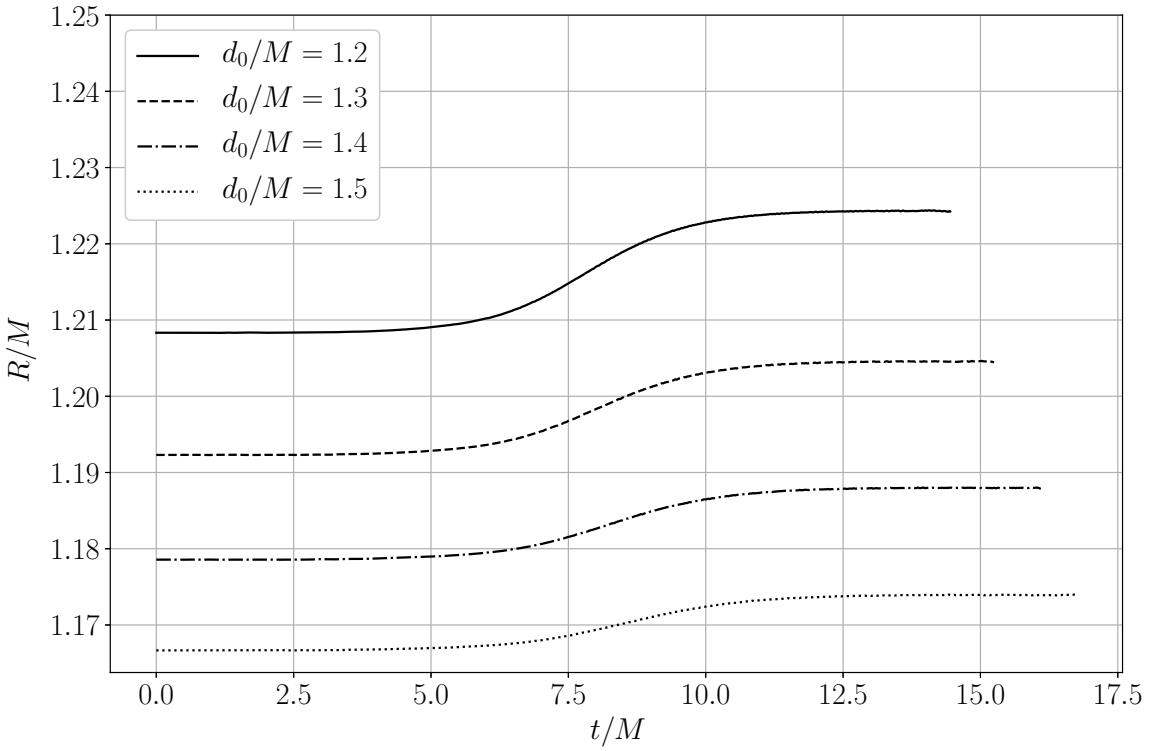

Figure 2.7: Evolution of the areal radius of $\mathcal{S}_1$ for intersecting cases with $q = 1$. The areal radius of $\mathcal{S}_2$ is the same as that for $\mathcal{S}_1$ since the holes have equal masses.

2.4 Conclusions

In this chapter I have presented results from a two-parameter study (mass ratio q and initial separation d_0) of head-on collisions of BHs. The focus was on the ultimate fate of the MOTSs $\mathcal{S}_1$ and $\mathcal{S}_2$ that initially were the AHs of the colliding BHs. Depending on the values of q and d_0, once inside the common AH the surfaces $\mathcal{S}_1$ and $\mathcal{S}_2$ intersect if the lapse function α_0 takes longer to collapse before the end of the simulation. The collapse of the lapse is fundamental to the singularity avoidance properties of the moving puncture gauge condition [16, 27] used in the simulations. We show that for all configurations in this study, at late times the coordinate separation of the BH punctures and of the MOTS surfaces $\mathcal{S}_1$ and $\mathcal{S}_2$ decays as $e^{-t/\lambda}$ with $\lambda \approx 2M$. When the separation of $\mathcal{S}_1$ and $\mathcal{S}_2$ is measured using proper distances, we find that all cases exhibit the same behavior as a function of proper time at early times. The data suggest that if it were not for the collapse of the lapse, all configurations would intersect. Furthermore, the intersection or overlap of the two surfaces freezes at late times. Similarly, the areal radii of $\mathcal{S}_1$ and $\mathcal{S}_2$ become constant at late times, implying that the surfaces become isolated horizons. Together these two facts (the freezing of the areal radius and the overlap) strongly suggest that the punctures do not merge. However, since this occurs at very small separations, ($|\Delta z| \sim 10^{-4}M$), for practical purposes, the two punctures act as a single puncture, namely the singularity of the final BH.

CHAPTER 3

POST-MERGER CHIRPS FROM BINARY BLACK HOLES

Even though all current GW observations present with the chirp morphology described earlier in this part, general GW signals can be far more intricate. The complex GW strain emitted in a direction (ι, ϕ) on the sky of a BBH can be written as a superposition of modes $h_{\ell,m}(\iota, \phi; t)$: [73]

$$h(t) = h_+(t) - ih_\times(t) = \sum_{\ell \geq 2} \sum_{m=-\ell}^{m=\ell} Y^{-2}_{\ell,m}(\iota, \phi) h_{\ell,m}(t). \tag{3.1}$$

Here h_+ and $h_\times$ denote the two GW polarizations, $Y_{\ell,m}$ are the spin-2 weighted spherical harmonics and (ι, ϕ) are the polar and azimuthal angles (respectively) of a spherical coordinate system centered on the binary. In this context, ℓ and m are *not* spatial indices. The coordinates are defined such that $\iota = 0$ (face-on) denotes the direction of the orbital angular momentum, while the orbital plane of the binary is located at $\iota = \pi/2$ (edge-on).

When the binary is nearly equal-mass and viewed face-on, the emission is dominated by the $(2, \pm 2)$ quadrupole modes [73] and therefore the frequency of the GW signal is twice the orbital frequency, to good approximation. Highly symmetric binaries such as these produce GWs that present the canonical single chirp morphology described at the beginning of this part. In contrast, asymmetric BBHs (with unequal masses or spinning BHs) also produce strong GW emission in the sub-dominant higher order modes during merger and ringdown [74, 45, 75, 76], allowing for GWs signals with non-trivial morphologies [77, 75, 76] that may shed light on novel features of the post-merger dynamics.

The connection between horizon dynamics and GW emission has been widely studied using a variety of approaches. For example, examining correlations between far-field signals and local fields near the horizon reveals close connections between the horizon

geometry, the GW flux, and strong-field phenomena such as anti-kicks [78, 79, 80, 81]. Alternatively, directly examining the strong-field dynamics that ultimately cause these correlations produces insight into the generation of GWs [82, 83, 84, 85, 86]. However, none of these previous studies describe a direct link from the horizon geometry to the to the GW strain observed by detectors.

In this chapter I present a study published in Communications Physics in which we expand upon the approach of [78, 79, 80, 81] in order to correlate a concrete, observable feature of the GW strain to geometric properties of the remnant BH horizon. Using a series of NR simulations that I performed using the computational infrastructure outlined in Section 1.3, we demonstrate that multiple post-merger frequency peaks (or chirps) can be measured near the orbital plane of unequal-mass binaries [1]. We then show that these chirps correlate to the line-of-sight passage of strongly emitting regions of the remnant BH with both large mean curvature gradient and locally extremal Gaussian curvature. These strongly emitting regions cluster around a cusp-like defect on the dynamical AH surface itself. Conversely, frequency minima in the GW signal correspond to the passage of the smoother region of the AH opposite the cusp, where curvature gradients are smaller.

3.1 Apparent horizon surface and curvatures

Throughout this chapter I use index notation that is a variation on that described in Section 1.1. As in the rest of the thesis, the indices i, j, k, l to refer to the spatial coordinates $x^i = (x, y, z)$ on a time-slice Σ_t, however indices a, b, c, d to refer to the angular coordinates $y^a = (\theta, \phi)$ on the horizon surface $\mathcal{S}$.

Consider a spacelike hypersurface Σ_t with 3-metric γ_{ij} and associated covariant derivative operator D_i, as described in Section 1.2. The spatial metric on an AH surface $\mathcal{S} \in \Sigma_t$ is

[1] In this work we only consider non-spinning BHs, therefore asymmetric binaries and unequal-mass binaries are effectively synonymous within the scope of this chapter.

simply given by the metric induced on $\mathcal{S}$ by γ_{ij}

$$q_{ij} = \gamma_{ij} - n_i n_j, \tag{3.2}$$

where n^i is the outward-pointing unit normal to $\mathcal{S}$.

The mean curvature of the apparent horizon surface is given by the divergence of the surface normals

$$H = D_i n^i. \tag{3.3}$$

The mean curvature is *extrinsic* to the surface $\mathcal{S}$, meaning that it depends on the metric and its derivatives in the neighborhood of the horizon, not just on the surface itself. As a result, the amount of output data required to calculate H during post-processing is prohibitively large. Instead I calculate the mean curvature at run time using the AHFINDERDIRECT thorn, which already constructs interpolations of the metric and its derivatives near $\mathcal{S}$ in the process of locating it. On the other hand, the Gaussian curvature K of $\mathcal{S}$ is intrinsic to the surface and can therefore be calculated using only the metric induced metric and its derivatives on the horizon. I have modified the AHFINDERDIRECT thorn to output q_{ij} on $\mathcal{S}$ in order to calculate K in post-processing.

For a two-dimensional surface the Riemann tensor has only one independent component and is therefore completely determined by the Ricci scalar. The Gaussian curvature of $\mathcal{S}$ is half of the Ricci scalar and is related to components of the Riemann tensor as

$$R_{abcd} = K(q_{ac}q_{db} - q_{ad}q_{cb}). \tag{3.4}$$

While this equation is valid for any component R_{abcd}, here I use the $R_{\theta\phi\theta\phi}$ component.

In this work we only consider curvatures in the orbital plane of the binary, where the complexity of Equation 3.4 is significantly reduced due to the symmetry properties of q_{ab}. With our focus limited to the curve formed by the intersection of the orbital plane and the

horizon surface it is natural to compute derivatives with respect to the arc-length s along this curve, which is related to the azimuthal angle ϕ as

$$\frac{ds}{d\phi} = \sqrt{q_{ij}\frac{dx^i}{d\phi}\frac{dx^j}{d\phi}} = \sqrt{q_{rr}\left(\partial_\phi R\right)^2 + q_{\phi\phi} + 2q_{r\phi}\left(\partial_\phi R\right)}\,, \tag{3.5}$$

where R denotes the coordinate radius of the horizon. The spherical components of q_{ij} are related to the Cartesian components output by AHFINDERDIRECT by

$$\begin{aligned} q_{rr} &= \cos^2(\phi)q_{xx} + \sin^2(\phi)q_{yy} + \sin(2\phi)q_{xy} \\ q_{\phi\phi} &= r^2\left(\sin^2(\phi)q_{xx} + \cos^2(\phi)q_{yy} - \sin(2\phi)q_{xy}\right) \\ q_{r\phi} &= \frac{1}{2}\sin(2\phi)(q_{xx} - q_{yy}) + \cos(2\phi)q_{xy} \end{aligned} \tag{3.6}$$

3.2 Post-merger chirps

Figure 3.1 shows the GW strain and the corresponding spectrograms[2] as measured by observers at various locations (or viewing angles), which have been extracted from NR simulations. The green vertical lines denote the formation of the common AH. Some time after the common horizon forms, each of these signals show a clear drop in frequency followed by a secondary peak or *post-merger chirp*. The top row of Figure 3.1 shows the waveforms for $q = 3$ and various different observer locations indicating that, depending on the location of the observer, the post-merger chirps occur at different times and involve different frequencies and intensities. As expected, when observed face-on (leftmost panel) the signal presents the simple chirp structure that is consistent with current GW observations [3, 6].

It is illustrative to compare the signals observed in the direction of the GW recoil [77, 76] of the final BH (kick-on) to those observed in the opposite direction (kick-off). While the kick-on observer records a secondary chirp with larger amplitude and peak frequency

[2] All spectrograms shown in this chapter were generated by performing a wavelet decomposition of the signals using PYCWT [87].

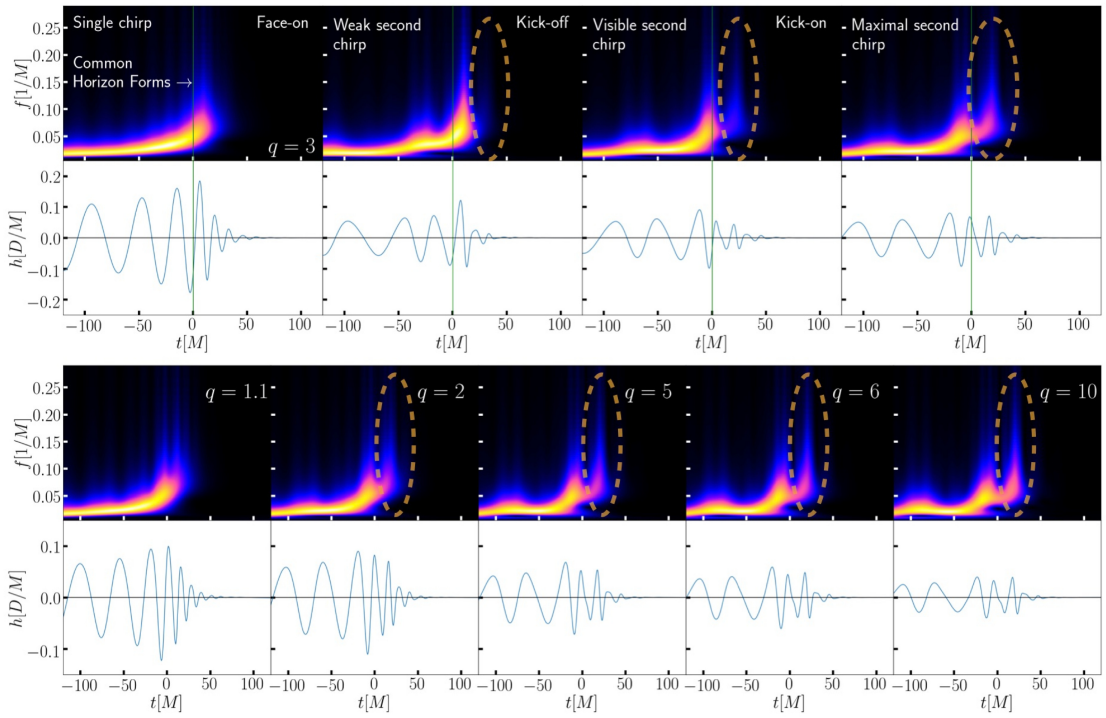

Figure 3.1: The GW strain $h(t)$ extracted from NR simulations (white background) and the corresponding spectrograms (black background). The green vertical lines denote the time at which the remnant AH is first located in the simulations. The top row shows the $q = 3$ case for four different viewing angles (left to right): face-on, kick-off, kick-on, and $55°$ away (in the direction of the orbit) from the kick direction. The last of these is the viewing angle for which the double-chirp feature is most prominent. The bottom row shows five different cases with mass ratios $q = 1.1, 2, 5, 6$, and 10 again in the direction that maximizes the double-chirp.

than the first, the converse is true for the kick-off observer. We find that the intensity of the second chirp is maximized when observed in a direction $\simeq 55^\circ$ away from the kick, as measured along the direction of the original orbit. This signal observed at this viewing angle is shown in the rightmost panel, showing a pronounced double-chirp. Notably, we find that this viewing angle maximizes the intensity of the second chirp irrespective of the mass ratio. We will refer to observers at this viewing angle as maximal-chirp observers. In the bottom row of Figure 3.1, we show the signals for mass ratios of $q = 1.1 - 10$ as measured by maximal-chirp observers, which clearly demonstrate that the double-chirp structure becomes more pronounced as the binary becomes more asymmetric (higher mass ratio). A similar non-trivial post-merger emission, visible in the time-domain, was described by González et al. [77] in terms of the Newman-Penrose scalar Ψ_4. However its frequency content, which is the departing point of our study and the motivation behind the double-chirp name, was not shown.

Analytically, these complex and observer-dependent post-merger waveform morphologies can be explained by the asymmetric interaction of the higher-order quasi-normal modes beyond the in different directions around the binary. These modes are excited during the merger and ringdown of asymmetric binaries and are known to be more prominent for highly inclined binaries [74, 76, 88]. However, the remarkable clarity of the double-chirp morphology suggests a connection to some underlying post-merger feature, analogous to how the increase of the frequency during the inspiral is connected to the increasing frequency of the binary. In the remainder of this chapter, I argue that this underlying feature is the existence of regions of locally extremal curvature that are distributed non-uniformly on the dynamical horizon surface of the remnant BH. Three of these regions cluster around a global curvature maximum (cusp), together forming a trident. The fourth can be found on the opposite (back) side of the horizon. These four regions all coincide with regions of maximal GW emission. Maintaining some of the original orbital angular momentum of the binary, this geometric structure continually rotates while the final BH relaxes, sweeping

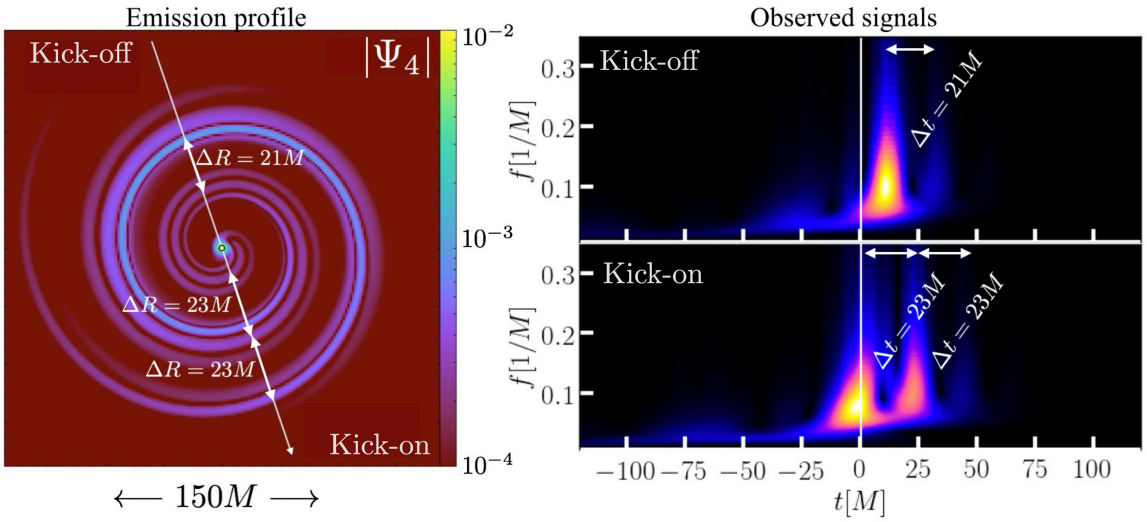

Figure 3.2: Panel **a** shows a snapshot of $|\Psi_4|$ (which encodes the GW emission) in the orbital plane of a $q = 3$ binary $52.3\,M$ after the merger. I have also marked the location of the kick-on and kick-off observers, along with the separation $\Delta R \sim 20\,M$ between the wave fronts traveling towards each observer. Panel **b** shows the corresponding spectrogram as seen by both the kick-on and kick-off observers. Note that the time elapsed $\Delta t \sim 20\,M$ between frequency peaks (chirps) is consistent with the separation of the arriving wave fronts seen in **a**. Two strong wave fronts reach the kick-on observer and produce a prominent double-chirp, however the second front to reach the kick-off observer is much weaker, leading to a weaker second chirp.

across all observers on the orbital plane as it fades away. We also show that after the cusp (back) of the horizon crosses the line-of-sight, frequency maxima (minima) are recorded at a time consistent with the GW travel time determined by the distance to the observer.

3.2.1 Far-field emission profile

In order to develop a qualitative understanding of how the spectrogram of the signal relates to the spatial structure of the GW emission, in Figure 3.2a I show a snapshot of the GW emission in the orbital plane of the $q = 3$ binary after the waves have traveled far from the source ($52.3\,M$ after merger). To visualize the GW emission I use the absolute value of the Newman-Penrose scalar $|\Psi_4|$ [89], which is related to the second time derivative of the GW strain. Based on the distribution of wavefronts in Figure 3.2a, it is clear that the observed frequency content of the GW signal depends on the viewing angle. This is

confirmed in Figure 3.2b, which shows the markedly different spectrograms measured by the kick-on and kick-off observers.

Furthermore, Figure 3.2a shows that there is a pair of wavefronts traveling towards each observer, with the two fronts being separated by $\Delta r \sim 20\,M$. The propagation time across this separation is consistent with the time delay $\Delta t \sim 20\,M$ between chirps seen in Figure 3.2. In addition, the relative intensities of the wave fronts approaching each observer in Figure 3.2a are in qualitative agreement with the intensities of the chirps in Figure 3.2b. The two wave fronts that reach the kick-on observer have similar intensities and therefore produce a prominent double-chirp, whereas the second front to arrive at the kick-off observer is significantly less intense than the first, resulting in a second chirp that is barely visible.

3.2.2 Horizon geometry and the near-source radiation fields

With this connection between post-merger chirps and the far-field GW emission profile in mind, we can now shift focus to the near-horizon region to investigate how the emission relates to the post-merger horizon dynamics. The snapshots shown in Figure 3.3e-h show the structure of Ψ_4 near the horizon at four selected times t_{frame} during its evolution. In the first snapshot (Figure 3.3e) soon after the horizon forms, Ψ_4 shows a distinctly asymmetric pattern. All four arms of the structure described at the beginning of this section are visible, with the most prominent central arm of the trident aligned with the cusp on the horizon. Note that this structure *does not* form abruptly at merger, but instead arises smoothly from the existing structure of Ψ_4 that results from the inspiral of the two BHs. The next three snapshots (Figure 3.3f-h) show how this structure rotates and begins to fade away as the remnant BH relaxes. During this rotation, all four arms of the Ψ_4 structure sweep across the line-of-sight of every observer multiple times.

In Figure 3.3a-d we show both Ψ_4 and the GW strain h measured by the kick-on and kick-off observers along with the corresponding spectrograms. Note that the time axis along

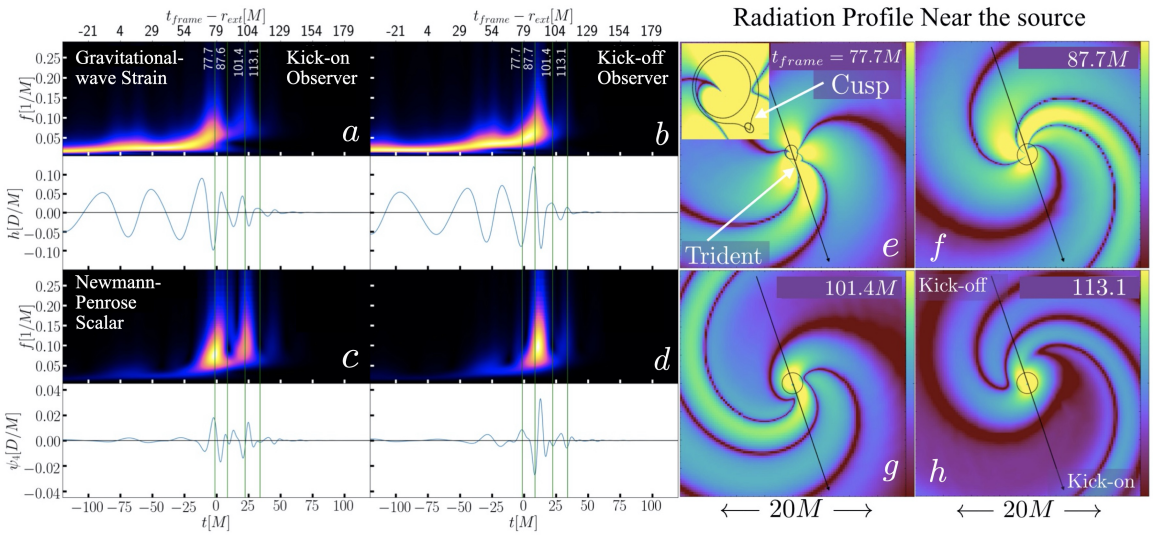

Figure 3.3: Panels **a** and **b** show the GW strain h (white background) and the corresponding spectrograms (black background) as recorded by the kick-on and kick-off observers, respectively, extracted at a distance of $r_{ext} = 75\,M$ from the source. Panels **c** and **d** show the same for Ψ_4 instead of h. The upper time axis shows the retarded time $t_{frame} - r_{ext}$, whereas the lower time axis has been shifted such that the $(2, 2)$ mode reaches peak amplitude at $t = 0$. The four vertical lines indicate the retarded times corresponding to the four snapshots of $\log|\Psi_4|$ in the orbital plane of a $q = 3$ binary shown in panels **e-h**. Bright yellow denotes large values of $|\Psi_4|$, while dark purple regions denote zeroes. The snapshots also show the horizon surfaces in black. As can be clearly seen in the inset of panel **e**, the remnant BH is initially highly asymmetric. In the same frame, the *trident* structure of $|\Psi_4|$ can be seen on the bottom right side of the horizon with its most prominent arm aligned with the *cusp*. The black arrow points along the kick-on direction.

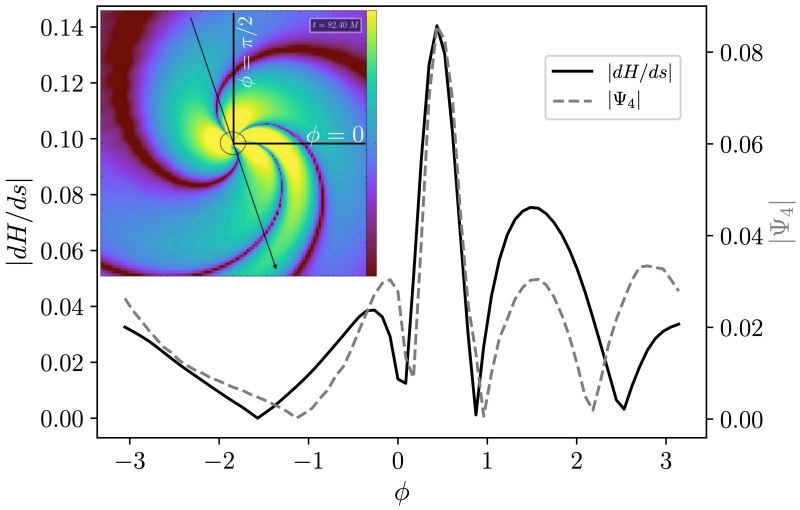

Figure 3.4: The main panel shows $|\Psi_4|$ on the intersection of the orbital plane and the common apparent horizon, along with the magnitude of the derivative of the mean curvature $|dH/ds|$ of the horizon along the same curve for a $q = 3$ binary $5\,M$ after the horizon forms. Both are shown as a function of the azimuthal angle ϕ. The parameter s denotes the arc-length along the equator, ad described in Section 3.1. The inset shows the corresponding snapshot of $|\Psi_4|$ in the orbital plane.

the top shows the retarded time $t_{frame} - r_{ext}$, where r_{ext} is the distance from the extraction surface to the emission source. When the arms of the trident Ψ_4 structure (particularly the central arm) cross the line-of-sight of an observer, that observer measures a chirp signal at a time r_{ext} later. This effect is also noticeable in the time series for h and Ψ_4 in the form of a short wavelength signal, consistent with the separation between wavefronts seen in Figure 3.2. Similarly whenever the back side of the horizon crosses the line-of-sight, it is followed by a frequency minimum after a time delay of r_{ext}. These observations strongly indicate that far-field GW signals, and particularly chirps and frequency minima, are directly connected to the line-of-sight passage of the arms of the Ψ_4 structure.

The alignment of the Ψ_4 central arm structure with the cusp on the apparent horizon suggests a relationship between Ψ_4 and the curvature of the horizon surface. To investigate this, we compare the value of Ψ_4 on the horizon surface and calculate both the mean curvature H and the Gaussian curvature K of the surface. Figure 3.4 shows Ψ_4 along with the magnitude of the derivative of the mean curvature $|dH/ds|$ along the equator $5\,M$ after

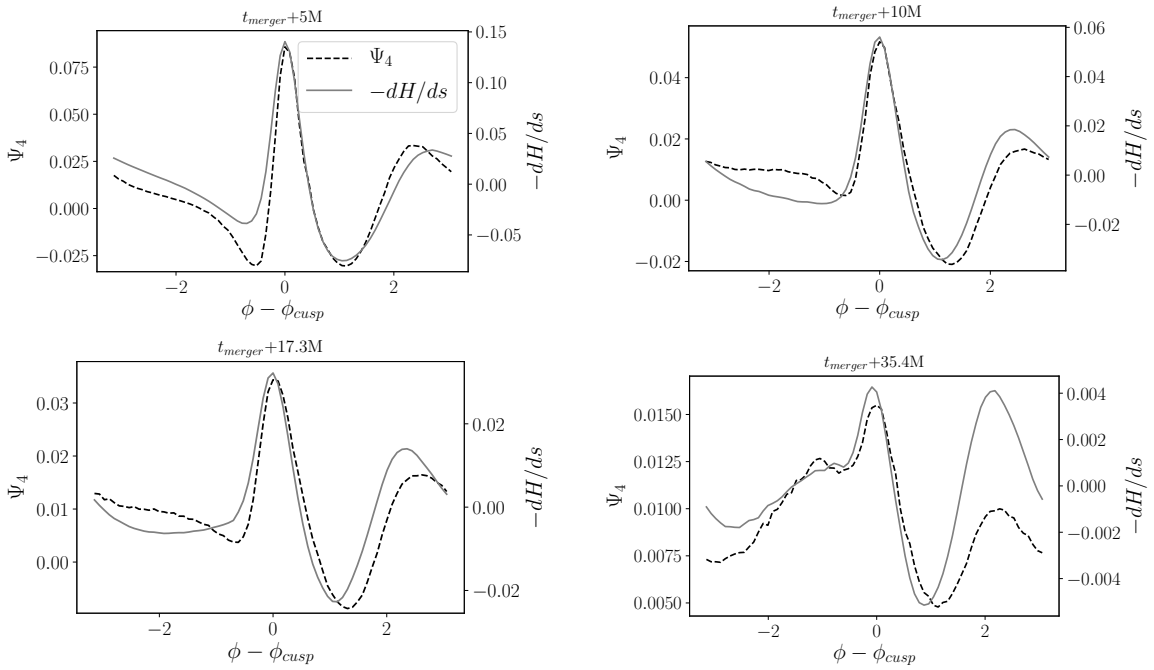

Figure 3.5: The correlation between Ψ_4 and dH/ds; similar to Figure 3.4, but shown at four different times: $5\,M$, $10\,M$, $17.3\,M$, and $35.4\,M$ after the formation of the common apparent horizon. Additionally, the ϕ-axis has been shifted by ϕ_{cusp} so that maximum of Ψ_4 (i.e. the central arm) is at $\phi - \phi_{cusp} = 0$.

the common horizon has formed. The parameter s denotes the arc-length along the horizons equator (see Section 3.1 for a detailed description of both the arc-length parameter and the two curvatures H and K). The four local maxima of $|\Psi_4|$ in the main panel correspond to the four arms of the emission structure, which is shown in the inset Ψ_4 snapshot. Clearly there is a close correlation between $|dH/ds|$ and $|\Psi_4|$. All four of the local maxima of $|\Psi_4|$ match up with the four local maxima of $|dH/ds|$. Each of the three Ψ_4 arms correspond to a nearby region of large $|dH/ds|$ that spans a similar angular size, with the maximum of $|dH/ds|$ (the cusp) matching up to the maximum of $|\Psi_4|$ (the central arm).

As can be seen in the four panels of Figure 3.5, this connection between Ψ_4 and dH/ds is not unique to any one moment in time. Based on the lower right panel ($35.4\,M$ after merger), we observe that this correlation degrades slightly long after the common horizon has formed. At late times the horizon has almost fully relaxed to equilibrium so the curvature is nearly uniform, with small dH/ds across the horizon surface. Emission is very weak for

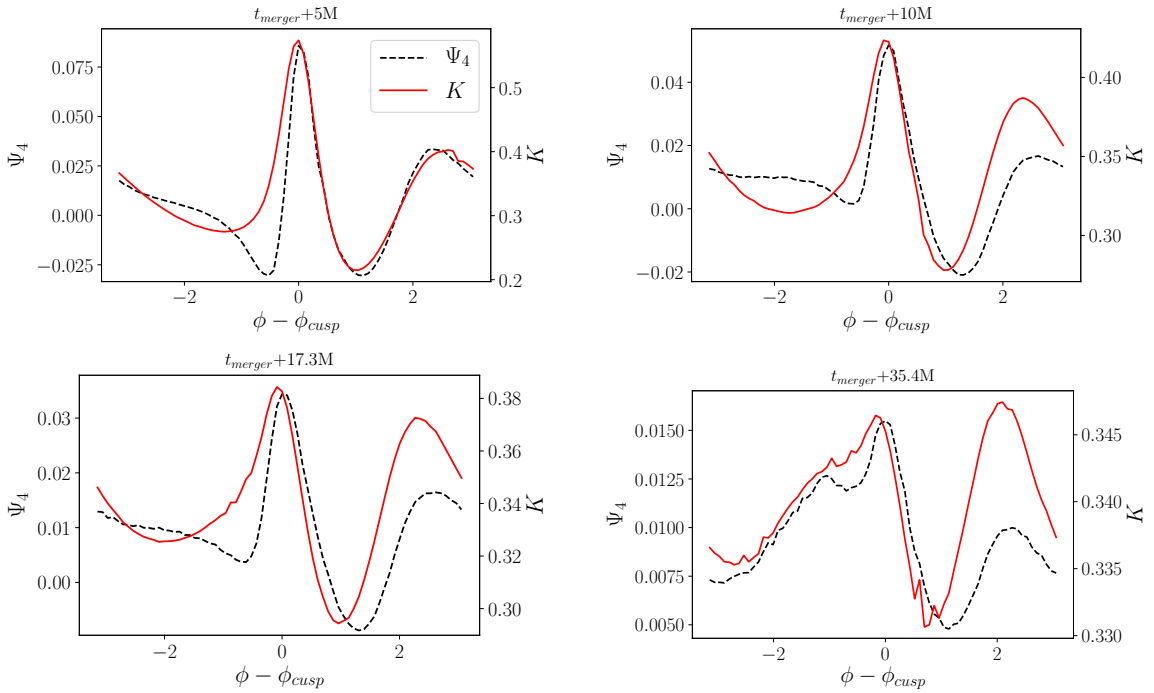

Figure 3.6: Values of Ψ_4 and the Gaussian curvature K on the intersection of the orbital plane and the final common horizon of a $q = 3$ binary as a function of the azimuthal angle ϕ. The panels **a-d** show times $5\,M$, $10\,M$, $17.3\,M$, and $35.4\,M$ after the common horizon forms, respectively.

the same reason, meaning that this degradation is easily attributed to numerical artifacts. Note that here we have chosen to plot Ψ_4 and $-dH/ds$, as opposed to taking their absolute values as in the previous figure, in order to show that the correlation holds smoothly over all ϕ. We chose to use the absolute values for the previous figure simply to facilitate visual comparison between the plot and the simulation snapshots.

As shown in Figure 3.6, the Ψ_4 arms also match with regions of locally extremal Gaussian curvature K, which, unlike the mean curvature, is coordinate independent and intrinsic to the horizon surface. Together, Figure 3.5 and Figure 3.6 provide compelling evidence that the rotation of the Ψ_4 corresponds precisely to the movement of extremal curvature regions on the horizon surface of the newly formed black hole.

Though I have only shown data from a $q = 3$ binary up until this point, we find that the correlations shown in Figure 3.5 and Figure 3.6 hold all of the mass ratios shown

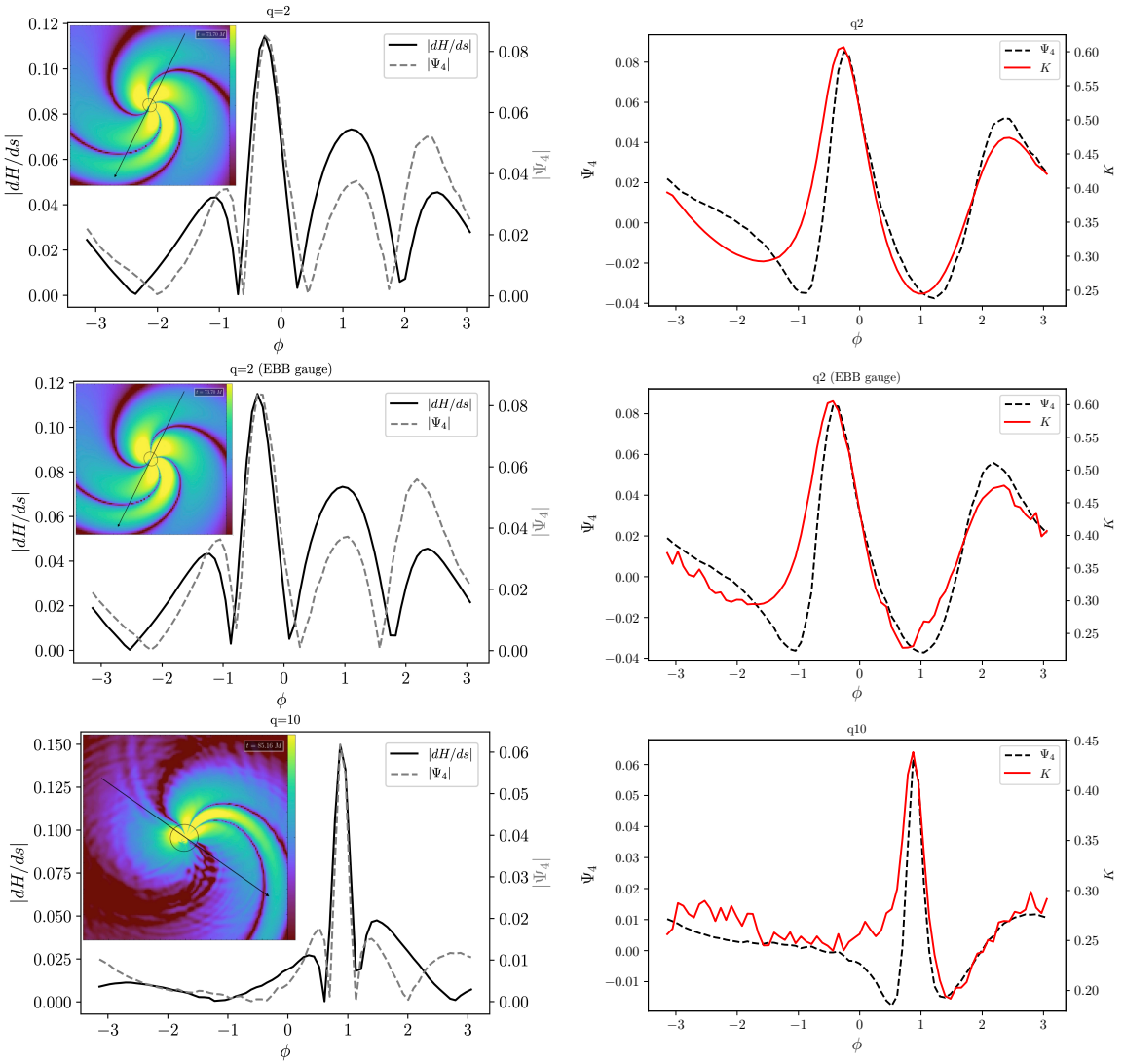

Figure 3.7: The panels on the left show the same as Figure 3.4, while the panels on the right show the same as Figure 3.6. The top two rows show the $q = 2$ case for two different gauge conditions, while the bottom row shows the $q = 10$ case.

in Figure 3.1, namely $q = 1.1, 2, 5, 6$ and 10. To demonstrate this, in the bottom row of Figure 3.7 we show results for the most extreme mass ratio $q = 10$. Moreover, while even the coordinate location of the apparent horizon itself depends on the gauge choice, we find that these results also hold in an alternative gauge. In the top two rows of Figure 3.7, I show results for the $q = 2$ case obtained using two different coordinate gauge conditions: the standard moving puncture gauge condition [16, 27] and a gauge with a dynamical shift condition [90] that is more appropriate for large mass ratios. The moving puncture gauge uses a Gamma-driving shift condition that depends on a damping parameter η with units of inverse mass. The range of appropriate values for η is a function of the BH masses, and thus for large mass ratios there is no one value that would lead to stability near both BHs. In this case we use position-dependent value of η to define a dynamical shift condition that is stable for larger mass ratios.

3.2.3 Observability of secondary chirps

For a GW signal $h(D;t)$ emitted by a source at distance D to be observable by a detector, it must have a high enough signal-to-noise ratio (SNR) to be considered a statistically significant deviation from the detector noise. The optimal SNR of the signal is defined as

$$\rho_{\rm opt}(D;t) = \sqrt{\langle h(D;t)|h(D;t)\rangle}, \tag{3.7}$$

where

$$\langle a|b\rangle = 4\,{\rm Re}\left(\int_{f_{min}}^{f_{cut}} df\,\frac{\tilde{a}(f)\tilde{b}^*(f)}{S_n(f)}\right) \tag{3.8}$$

denotes the inner product [91]. Here $\tilde{a}(f)$ denotes the Fourier transform of $a(t)$, an asterisk denotes complex conjugation, ${\rm Re}$ denotes the real part, and $S_n(f)$ is the one-sided power spectral density of the detector noise.

If the SNR is $\rho_{\rm opt} = 5$, this guarantees that the observed signal is a 5σ outlier from Gaussian noise. However, general long-duration realizations of LIGO detector noise are

both non-stationary and non-Gaussian. In addition to slow and smooth variations of the overall noise level over time, detector data can present with more abrupt noise glitches that may appear similar to transient astrophysical signals [92]. To overcome this, an SNR of ~ 10 for the *entire merger* signal is usually required in order to claim a GW detection [3].

In contrast, for shorter duration signals the detector noise is typically well approximated as both stationary and Gaussian [92]. For this analysis we are only concerned with the observability of the secondary chirp within a *previously detected* BBH signal. Such a signal is short enough that the noise may safely be assumed to be Gaussian. Furthermore, we can assume that signal is free of glitches since it has already passed the rigorous event validation process. As a result, the observable (at 5σ) distance D_o is given by the source distance at which $h(D_o; t)$ has an SNR of $\rho_{\text{opt}} = 5$.

In order to calculate the SNR of only the second chirp and not the entire signal, we cut our waveforms in the time domain at the post-merger frequency minimum according to the spectrograms. We then apply an aggressive window of width $\sim 10\,M$ to the beginning of the cut signal in order to avoid Gibbs phenomena in the Fourier transform due to the abrupt start. As a result, our estimates of ρ_{opt} are fairly conservative. We use a lower frequency cutoff of $f = 0.015/M$, which is well below the lowest frequency for which the second chirp has support based on Figure 3.1.

In Figure 3.8, I show the distance at which the secondary chirp would be observable at 5σ under the above assumption that it is part of a longer, confirmed GW observation. Here we consider four families of BBHs with varying mass ratio and total mass. We assume two Advanced LIGO detectors working at both current (solid) and design sensitivities (dashed) [93]. We also assume that the source has optimal sky-location, with the detector sitting in the orbital plane 55° away from the final kick direction, thereby maximizing the intensity of the secondary chirp. As a result, the observable distance curves shown in Figure 3.8 give an optimistic upper bound for sources with arbitrary sky-location.

The stars in Figure 3.8 denote the 10 BBH detections reported in GWTC-1 [3] (covering

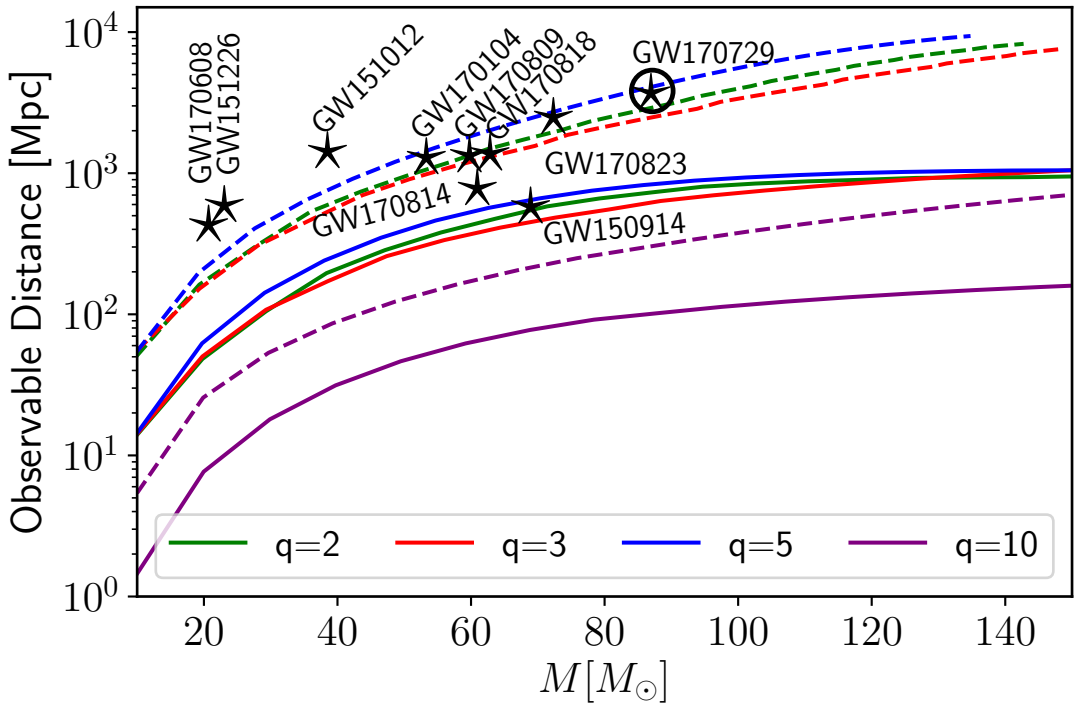

Figure 3.8: The source distance at which the secondary chirp of a GW signal can produce an SNR of $\rho_{\rm opt} = 5$ for a a collection of binaries with varying mass ratios and total masses (as measured in the detector frame). The observable distances are shown for two LIGO detectors working at early sensitivity (solid) and design sensitivity (dashed). We assume the sky-location of the source to be optimal, in that it maximizes the intensity of the secondary chirp.

observing runs O1 and O2). Of these events, GW170729 has the largest total mass and is consistent with a mass ratio $q = 2$ [3, 94]. While the observed signal does not present a secondary chirp, we find that such a chirp would be observable at design sensitivity for an *optimally oriented* copy of GW170729. Heavier asymmetric sources with $M = 300\,M_{\odot}$ would also present visible secondary chirps up to distances of $\sim 6\,Gpc$. Future work should extend this analysis to the events recently reported in GWTC-2 [4] (covering the first half of observing run O3), which includes 36 additional BBH detections with a wider range of mass ratios.

3.3 Conclusions

Observations of the merger and ringdown stages of BBHs have the unique ability to grant us access to the strongest regime of gravity, in which the most fundamental phenomenology of GR is on display through the dynamics of the highly distorted horizon of the remnant BH. Various connections between these dynamics and the observable GWs have been proposed and investigated [80, 79, 81, 78, 82, 83, 84, 85, 86], however to date, no explicit, concrete, observable GW features have been described. In this study, we propose the first such connection. We have shown that secondary chirps, which are non-trivial features of the post-merger GW emission of edge-on, asymmetric BBH mergers, are fundamentally connected to the presence of asymmetrically distributed extremal curvature regions on the dynamical horizon of the remnant. Furthermore, while post-merger chirps may resemble the signature of BH echoes [48], they have the important distinction not requiring anything more exotic than the standard BHs of GR.

To make this connection, we show that an asymmetric emission pattern emerges in the vicinity of the remnant BH horizon, with a three-armed trident structure on one side opposite a single arm on the other. These arm structures rotate along with the newly formed horizon, and their passage through an observers line-of-sight closely corresponds to the appearance of post-merger chirps, after accounting for GW propagation time. Finally, we show that

these arm structures coincide with locally extremal regions of the Gaussian curvature K and the mean curvature gradient dH/ds on the dynamical horizon, with the most prominent arm aligning with the globally extremal curvature region, or the cusp.

For all the mass-ratios we have considered, we find this feature is more prominent on the orbital plane of the binary, $\sim 55^{\circ}$ from the kick direction measured along the direction of the original orbit. Nevertheless, we assume that this will be subject to change if spinning BHs are considered [95, 96].

Finally, we show that Advanced LIGO detectors working at their design sensitivity would be able to observe post-merger chirps for a correctly oriented copy of the BBH GW170729 [3, 94], suggesting that such an observation may be feasible before the arrival of third generation detectors.

Part II

Tidal Disruption Events

Overview

Observations of TDEs have the potential to be a powerful tool to probe the demography of BHs in nearby galaxies. In galaxies with quiescent BHs, TDE signatures should be readily identifiable due to the absence of accretion-powered nuclear activity. In fact, in some cases TDEs may be the only way to determine the demographics of their central black holes. Observational evidence for TDEs is rapidly accumulating in UV [97, 98, 99, 100], X-ray [101, 102, 103, 104, 105], and visible band [106, 107] surveys. Some observations have shown indications of radio jet launching [102, 103, 108], while others have paved the way for new theoretical investigations by providing indications of structure in the light curve beyond the expected $t^{-5/3}$ power-law [104] or presenting spectra that do not match the properties expected of a simple TDE accretion disk [100, 109]. The work presented in this part is motivated by the increasing need for more simulations in order to interpret the rapidly growing number of potential TDE observations.

The foundation for TDE modeling was originally established by Rees [110], Phinney [111], and Evans and Kochanek [112]. Consider a star of mass m_* and radius r_* approaching a BH of mass m_h, most likely in a highly eccentric or parabolic orbit [110, 113]. The star will be tidally disrupted if it approaches the BH within the *tidal radius* r_t, defined as the separation at which the tidal force on the star is larger than its self gravity. Using a Newtonian approximation, the tidal radius is given by

$$r_t = r_* \left(\frac{m_h}{m_*}\right)^{1/3}. \tag{3.9}$$

It is customary to characterize the strength of a TDE encounter by the *penetration factor* β, which is defined as

$$\beta \equiv \frac{r_t}{r_p} = \frac{r_*}{r_p}\left(\frac{m_h}{m_*}\right)^{1/3}, \tag{3.10}$$

where r_p is the separation of the star and the BH at periapsis passage. Along with the gravitational radius of the BH $r_g = Gm_h/c^2$ (half the horizon radius for a non-spinning BH

and the full horizon radius for a maximally rotating BH), the quantities r_*, r_p, and r_t fully define the length scales of the TDE.

In Figure 3.9, I have included snapshots from two TDE simulations that provide an overview of a typical disruption event. The top panel shows a star passing just within the tidal radius ($\beta = 1$), while the bottom panel shows a much closer encounter ($\beta = 5$). As the star passes within the tidal radius of the BH it experiences tidal stretching along the line that connects the two objects. Meanwhile, the star experiences concurrent tidal compression in the direction normal to the orbital plane that depends strongly on the strength of the TDE encounter. Analytical estimates [114, 115, 116] suggest that under the influence of tidal compression the maximum temperature of the star scales as β^2. For a polytropic equation of state ($p = K\rho_0^\Gamma$) this indicates that the maximum density scales as $\beta^{2/(\Gamma-1)}$.

Tidal stretching leads to the formation of a quadrupole distortion of the star, which experiences a gravitational torque due to the fact that the line connecting the star and the BH rotates along the orbit. This torque induces a spread in the specific binding energy of the stellar material which has a half-width given by [117]

$$\begin{aligned} \Delta e &\simeq \frac{G m_h r_*}{r_t^2} \\ &\simeq G\, m_*^{2/3} r_*^{-1} m_h^{1/3}. \end{aligned} \tag{3.11}$$

The characteristic fallback time for the most tightly bound material ($e_{min} = -\Delta e$) to return to the BH is given by

$$\begin{aligned} t_{min} &\simeq \frac{2\pi G m_h}{(2|e_{min}|)^{3/2}} \\ &\simeq \frac{\pi}{\sqrt{2G}}\, r_*^{3/2} m_*^{-1} m_h^{1/2}. \end{aligned} \tag{3.12}$$

It is generally assumed [112] that the post-disruption distribution of mass per specific

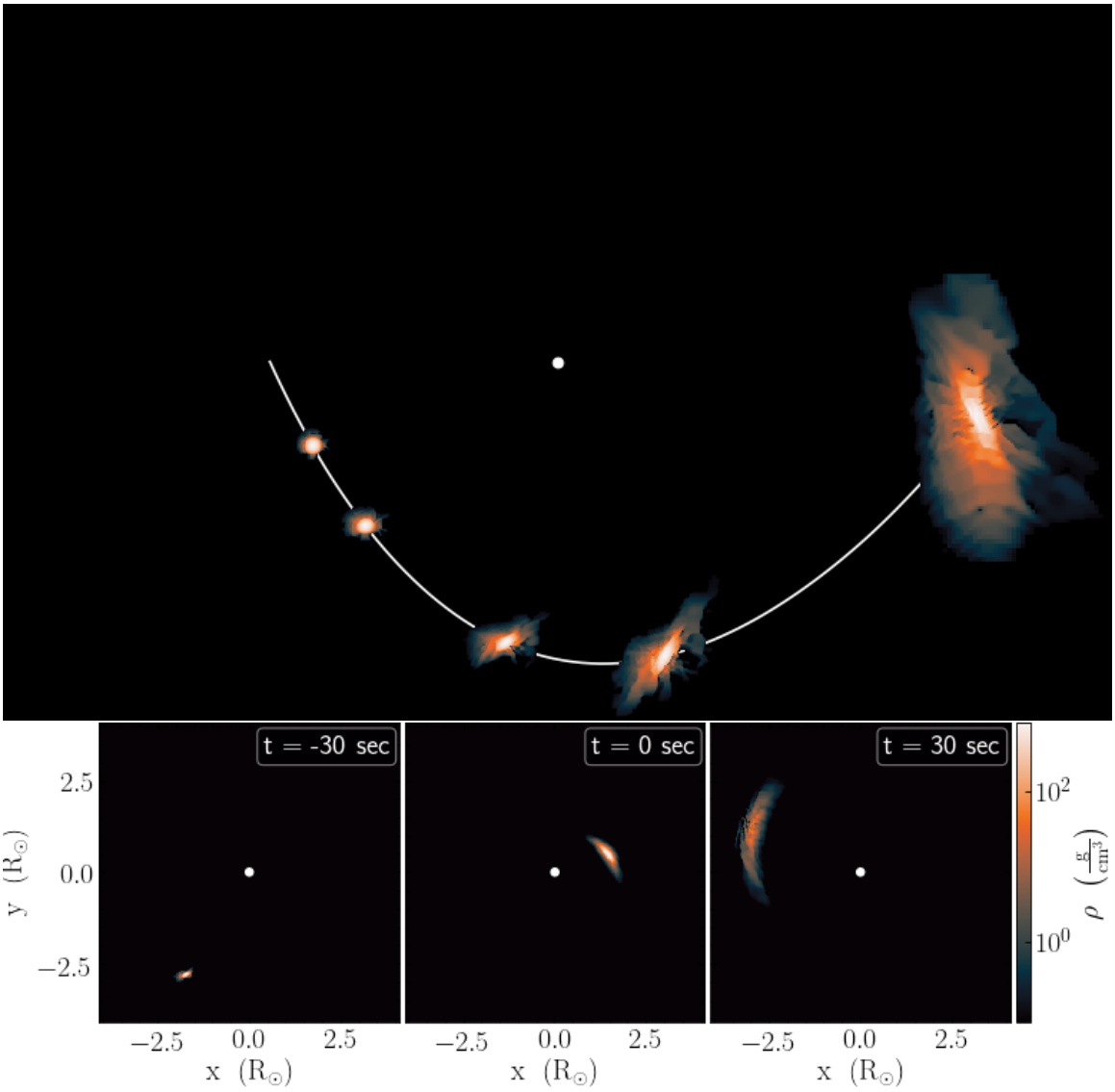

Figure 3.9: Schematic figures showing the disruption of a main sequence star by a BH. In the top panel I have overlaid snapshots of the disrupted star at five points on the shallow ($\beta = 1$) parabolic orbit (white line) around the BH (white circle). The bottom panel shows three individual snapshots of a close encounter ($\beta = 5$) thirty seconds before pericenter passage, at pericenter, and thirty seconds after (respectively, from left to right).

binding energy is uniform

$$\frac{dm}{de} \simeq \frac{m_*}{2\Delta e} \simeq \frac{m_*}{\left(2\pi G m_h\right)^{2/3}} \, t_{min}^{2/3}. \tag{3.13}$$

For a parabolic orbit $\langle e \rangle = 0$ so roughly half of the material remains bound to the BH after disruption. This assumption, along with the Keplerian relation

$$\frac{de}{dt} = \frac{1}{3} \left(2\pi G m_h\right)^{2/3} \, t^{-5/3} \tag{3.14}$$

provides an estimate for the accretion rate

$$\dot{m}_h \equiv \frac{dm_h}{dt} = \frac{dm}{de}\frac{de}{dt} \simeq \dot{m}_{max} \left(\frac{t}{t_{min}}\right)^{-5/3}, \tag{3.15}$$

where $\dot{m}_{max} \equiv m_*/(3t_{min})$. The $t^{-5/3}$ power law decay of Equation 3.15 is widely considered to be a trademark signature of TDEs [110, 112, 118, 119].

The difficulty involved in performing numerical simulations of TDEs primarily stems from the physical length and time scales involved in the encounters. The four length scales (r_*, r_p, r_t, and r_g) described above must all be properly resolved and are only commensurate for a small subset of encounters. Furthermore, at least several orbits are required after disruption for the debris to circularize. As a result, simulations must continue for at least $t_{circ} \sim 10 \; t_{min}$ [112] in order to capture the formation of the accretion disk. For the typical example of the disruption of a solar-type star by a $10^6 \; M_\odot$ BH, this corresponds to $t_{circ} \sim 1$ year. Ultra-close encounters ($r_p \sim r_g$) come with even more significant challenges, starting with the requirement of a fully relativistic treatment of gravity. One must also ensure that extreme tidal compression can be properly resolved.

To overcome these challenges, many previous studies have used smoothed particle hydrodynamics (SPH) methods, which by their nature overcome issues of scale and resolution. SPH has been used to investigate the $t^{-5/3}$ power-law decay of the accretion rate [112, 120],

disruptions of solar-type stars [118] and the stripped helium cores of giant stars [121] by supermassive black holes (SMBHs), disruptions of white dwarf stars by intermediate mass black holes (IMBHs) [119], and the disruption of rotating [122, 123] and magnetized [124] stars.

While SPH methods are a powerful tool for studying TDEs, fully coupling the particles to general relativity is still an open problem. As such, most SPH codes use a fixed spacetime background combined with Newtonian self-gravity for the fluid particles. In order to investigate ultra-close TDE encounters under full GR, one must use codes that are capable of solving the full set of Einstein's equations of GR coupled to GRHD or GRMHD. In the past, these fully coupled simulations have been used to study ultra-close disruptions of white dwarf stars by IMBHs and the potential for nuclear ignition due to tidal compression [20, 125].

In this part, I investigate TDEs using the computational infrastructure outlined in Section 1.3. In Chapter 4 I present BOOSTEDSTAR, a new initial data framework designed specifically with TDEs systems in mind. I describe the initial data method in detail in Section 4.2 followed by a series of code validation tests and their results in Section 4.3. Using this initial data framework, in Chapter 5 I present a study of the effects of stellar rotation in TDEs. In Section 5.1 I show that the tidal torque experienced by a prograde-rotating star can be much larger (by as much as a factor of two) than that experienced by a non-spinning or retrograde-rotating star. With these results in mind, in Section 5.2 I describe an analysis that provides preliminary indications that the effects of stellar rotation could be a significant driver of tidal debris circularization.

CHAPTER 4
BOOSTEDSTAR INITIAL DATA FRAMEWORK

In contrast to the majority of systems typically studied using NR, parabolic TDEs are somewhat unique in that they are not fully bound. While this presents its own complications during time evolution, it also allows for simpler methods of initial data construction. For example, if the initial separation between the star and the BH is sufficiently large, then the gravitational interaction between the two can be ignored to good approximation. Consequently, the initial data problem for the system is reduced to finding solutions for the star and BH in isolation and superimposing the two. While this can also be done with bound systems (such as BBHs), it would require such large initial separations that the resulting inspiral time would be impractical for NR simulations.

In practice, initial data for the BH is much easier to construct than that for the star. Given that $m_h \gg m_*$ for typical TDEs, the BH will be stationary since it is effectively the center of mass of the system. This means that all BH solutions permitted by GR are (in the absence of electric charge) spanned by four parameters: mass m_h and the spin angular momentum components J^i. These solutions have been studied extensively [67, 32, 31], and can be easily produced using the well established implementation of TWOPUNCTURES described in Section 1.3.

On the other hand, the space of potential solutions for an isolated star is vast and diverse. The simplest and most commonly used example is the time-invariant and spherically symmetric TOV star [126], which even still can produce significantly different structures for different equations of state. Solutions for isolated rotating stars [127, 128, 129] are also widely used in NR, though typically for rapidly rotating neutron stars. Beyond the solution itself, the star must be injected into a parabolic orbit around the BH, typically at relativistic ($\sim 0.1\,c$) speeds, without significantly disturbing hydrostatic equilibrium. It is difficult to

overstate the importance of this last point because nearly all aspects of TDEs that are worth studying numerically, such as extreme tidal compression or the energy distribution of stellar debris, depend sensitively on hydrostatic equilibrium remaining intact.

In this chapter, I describe the BOOSTEDSTAR initial data framework that I have created to construct TDE initial data using the above outlined approach. The framework constructs initial data for the star by applying a Lorentz boost transformation to the *stationary source description* defined in Section 4.1. BOOSTEDSTAR is highly generalizable in that it makes minimal assumptions about the isolated stellar model, requiring only the $3+1$ description of the source that would be required to as initial data for a stationary star. As examples, I outline the stationary source descriptions for TOV solutions and rotating RNS solutions in Sections 4.1.1 and 4.1.2, respectively.

In Section 4.2, I describe how to use the stationary source description to produce $3+1$ initial data for a star moving with the required velocity to be injected into a parabolic orbit around the BH. I generate the components of BOOSTEDSTAR that implement this process using NRPY+ [130], which is a Python package that uses a computer algebra system to generate highly optimized C code from symbolic equations.

The final component of BOOSTEDSTAR pipeline superimposes this boosted star solution with a stationary BH solution to produce initial data suitable for TDEs. BOOSTEDSTAR uses the existing implementation of the TWOPUNCTURES[31] spectral code in MAYA to produce a BH solution for a given mass and spin. Since they model isolated objects, both of these solutions are asymptotically flat, meaning that they approach flat space far from the star (BH):

$$\gamma_{ij} \to \delta_{ij} \tag{4.1}$$

$$K_{ij},\ \alpha,\ \beta^i,\ \partial_t\alpha,\ \partial_t\beta^i \to 0. \tag{4.2}$$

If the fields for the two solutions are simply added, then the resulting initial data will clearly

not be asymptotically flat. Instead, BOOSTEDSTAR expresses the $3+1$ fields as deviations from flat space and superimposes those. For example, the combined spatial metric is given by

$$\gamma_{ij} = \underbrace{\delta_{ij}}_{\text{flat space}} + \underbrace{\left(\gamma_{ij}^{(*)} - \delta_{ij}\right)}_{\text{star}-\text{flat space}} + \underbrace{\left(\gamma_{ij}^{(h)} - \delta_{ij}\right)}_{\text{BH}-\text{flat space}}. \tag{4.3}$$

While this process still does not generally yield a result that analytically satisfies the constraint equations, it produces consistently superimposed initial data with minimal constraint violations at separations typical to TDE simulations. To demonstrate this and evaluate the validity of BOOSTEDSTAR initial data, in Section 4.3 examine the constraint violations for TOV and RNS stars and show that they fall well within acceptable limits

4.1 Stationary source description

Let S (unprimed indices) denote the reference frame in which the star is stationary, and S' (primed indices) the frame in which it is boosted. In order to be used in BOOSTEDSTAR, an isolated star solution must be provided as a *stationary source description*, which is comprised of a complete $3+1$ description of the solution on the entire computational domain in S. Explicitly, the following fields must be specified:

- Spatial metric and its spatial derivatives: γ_{ij} and $\partial_l \gamma_{ij}$
- Extrinsic curvature: K_{ij}
- Gauge variables and their spatial derivatives: α, β^i, $\partial_k \alpha$, and $\partial_k \beta^i$
- Hydrodynamical primitives: ρ_0, p, ϵ, and v^i

Beyond this, BOOSTEDSTAR only enforces two further restrictions on the source solution: it must be both asymptotically flat and time-symmetric. The first restriction stems from the procedure (described in the previous section) used to superimpose the two solutions, which is only valid if both are asymptotically flat. On the other hand, the second restriction

is fundamental to the construction of the boosted star itself. As detailed in Section 4.2.2 below, the boosted NR initial data in S' must specify all of fields at a single coordinate time $x^{\mu'} = \left(0,\, x^{i'}\right)$, meaning that the corresponding points $x^{\mu} = \Lambda^{\mu}{}_{\mu'} x^{\mu'}$ in S are not simultaneous. As a result, the boosted initial data will not be consistent if the source is not time-symmetric.

Presently BOOSTEDSTAR includes the capability to generate source descriptions for TOV stars and rotating RNS solutions with the implementations detailed in the two subsections below. Both make use of existing external solvers, so entail a two step process. The first makes the appropriate calls to the external solver and stores the results as auxiliary grid functions that can be used by BOOSTEDSTAR. Neither the TOV or RNS solvers directly provide all the fields required for a source description, but instead produce auxiliary fields (such as metric potentials) from which the source description can be calculated. The second step is to perform this calculation, which I have implemented by symbolically mapping the auxiliary fields to the source description and then using NRPY+ to generate the implementation code.

For both the TOV and RNS solutions, I will exclusively use a polytropic equation of state for which the pressure and internal energy density are given by

$$p = K\rho_0^{\Gamma} \tag{4.4}$$

$$\epsilon = \frac{K\rho_0^{\Gamma-1}}{\Gamma - 1}. \tag{4.5}$$

4.1.1 TOV star

BOOSTEDSTAR uses the existing TOV solver included in MAYA, which was developed by Michael Clark and detailed in his thesis [131]. The TOV metric is both spherically symmetric and conformally flat, so it takes the form [22]

$$ds^2 = -\alpha^2(r)\, dt^2 + \Phi^4(r)\left(dr^2 + r^2 d\Omega\right), \tag{4.6}$$

where r is the radial coordinate centered on the star. For a given equation of state, TOV solutions are uniquely parameterized by the central density ρ_c of the star. The solver numerically integrates the constraint and continuity equations for the metric in Equation 4.6

$$\frac{1}{r^2}\partial_r\left(r^2\partial_r\Phi\right) = -2\pi\Phi^5\rho_H \tag{4.7}$$

$$\frac{1}{r^2}\partial_r\left(r^2\partial_r\Theta\right) = 2\pi\Theta\Phi^4\left(\rho_H + 6p\right) \tag{4.8}$$

$$\partial_r p = -\left(\rho_H + p\right)\left(\frac{\partial_r\Theta}{\Theta} - \frac{\partial_r\Phi}{\Phi}\right). \tag{4.9}$$

to produce a TOV solution in terms of $p(r)$, $\Phi(r)$, and $\Theta(r) = \alpha(r)\Phi(r)$. These solutions, along with $\partial_r\Theta$ and $\partial_r\Phi$, are then interpolated on to the Cartesian grid and stored as auxiliary grid functions.

The fluid source description is fully defined by $p(r)$ along with $v^i = 0$, with ρ_0 and ϵ determined by the equation of state (Equations 4.4 and 4.5). In terms of the auxiliary fields provided by the TOV solver, the metric source description is given by

$$\gamma_{ij} = \Phi^4\,\delta_{ij} \tag{4.10}$$

$$K_{ij} = 0 \tag{4.11}$$

$$\alpha = \Theta/\Phi \tag{4.12}$$

$$\beta^i = 0. \tag{4.13}$$

4.1.2 RNS *star*

BOOSTEDSTAR uses the publicly available RNS [129] code (version 2.0) to generate solutions for uniformly rotating stars. In spherical coordinates centered on the star, the metric for these solutions takes the form [132]

$$ds^2 = -e^{\gamma+\rho}\,dt^2 + e^{\gamma-\rho}r^2\sin^2\theta\left(d\phi - \omega\,dt\right)^2 + e^{2\alpha}\left(dr^2 + r^2\,d\theta^2\right), \tag{4.14}$$

where the metric potentials ρ, γ, α, and ω are functions of r and θ that are computed by RNS. These solutions are both stationary and axisymmetric, with Killing vectors ∂_t and $\partial_\phi = -y\,\partial_x + x\,\partial_y$, respectively. For a given equation of state, RNS solutions are uniquely parameterized by the central density ρ_c of the star and oblateness, which is the ratio of the polar radius to the equatorial radius r_p/r_e.

The RNS calculates the solution on a uniform numerical grid using a compactified radial coordinate s and an angular coordinate μ defined by

$$r = r_e \left(\frac{s}{1-s} \right) \tag{4.15}$$

$$\mu = \cos\theta, \tag{4.16}$$

where r_e is again the equatorial radius of the star. This data is then interpolated onto the Cartesian grid and stored as auxiliary grid functions. During the interpolation process, all first derivatives of the solution with respect to s and μ are calculated and stored as well. In terms of these, derivatives with respect to the Cartesian coordinates are calculated using the chain rule with

$$\partial_i s = \frac{r_e}{(r+r_e)^2}\,\partial_i r \tag{4.17}$$

$$\partial_i \mu = \frac{1}{r}\left(\delta_{iz} - \mu\,\partial_i r\right). \tag{4.18}$$

Typically the goal is not to find an RNS solution with a specific oblateness, but rather a specific angular velocity Ω_* as measured by an observer at rest at infinity. To accomplish this, BOOSTEDSTAR iterates over RNS solutions to find the oblateness that gives the desired Ω_* using a method originally implemented in MAYA by Tanja Bode. Starting with a spherical solution, it first decreases the oblateness in decrements of 0.05 until it finds a star with $\Omega > \Omega_*$. This allows it to bracket the desired solution, which can then found using Ridder's method [133].

For the metric source description in Cartesian coordinates, the spatial components of the metric shown in Equation 4.14 are

$$\gamma_{ij} = g_{ij} = \begin{pmatrix} \left(x^2 e^{2\alpha} + y^2 e^{\sigma}\right)/\bar{r}^2 & xy\left(e^{2\alpha} - e^{\sigma}\right)/\bar{r}^2 & 0 \\ xy\left(e^{2\alpha} - e^{\sigma}\right)/\bar{r}^2 & \left(x^2 e^{\sigma} + y^2 e^{2\alpha}\right)/\bar{r}^2 & 0 \\ 0 & 0 & e^{2\alpha} \end{pmatrix}, \tag{4.19}$$

where $\sigma = \gamma - \rho$ and $\bar{r} = \sqrt{x^2 + y^2}$ is the distance to the axis of rotation. Similarly

$$\alpha = \left(-g^{tt}\right)^{-1/2} = e^{\rho+\sigma/2} \tag{4.20}$$

$$\beta^i = \alpha^2 g^{ti} \quad = -\omega\, \partial_\phi{}^i. \tag{4.21}$$

Finally, rewriting Equation 1.9 I calculate the extrinsic curvature using

$$K_{ij} = \frac{1}{2\alpha}\left(D_i\beta_j + D_j\beta_i - \partial_t\gamma_{ij}\right), \tag{4.22}$$

with Equations 4.19 to 4.21, along with the fact that $\partial_t\gamma_{ij} = 0$.

For uniform rotation, the fluid four-velocity can be written as a linear combination of the two Killing Vectors [134]

$$u^\mu = \left(\frac{e^{-\sigma}}{e^{2\rho} - (\Omega-\omega)^2 r^2 \sin^2\theta}\right)^{1/2} \left(\partial_t{}^\mu + \Omega\, \partial_\phi{}^\mu\right), \tag{4.23}$$

where again $\Omega = u^\phi/u^t$ is the angular velocity of the fluid as measured by an observer at rest at infinity and the prefactor results from normalization $u_\mu u^\mu = -1$. Transforming to Cartesian coordinates and using the lapse and shift shown in Equations 4.20 and 4.21, this corresponds to an Eulerian fluid velocity

$$v^i = (\Omega - \omega)\, e^{-(\rho+\gamma)/2}\, \partial_\phi{}^i. \tag{4.24}$$

The hydrodynamical description of an RNS solution is provided in terms of the pressure p along with the energy density and enthalpy, which are given by

$$e = \rho_0 \left(1 + \epsilon\right) \tag{4.25}$$

$$H = \int_0^p \frac{c^2 dp'}{e + p'}, \tag{4.26}$$

respectively. For a polytropic equation of state (Equations 4.4 and 4.5), Equation 4.26 integrates to

$$H = \log\left(1 + \left(\frac{\Gamma K}{\Gamma - 1}\right)\rho_0^{\Gamma - 1}\right). \tag{4.27}$$

The rest mass density ρ_0 and internal energy density ϵ can be expressed in terms of the provided quantities (p, e, and H) as

$$p = p \tag{4.28}$$

$$\rho_0 = \left(e + p\right) e^{-H} \tag{4.29}$$

$$\epsilon = \frac{p}{\rho_0 \left(\Gamma - 1\right)}. \tag{4.30}$$

4.2 Construction of boosted star solution

In this section I describe how the BOOSTEDSTAR framework applies a Lorentz boost to a stationary star and uses the transformed solution it to construct initial data in which the star moves with velocity ξ^i with respect to a stationary observer. A high level overview of this process can be seen in Figure 4.1.

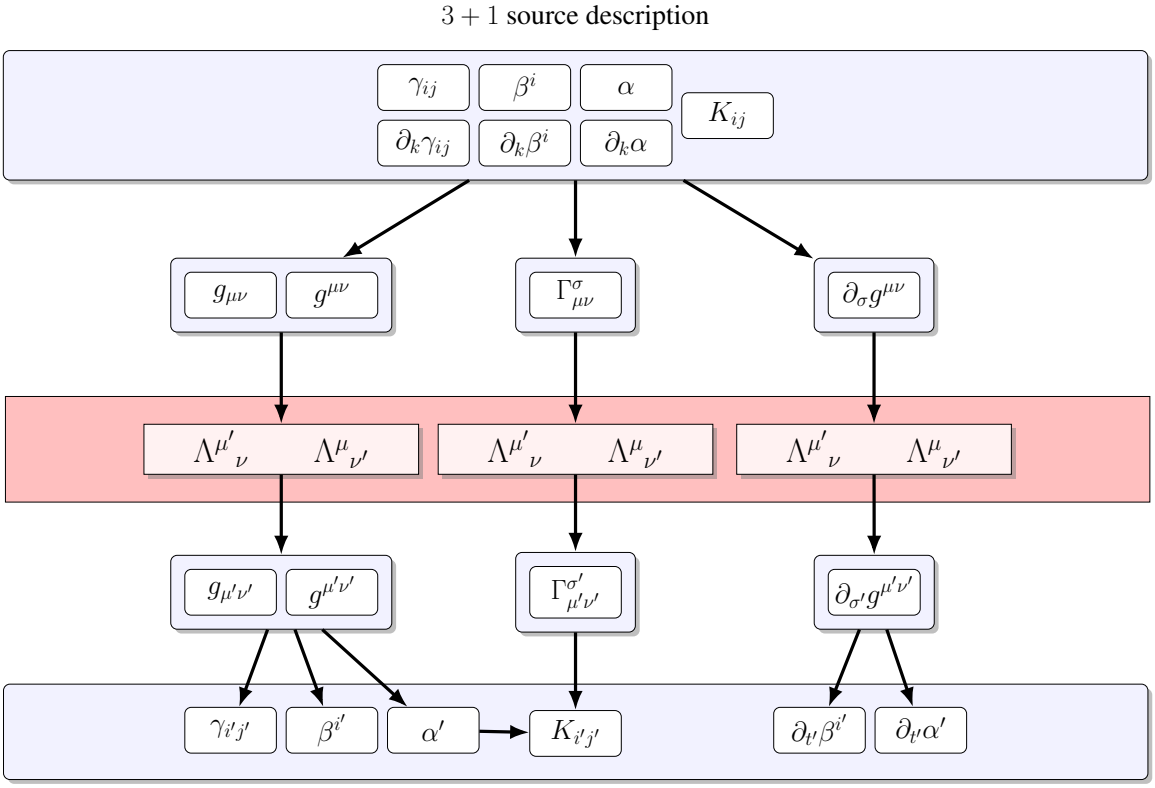

Figure 4.1: Overview of the process used by BOOSTEDSTAR to produce initial data for a boosted star from a stationary source description.

This section is organized into four subsections, each describing a step in the boosted star construction:

1. **Section 4.2.1**: Reconstruct $g_{\mu\nu},\ g^{\mu\nu},\ \partial_\sigma g^{\mu\nu}$ and the connection $\Gamma^\sigma_{\mu\nu}$
2. **Section 4.2.2**: Transform to S' using the boost transformation Λ
3. **Section 4.2.3**: Evaluate the boosted $3+1$ fields from the transformed metric quantities
   (a) Decompose $g_{\mu'\nu'}$ into $\gamma_{i'j'},\ \alpha'$, and $\beta^{i'}$
   (b) Calculate $\partial_{t'}\alpha'$ and $\partial_{t'}\beta^{i'}$ from $\partial_{\sigma'}g_{\mu'\nu'}$
   (c) Calculate $K_{i'j'}$ from α' and $\Gamma^{t'}_{i'j'}$
4. **Section 4.2.4**: Calculate the hydrodynamical fields in S'

4.2.1 Reconstruction of the four-metric and its connection

In terms of the $3+1$ metric and gauge quantities γ_{ij}, α, and β^i, the four-metric is given by[1]

$$g_{\mu\nu} = \begin{pmatrix} -\alpha^2 + \gamma_{ij}\beta^i\beta^j & \gamma_{ij}\beta^j \\ \gamma_{ij}\beta^i & \gamma_{ij} \end{pmatrix} \tag{4.31}$$

and its inverse by

$$g^{\mu\nu} = \begin{pmatrix} -1/\alpha^2 & \beta^i/\alpha^2 \\ \beta^j/\alpha^2 & \gamma^{ij} - \beta^i\beta^j/\alpha^2 \end{pmatrix}, \tag{4.32}$$

[1] See Section 1.2 for details.

where I have obtained γ^{ij} by numerically inverting γ_{ij}. Similarly, the Christoffel symbols in S can be expressed as [135]

$$\Gamma^t_{tt} = \alpha^{-1}\left(\partial_t\alpha + \beta^m\partial_m\alpha - \beta^m\beta^n K_{mn}\right) \tag{4.33}$$

$$\Gamma^t_{ti} = \alpha^{-1}\left(\partial_i - \beta^m K_{im}\right) \tag{4.34}$$

$$\Gamma^t_{ij} = -\alpha^{-1}K_{ij} \tag{4.35}$$

$$\Gamma^k_{tt} = \alpha\gamma^{ki}\left(\partial_i\alpha - 2\beta^j K_{ij}\right) - \beta^k\Gamma^t_{tt} + \partial_t\beta^k + \beta^i D_i\beta^k \tag{4.36}$$

$$\Gamma^k_{it} = -\alpha^{-1}\beta^k\left(\partial_i\alpha - \beta^j K_{ij}\right) - \alpha\gamma^{kj}K_{ij} + D_i\beta^k \tag{4.37}$$

$$\Gamma^k_{ij} = {}^{(3)}\Gamma^k_{ij} + \alpha^{-1}\beta^k K_{ij}, \tag{4.38}$$

where

$${}^{(3)}\Gamma^k_{ij} = \frac{1}{2}\gamma^{km}\left(\partial_i\gamma_{jm} + \partial_j\gamma_{im} - \partial_m\gamma_{ij}\right) \tag{4.39}$$

are the connection coefficients for the spatial metric.

Even though only $\partial_\sigma g^{\mu\nu}$ is needed, it is actually simpler to calculate $\partial_\sigma g_{\mu\nu}$ from Equation 4.31 and use it to calculate $\partial_\sigma g^{\mu\nu}$ than to do so directly from Equation 4.32, given that the goal is to express the result terms of the given $3+1$ fields and their derivatives. This is most apparent for the time derivatives

$$\partial_t g_{tt} = \beta^i\beta^j\partial_t\gamma_{ij} \tag{4.40}$$

$$\partial_t g_{ti} = \beta^j\partial_t\gamma_{ij} \tag{4.41}$$

$$\partial_t g_{ij} = \partial_t\gamma_{ij}, \tag{4.42}$$

which all depend on the extrinsic curvature through Equation 1.9.

The remaining spatial derivatives are given by

$$\partial_k g_{tt} = -2\alpha\partial_k\alpha + \beta^i\beta^j\partial_k\gamma_{ij} + 2\gamma_{ij}\beta^i\partial_k\beta^j \tag{4.43}$$

$$\partial_k g_{ti} = \gamma_{ij}\partial_k\beta^j + \beta^j\partial_k\gamma_{ij} \tag{4.44}$$

$$\partial_k g_{ij} = \partial_k\gamma_{ij}. \tag{4.45}$$

These can be used to calculate the necessary components by differentiating the identity $g_{\mu\alpha}g^{\alpha\nu} = \delta^\mu_\nu$ to find

$$\partial_\sigma g^{\mu\nu} = -g^{\mu\alpha}g^{\nu\beta}\partial_\sigma g_{\alpha\beta}. \tag{4.46}$$

4.2.2 Lorentz boost transformation

The Lorentz boost transformation is fully specified by the boost parameter ξ^i, which is equivalent to the velocity of the boosted star in S'. Keep in mind that the boost parameter is a *symbol* and not a true vector as it appears, since it cannot be transformed between reference frames. Rather, I will define all of the symbols

$$\xi^i = \xi^{i'} = \xi_i = \xi_{i'} \tag{4.47}$$

to be equivalent. As a result, special care must be taken with indices on ξ in order to maintain consistency. To satisfy Equation 4.47, indices of ξ must be raised, lowered, and contracted with the Kronecker delta δ instead of the metric. Furthermore, I extend the Kronecker delta to allow mixed indices (from S and S') by treating the corresponding components (i.e. z and z') as the same

$$\delta_{i'j} = \delta_{ij}, \tag{4.48}$$

meaning that $\delta_{x'x} = \delta_{xx} = 1$, while $\delta_{x'y} = \delta_{xy} = 0$. For example, it is convenient to define the Lorentz factor of the boost

$$\gamma_b = \frac{1}{\sqrt{1-\xi^2}}, \tag{4.49}$$

where the contraction is given by

$$\xi^2 = \xi_i \xi^i = \delta_{ij} \xi^i \xi^j. \tag{4.50}$$

For a given boost parameter ξ^i, the transformation matrix is given by [136]

$$\Lambda^{\mu'}{}_{\nu} = \begin{bmatrix} \gamma_b & \gamma_b\, \xi_x & \gamma_b\, \xi_y & \gamma_b\, \xi_z \\ \gamma_b\, \xi^{x'} & 1 + \frac{\xi^{x'} \xi_x (\gamma_b - 1)}{\xi^2} & \frac{\xi^{x'} \xi_y (\gamma_b - 1)}{\xi^2} & \frac{\xi^{x'} \xi_z (\gamma_b - 1)}{\xi^2} \\ \gamma_b\, \xi^{y'} & \frac{\xi^{y'} \xi_x (\gamma_b - 1)}{\xi^2} & 1 + \frac{\xi^{y'} \xi_y (\gamma_b - 1)}{\xi^2} & \frac{\xi^{y'} \xi_z (\gamma_b - 1)}{\xi^2} \\ \gamma_b\, \xi^{z'} & \frac{\xi^{z'} \xi_x (\gamma_b - 1)}{\xi^2} & \frac{\xi^{z'} \xi_y (\gamma_b - 1)}{\xi^2} & 1 + \frac{\xi^{z'} \xi_z (\gamma_b - 1)}{\xi^2} \end{bmatrix} \tag{4.51}$$

and its inverse by

$$\Lambda^{\mu}{}_{\nu'} = \begin{bmatrix} \gamma_b & -\gamma_b\, \xi_{x'} & -\gamma_b\, \xi_{y'} & -\gamma_b\, \xi_{z'} \\ -\gamma_b\, \xi^{x} & 1 + \frac{\xi^{x} \xi_{x'} (\gamma_b - 1)}{\xi^2} & \frac{\xi^{x} \xi_{y'} (\gamma_b - 1)}{\xi^2} & \frac{\xi^{x} \xi_{z'} (\gamma_b - 1)}{\xi^2} \\ -\gamma_b\, \xi^{y} & \frac{\xi^{y} \xi_{x'} (\gamma_b - 1)}{\xi^2} & 1 + \frac{\xi^{y} \xi_{y'} (\gamma_b - 1)}{\xi^2} & \frac{\xi^{y} \xi_{z'} (\gamma_b - 1)}{\xi^2} \\ -\gamma_b\, \xi^{z} & \frac{\xi^{z} \xi_{x'} (\gamma_b - 1)}{\xi^2} & \frac{\xi^{z} \xi_{y'} (\gamma_b - 1)}{\xi^2} & 1 + \frac{\xi^{z} \xi_{z'} (\gamma_b - 1)}{\xi^2} \end{bmatrix} \tag{4.52}$$

By construction, the center of mass of the star is at the same coordinate location in both frames $x^i_* = x^{i'}_*$, which is not necessarily the origin of the coordinate system. To ensure this, and to minimize coordinate deformation of the star, the boost transformations are applied relative to x^i_*. Explicitly,

$$x^\mu = x^\mu_* + \Lambda^{\mu}{}_{\nu'} \left(x^{\nu'} - x^{\nu'}_* \right), \tag{4.53}$$

where $x^{\mu'}_* = \left(0,\, x^{i'}_*\right)$. Also note that the NR initial data in S' needs to specify all of the fields on a single space-like hypersurface with constant coordinate time, or at coordinates $x^{\mu'} = \left(0,\, x^{i'}\right)$. The corresponding points in S will *not* be simultaneous with $x^\mu = (t(x^i),\, x^i)$, but this can generally be ignored since the star is stationary in S.

The metric, its derivative, and the connection can then be transformed according to

$$g_{\mu'\nu'} = \Lambda^{\mu}{}_{\mu'}\Lambda^{\nu}{}_{\nu'}\, g_{\mu\nu} \tag{4.54}$$

$$g^{\mu'\nu'} = \Lambda^{\mu'}{}_{\mu}\Lambda^{\nu'}{}_{\nu}\, g^{\mu\nu} \tag{4.55}$$

$$\partial_{\sigma'} g^{\mu'\nu'} = \Lambda^{\sigma}{}_{\sigma'}\Lambda^{\mu'}{}_{\mu}\Lambda^{\nu'}{}_{\nu}\partial_{\sigma} g^{\mu\nu} \tag{4.56}$$

$$\Gamma^{\sigma'}_{\mu'\nu'} = \Lambda^{\sigma'}{}_{\sigma}\Lambda^{\mu}{}_{\mu'}\Lambda^{\nu}{}_{\nu'}\Gamma^{\sigma}_{\mu\nu}. \tag{4.57}$$

Note that while $g_{\mu\nu}$ and $g^{\mu\nu}$ are both tensors, $\partial_\sigma g^{\mu\nu}$ and $\Gamma^{\sigma}_{\mu\nu}$ are not. However, for this specific transformation both will transform as tensors due to the linearity of Λ. In general, Equations 4.56 and 4.57 do *not* hold for arbitrary coordinate transformations.

4.2.3 Decomposition into $3+1$ *quantities*

Using Equations 4.31 and 4.32 in the frame S', I then decompose the transformed four-metric as

$$\gamma_{i'j'} = g_{i'j'} \tag{4.58}$$

$$\alpha' = \left(-g^{t't'}\right)^{-1/2} \tag{4.59}$$

$$\beta^{i'} = (\alpha')^2 g^{t'i'}. \tag{4.60}$$

While I assume that the time derivatives derivatives $\partial_t\alpha$ and $\partial_t\beta^i$ vanish in S, this is generally not the case in S'. After differentiating Equations 4.59 and 4.60, these are given by

$$\partial_{t'}\alpha' = \frac{1}{2}\left(\alpha'\right)^3 \partial_{t'} g^{t't'} \tag{4.61}$$

$$\partial_{t'}\beta^{i'} = 2\alpha' g^{t'i'}\partial_{t'}\alpha' + \left(\alpha'\right)^2 \partial_{t'} g^{t'i'}. \tag{4.62}$$

Finally, to calculate the extrinsic curvature in S' consider the Christoffel symbols

$$\Gamma^{\sigma'}_{\mu'\nu'} = \frac{1}{2} g^{\sigma'\rho'} \left(\partial_{\mu'} g_{\nu'\rho'} + \partial_{\nu'} g_{\mu'\rho'} - \partial_{\rho'} g_{\mu'\nu'} \right). \tag{4.63}$$

In terms of $3+1$ quantities, the $\Gamma^{t'}_{i'j'}$ component satisfies

$$-\alpha' \Gamma^{t'}_{i'j'} = \frac{1}{2\alpha'} \left(D_{i'} \beta_{j'} + D_{j'} \beta_{i'} - \partial_{t'} \gamma_{i'j'} \right), \tag{4.64}$$

which along with Equation 1.9 gives

$$K_{i'j'} = -\alpha' \Gamma^{t'}_{i'j'}. \tag{4.65}$$

4.2.4 Calculation of the hydrodynamical quantities in S'

The hydrodynamical quantities ρ_0, p, and ϵ are all scalars, so the fields in S' are simply given by the fields at the corresponding points $x^i = x^i\left(x^{i'}\right)$ in S. For the fluid velocity, I first reconstruct the four-velocity using Equations 1.29 and 1.30

$$u^t = \alpha^{-1} \left(1 - \gamma_{ij} v^i v^j \right)^{-1/2} \tag{4.66}$$

$$u^i = u^t \left(\alpha v^i - \beta^i \right), \tag{4.67}$$

which transforms as a vector. The Eulerian fluid velocity and Lorentz factor in S' are then also given by Equations 1.29 and 1.30

$$v^{i'} = \frac{1}{\alpha'} \left(u^{i'}/u^{t'} + \beta^{i'} \right) \tag{4.68}$$

$$W' = \alpha' u^{t'}. \tag{4.69}$$

4.3 Code validation

In order to be used for TDE simulations, BOOSTEDSTAR initial data must not only satisfy the Hamiltonian and momentum constraints to an acceptable degree of approximation, but it must also model a hydrodynamically stable star with a center of mass velocity that is consistent with the boost parameter ξ^i. In this section, I describe a series of tests that demonstrate that BOOSTEDSTAR meets these expectations.

These code validation tests fall into two distinct categories: initial data only and time evolved. Since time evolution is not required to investigate constraint violations of the initial data, these tests are initial data only. On the other hand, validation of velocity and hydrodynamic stability of the star fundamentally requires time evolution.

All *initial data* test cases that follow are variations on a TDE system with a (non-spinning) $10^6\,M_\odot$ BH and a solar-type with a polytropic equation of state ($\Gamma = 4/3$, $K = 0.364\,M_\odot^{2/3}$). The BH is placed at the origin and the star on the $-x$ axis. A parabolic $\beta = 10$ encounter for this system would require the star to have $v/c \approx 0.16$ if injected into orbit at a distance of $1.5\,r_t$. The full computational domain extends out to $214\,r_g$ with a coarse resolution of $2.4\,r_g$. Both the star and the BH are covered by nine levels of refinement, with the finest level having a resolution of $0.01\,r_g \approx r_*/50$. Some of the test cases will include only the BH and not the star. For consistency, this grid structure (including the additional refinement levels covering where the absent star would be) will be the same for all *initial data only* tests.

For the time evolved tests, the ultimate goal is to measure the properties of the boosted star solution in the absence of any disruption by a BH. In this case, tests are based on the same solar-type star but rescaling the units to $1\,M = 10^5\,M_\odot$ so that the simulation length scales are more appropriate to $r_* \approx 4.7\,M$. The full computational domain extends out to $181\,r_g$ with a corse resolution of $2.5\,r_g$. The star is initially at the origin and covered by five levels of refinement, with the finest level having a resolution of $0.08\,r_g \approx r_*/50$. The boost

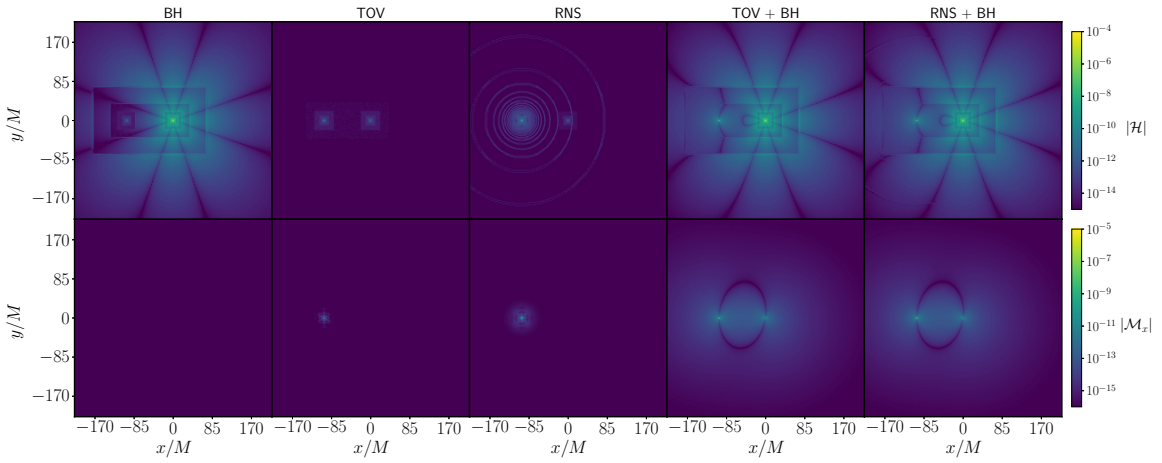

Figure 4.2: Snapshots of the constraint violation for five BOOSTEDSTAR initial data configurations. The top row shows the Hamiltonian constraint violation, while the bottom shows the momentum constraint.

parameter ξ^i is directed along the $+x$ axis for all time evolved tests.

For all cases involving RNS stars, the star rotates at 10% of the breakup angular velocity with the stellar rotation axis aligned with the z-axis.

As explained at the beginning of this chapter, BOOSTEDSTAR initial data will not be an exact solution to the Hamiltonian and momentum constraints. In order to gain a better understanding these constraint violations in the context of TDE simulations and determine whether or not they fall within an acceptable range, I consider here five different variations of the initial data configuration described above: BH only, TOV only, RNS only, BH with a TOV star, and BH with a RNS star. Figure 4.2 shows snapshots of the Hamiltonian (top row) and momentum (bottom row) constraint violation in the orbital plane for each variation. While only the last two of these model an actual TDE system, by looking at the BH and star solutions individually I can develop a better qualitative understanding of how these constraint violations arise. All configurations including a star use the boost parameter $|\xi^i| = 0.16$ corresponding to the $\beta = 10$ encounter mentioned above.

First, consider the BH solution in isolation (leftmost column). The momentum constraint is trivially satisfied since the BH is stationary and non-spinning. The Hamiltonian constraint violation shows clear indications of two distinct features: one delineated along the refinement

Table 4.1: L^2- and L^∞-norm constraint violations for five BOOSTEDSTAR initial data configurations.

Constraint	BH	TOV	RNS	BH + TOV	BH + RNS
$\|\mathcal{H}\|_2$	1.64×10^{-10}	4.23×10^{-13}	3.00×10^{-10}	1.38×10^{-9}	1.41×10^{-9}
$\|\mathcal{H}\|_\infty$	2.21×10^{-6}	2.08×10^{-7}	6.52×10^{-5}	2.56×10^{-4}	2.87×10^{-4}
$\|\mathcal{M}_x\|_2$	0	9.52×10^{-14}	2.96×10^{-11}	1.35×10^{-10}	1.38×10^{-10}
$\|\mathcal{M}_x\|_\infty$	0	4.61×10^{-8}	1.62×10^{-5}	2.53×10^{-5}	4.11×10^{-5}

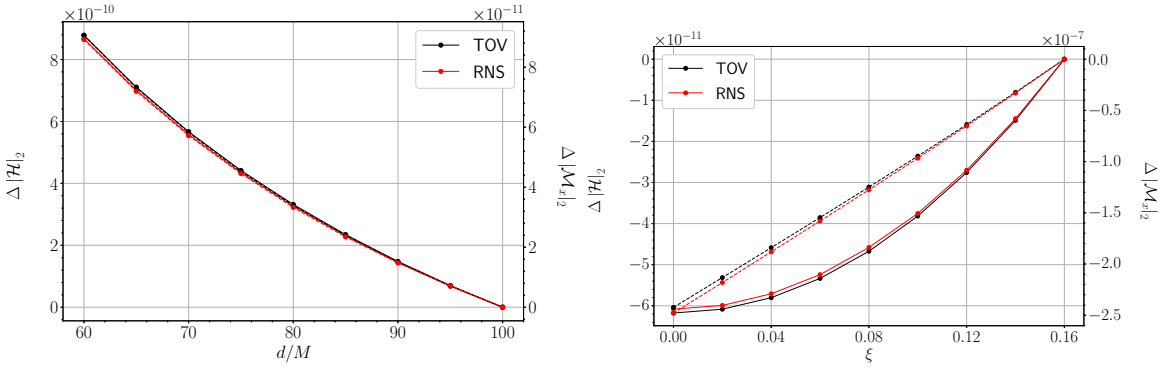

Figure 4.3: Constraint violations for BOOSTEDSTAR initial data at various separations and boost velocities. In the left panel the constraints are shown relative to their value at $d = 100\,M$, and in the right panel they are shown relative to $\xi = 0.16$.

boundaries and the other extending radially from the BH. The former is simply due to finite differencing truncation error, while the latter results from translating the BH solution from the coordinate system used by TWOPUNCTURES (see [31] for details) to the Cartesian grid. Consequently, both of these features will also be present in the superimposed data.

Moving next to the isolated star configurations, the constraint violations for TOV and RNS solutions appear qualitatively similar. For both, violations are most significant within a well-localized region centered on the stars while also appearing again near refinement boundaries. In addition, the RNS solution also shows increased violation (at a level similar to the truncation error) of the Hamiltonian constraint on a series of rings centered on the star. These features result from interpolating the RNS solution from the uniform grid $(s_i,\, \mu_i)$ (defined in Equation 4.15) to the Cartesian grid, with the radius of each ring corresponding to a value of s exactly halfway between two grid points s_i and s_{i+1}.

Finally, the two rightmost columns of Figure 4.2 correspond to superimposed BOOST-

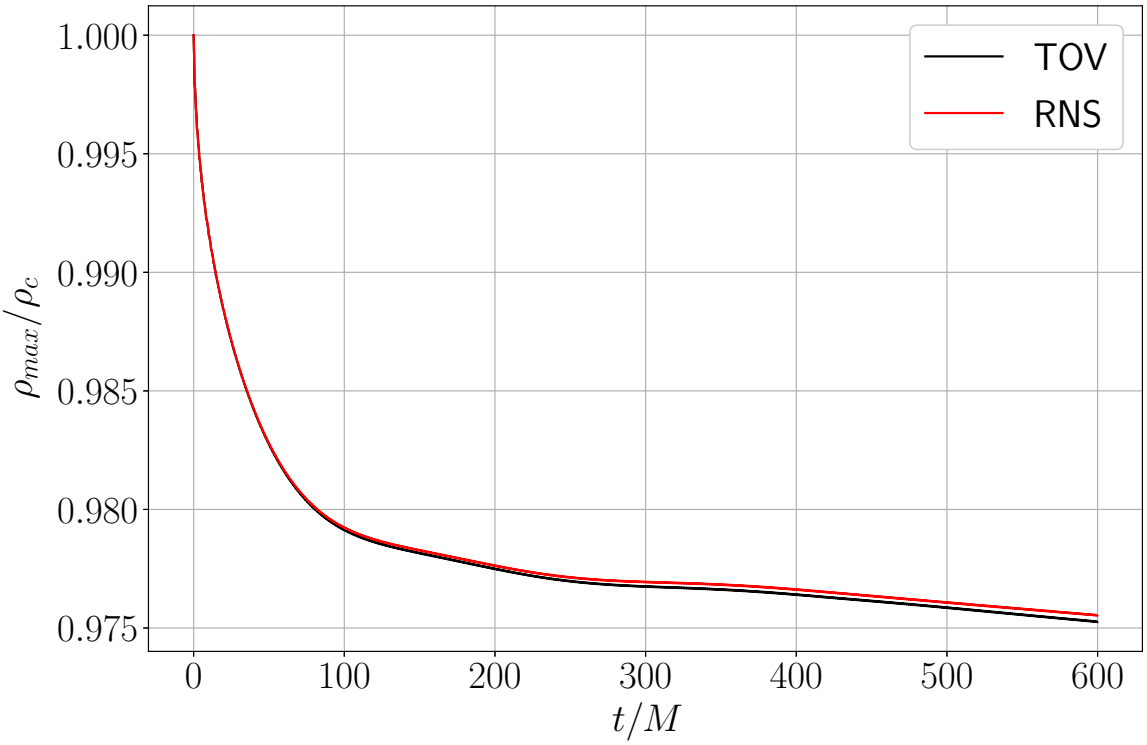

Figure 4.4: Central density change for both TOV and RNS BOOSTEDSTAR solutions.

EDSTAR initial data for TDEs. In addition to those from the star and BH in isolation, the Hamiltonian constraint violation displays additional features resulting from the superposition process. This is most evident along the x-axis between the two objects where the gravitational interaction between the two is the most non-linear.

Looking at the entire grid, Table 4.1 lists the L^2- and L^∞-norm constraint violations for each of these five configurations. The TOV is the most accurate of the isolated solutions, with both $|\mathcal{H}|_2$ and $|\mathcal{M}_x|$ falling about three orders of magnitude below the other two (disregarding the vanishing BH momentum constraint). For the Hamiltonian constraint, the RNS solution is commensurate with the BH.

Relative to this base configuration ($d = 100\,M$, $\xi = 0.16$), Figure 4.3 shows how the constraint violations change with decreasing separation binary separation d (left) and boost parameter ξ (right). As expected, violations become larger at shorter separations since gravitational interactions are ignored by the superposition process. Unsurprisingly, violations

also decrease with smaller ξ as the solutions approach those of an isolated stationary star.

Finally, the time evolved tests show that both the boosted TOV and RNS stars are stable and have the appropriate velocity. Over a period of $600\,M$, both stars maintained a center of mass velocity with $|v/\xi - 1| \leq 10^{-4}$. Furthermore, in Figure 4.4 I show the central densities of the two stars during time evolution. In both cases the central density drops initially by $\sim 2.5\%$ and then levels out, indicating that the boosted stars are hydrodynamically stable.

Across all of the BOOSTEDSTAR initial data considered in this section, including configurations suitable for TDE simulations, the constraint violations fall within $|\mathcal{H}|_2 \leq 2.3 \times 10^{-9}$ and $|\mathcal{M}_x|_2 \leq 2.3 \times 10^{-10}$.

CHAPTER 5

TIDAL DISRUPTION EVENTS AND STELLAR ROTATION

The large variety of TDE observations is no doubt due in part to the diverse population of stars available for disruption in galactic centers. As demonstrated by Guillochon and Ramirez-Ruiz [137], stellar structure plays a central role in the observational properties of a TDE.

The internal structure of a star depends not only on its mass, composition, and evolutionary stage, but also the stellar spin. For early-type stars specifically, observations indicate that a non-negligible fraction have significant stellar rotation [138]. Young stars have no mechanism to shed excess angular momentum due to the fact that magnetic breaking occurs on timescales on the order of the stellar lifetime [139]. Given the strong bias towards post-starburst galaxies as hosts for TDE observation [140], it is reasonable to expect a significant number of disruptions involving stars with high spins.

Additionally, there are many opportunities for a star to be spun-up in a nuclear star cluster. Through soft hyperbolic tidal encounters with other stars in the cluster, a solar-type main-sequence star can be spun-up to $\sim 10\% - 30\%$ of the breakup rate over the course of its lifetime [139].

Stars that enter the loss cone through the diffusive regime can be spun-up further by the tidal field of the BH over many orbits before full disruption actually occurs [123]. This occurs because the tidal field induces a quadrupole distortion [110] of the star that lags behind the direction to the BH, causing it to experience a tidal torque. Rough analytical estimates of this spin-up process indicate that it can result in a stellar spin that is on the order of the breakup rate [112], but the details of this process depend on the details of both the stellar structure and the encounter, and have not yet been fully investigated.

Our current understanding of TDE observations relies on the circularization timescale

being much shorter than the fallback timescale for bound debris, however the mechanism for this remains unclear at best [141]. Shock dissipation at the nozzle (lower mass BHs), relativistic precession ($r_p \sim r_g$), and dissipation through the magneto-rotational instability are all commonly proposed dissipation mechanisms which, even together, are not enough to ensure sufficiently fast circularization in some cases [142].

In this chapter, I investigate the role of stellar spin in TDEs using GRHD simulations performed with MAYA. I consider a $\beta = 1$ disruption of a main-sequence star with $m_* = 1.8\,M_\odot$ and $r_* = 1.8\,R_\odot$ by a $10^6\,M_\odot$ BH. The star is initially a distance of $1.5\,r_t \approx 100\,r_g$ from the BH and modeled as an RNS solution using a polytropic equation of state with $\Gamma = 4/3$. The rotation rate of the star varies across simulations and is described in terms of the breakup velocity

$$\Omega_K = \sqrt{\frac{Gm_*}{r_*^3}} \approx 1.3\ 1/\text{hr}. \tag{5.1}$$

I use the BOOSTEDSTAR framework described in Chapter 4 for initial data.

In Section 5.1 I calculate the tidal spin-up during weak/partial disruptions and show that the effect is stronger if the star already has a prograde rotation, thereby amplifying the population of spinning stars that can undergo full disruption. In Section 5.2 I show that when a prograde spinning star undergoes disruption, there are strong indications that the bound debris undergoes more self-intersections than if the star were not spinning, which would lead to an additional source of dissipation to speed up circularization. Finally, in Section 5.3 I describe the limitations of this analysis and propose a direction for future studies.

5.1 Tidal Spin-Up

During a TDE, the star will experience a torque due to the action of the tidal field on the deformed star. Based on the order of magnitude estimation of Evans and Kochanek [112], over the course of the encounter the star is spun up to acquire a prograde specific angular momentum of $\ell_s \sim \sqrt{r_* m_*}\beta^{3/2}$. While this estimation depends only on r_*, m_*, and β, the

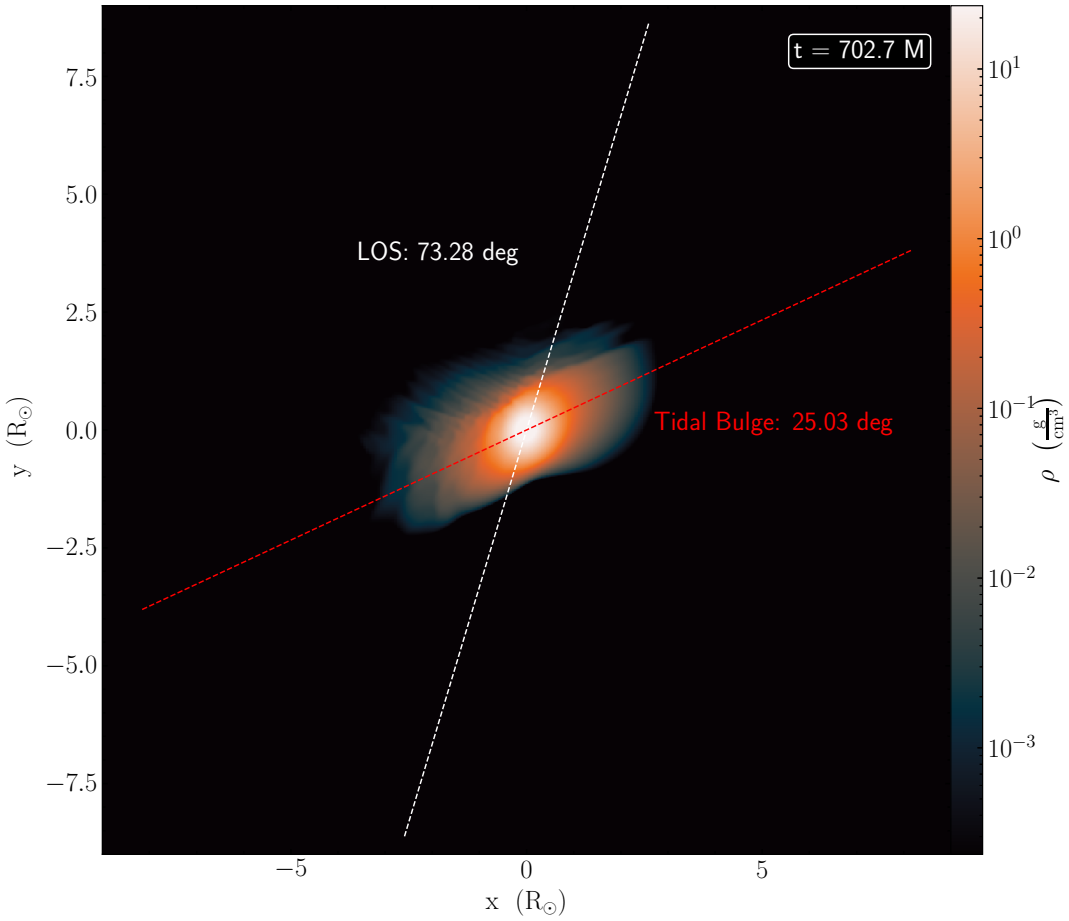

Figure 5.1: Tidal bulge axis (red) and line-of-sight to the BH (white) during disruption. All angles shown in this figure are measured counter-clockwise from the positive x-axis. In this snapshot, the lag angle is $\delta = 48.25$ deg.

reality of this spin-up process depends sensitively on the structure of the star and how it is deformed by the tidal field.

In order to see this, one can approximate the deformed star during disruption as a prolate spheroid [143] with average radius R and ellipticity $\epsilon = (r_e - r_p)/R$, where r_e and r_p are the equatorial and polar radii, respectively. The deformed star is assumed to be symmetric about the polar axis, which is aligned with the tidal bulge. Note that R is not the same as r_*, but is instead a result of the tidal deformation.

One can then expand the Newtonian gravitational potential of the star in muiltipoles

$$\phi_*(r,\theta) = \frac{Gm_*}{R}\sum_n J_n \left(\frac{R}{r}\right)^{n+1} P_n\left(\cos\theta\right) \tag{5.2}$$

$$J_n = -\frac{1}{m_* R^n}\int dV\, r^n P_n\left(\cos\theta\right)\rho(r,\theta), \tag{5.3}$$

where θ is the polar angle from the tidal bulge. Now consider a point during the disruption when the orbital separation is d and the lag angle between the tidal bulge and the BH line-of-sight is δ. To first order in the ellipticity, the gravitational potential of the star is given by

$$\phi_*(r,\theta) = -\frac{Gm_*}{r} + \frac{J_2}{2}\frac{Gm_* R^2}{r^3}\left[3\cos^2\left(\theta+\delta\right) - 1\right] + \mathcal{O}\left(\epsilon^2\right). \tag{5.4}$$

This setup is illustrated in Figure 5.1. The polar angle θ is measured clockwise from the tidal bulge axis (shown in red), and the angle δ is measured counter-clockwise from the tidal bulge axis to the line-of-sight to the BH (shown in white).

Using Equation 5.4, one can calculate the torque exerted on the BH by the gravitational field of the star as $-m_h \left.\frac{\partial\phi_*}{\partial\theta}\right|_{\theta=0,r=d}$, which, by the conservation of angular momentum, must be equal and opposite to the torque exerted on the deformed star by the BH. This leads to a specific torque on the star of

$$\tau_* = -\frac{3}{2}J_2\frac{Gm_h R^2}{d^3}\sin\left(2\delta\right) + \mathcal{O}\left(\epsilon^2\right). \tag{5.5}$$

Note that for a prolate spheroid $J_2 < 0$ and therefore $\tau_* > 0$ meaning that the star will acquire a prograde spin, as expected.

From Equation 5.5 one can see that, to first approximation, τ_* depends on the stellar structure through R, J_2, and the lag angle δ. Different stellar structures (i.e. different density profiles $\rho(r,\theta)$) will generally lead to different values for R and J_2, but also indirectly

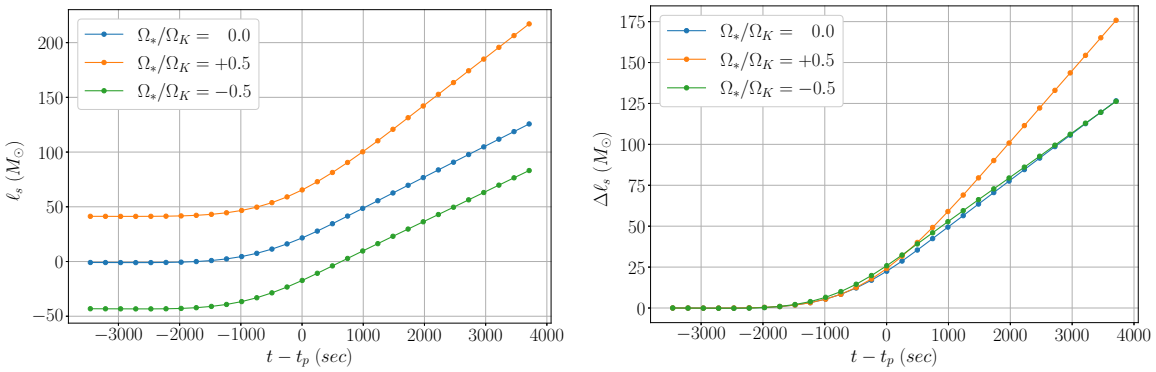

Figure 5.2: Specific rotational angular momentum of the star ℓ_s during disruption for the non-spinning case and the prograde/retrograde-spinning cases ($\Omega_*/\Omega_K = \pm 0.5$).

control how the star deforms during disruption and therefore how R and J_2 evolve with time. These results indicate that a spinning star should experience a different tidal torque than its non-spinning counterpart. In Figure 5.2 I show simulation data for the specific rotational angular momentum throughout disruption for an initially non-spinning star, and for stars with $\Omega_*/\Omega_K = \pm 0.5$. The data indicate that the tidal torque experienced by the star does indeed depend on the initial stellar rotation, with the prograde-spinning star experiencing nearly double the torque compared to its non-spinning and retrograde counterparts.

These numerical simulations can also shed some light on what exactly causes this difference in tidal torque. I find that the mean radius R and lag angle δ evolve nearly identically across all three cases, meaning that the difference has to stem from the multipole moment J_2. In Figure 5.3 I have plotted the value of $|J_2|$ for each case throughout the disruption. Initially, the moments for $\Omega_*/\Omega_K = \pm 0.5$ are very similar to each other but different from the non-spinning case. This is to be expected based on the density profiles of the initial stars. However, after pericenter passage the tidal disruption begins to significantly enhance $|J_2|$ for the prograde spinning star as compared to the other two cases. Ultimately this disparity grows to nearly a factor of two, which accounts for the increased tidal torque experienced by the prograde-spinning star.

In fact, this enhancement of $|J_2|$ stems from the same physical process described by Kagaya, Yoshida, and Tanganyika [122] and Golightly, Coughlin, and Nixon [123]: all

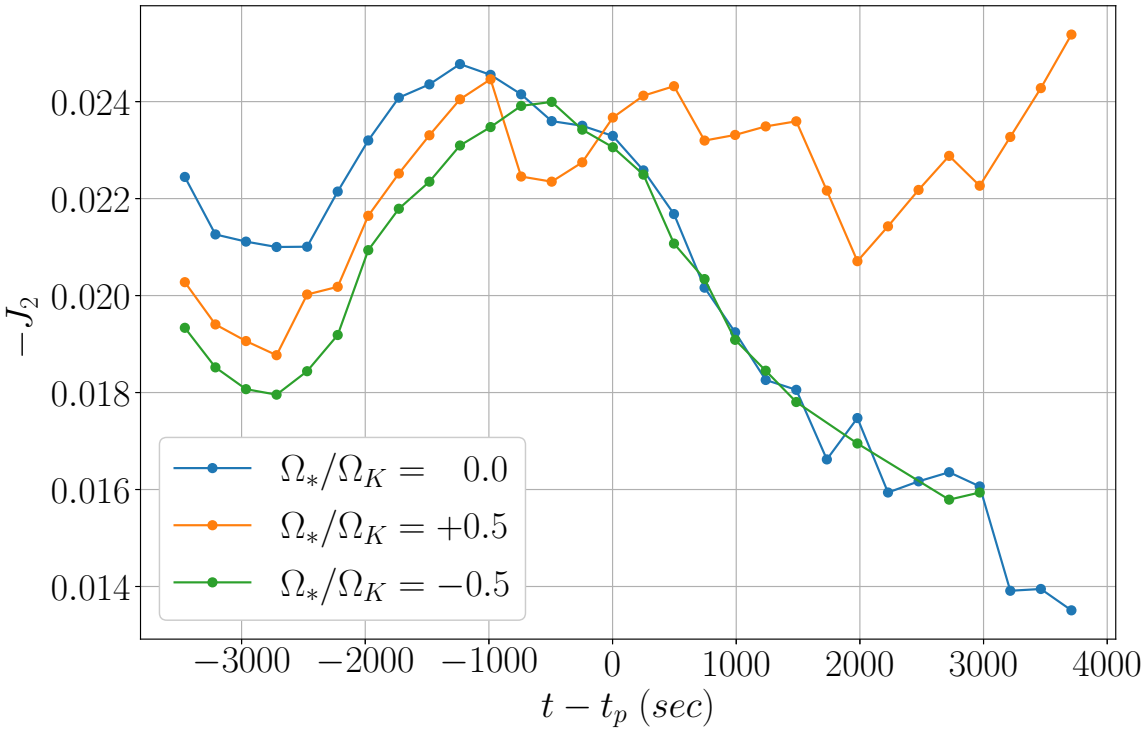

Figure 5.3: Evolution of the multipole moment J_2 for a non-spinning star and the prograde/retrograde-spinning cases $\Omega_*/\Omega_K = \pm 0.5$.

other things being equal, a prograde-spinning star is more easily disrupted than its non-spinning or retrograde-spinning counterparts, and will therefore result in a debris distribution that is less spatially compact. Based on these simulations, the maximum density of the debris is $\approx 5 - 10\%$ lower for the prograde-spinning case as a result of the disruption. From Equation 5.3 it is clear that a more extended matter distribution will have a larger $|J_2|$ due to the r^2 weighting of the density in the integrand.

5.2 Disruption of Rotating Stars

The generally accepted model of TDE emissions relies on the fact that the tidal debris circularizes much faster than the fallback timescale. Traditional pictures of debris circularization generally involve debris stream self-intersections due to relativistic precession, however these effects are not very strong unless pericenter passage is sufficiently close to the BH.

Another possible driver of circularization relies on the fact that the initial orbital energy-

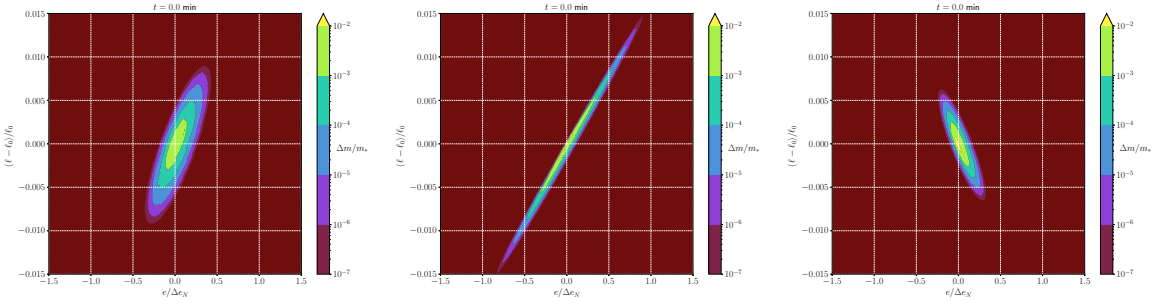

(a) $\Omega_* = 0$ (b) $\Omega_*/\Omega_k = +0.5$ (c) $\Omega_*/\Omega_k = -0.5$

Figure 5.4: Distribution of specific orbital energy e and specific orbital angular momentum ℓ of a star in a $\beta = 1$ orbit at a distance of $100\, r_g$ from the BH. Panel (a) shows a non-spinning star, while panels (b) and (c) show stars with $\Omega_*/\Omega_K = +0.5$ and -0.5, respectively.

momentum distribution of the stellar material depends on the stellar rotation Ω_*, as is shown in Figure 5.4. Here the specific orbital energy e (horizontal axis) is shown as a fraction of the Newtonian energy spread Δe_N (Equation 3.11) expected in a TDE encounter, and the specific orbital angular momentum ℓ (vertical axis) is given as a relative deviation from the center of mass value ℓ_0. The leftmost panel shows the distribution for a non-spinning star, for which the energy falls in the range $e/\Delta e_N \in (-0.5\, 0.5)$ and the angular momentum deviates from ℓ_0 by no more than 1%. The material on the side of the star closer to the BH is more bound and has lower orbital angular momentum, with the opposite being true on the other side.

When the star has a prograde rotation of $\Omega_*/\Omega_K = +0.5$, the material closer to the BH is moving more slowly relative to the BH than in the non-rotating case, since the rotational motion opposes that of the center of mass. This leads to material that is more bound with lower orbital angular momentum. On the far side of the star, the rotational motion is in the same direction as that of the center of mass, leading to less bound material with larger orbital angular momentum. In total, the prograde stellar rotation acts to stretch out the non-spinning energy-momentum distribution of Figure 5.4a to cover a larger range of both e and ℓ, as shown in Figure 5.4b. Here the energy falls in the range $e/\Delta e_N \in (-1, 1)$ and the angular momentum deviates from ℓ_0 by up to 1.5%. When this is the case, the fluid

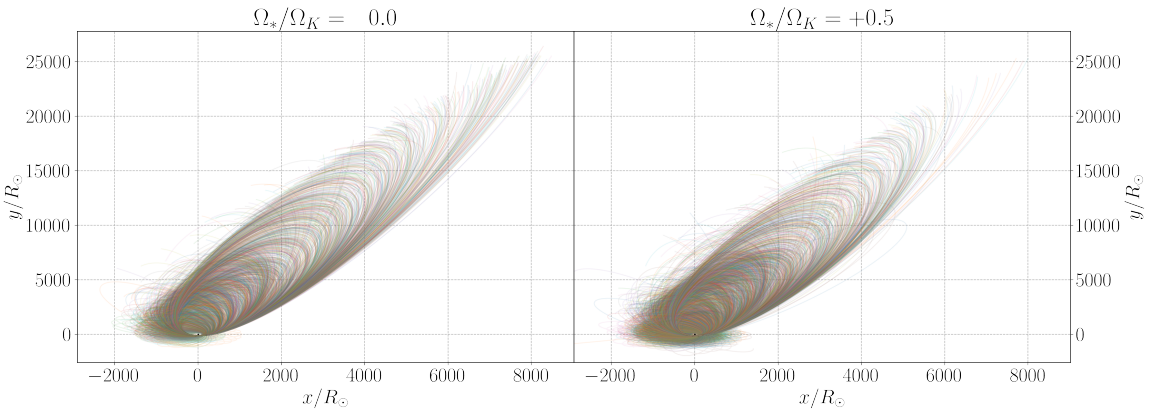

Figure 5.5: Schwarzchild geodesics of particles extracted from tidal debris. The left panel shows geodesics for an initially non-spinning star, while the right panel shows those for a star with $\Omega_*/\Omega_K = +0.5$.

elements that return to the BH have a larger velocity spread and therefore a higher collision rate. Qualitatively, this should lead to a faster rate of dissipation and circularization.

Note that this effect is not present for retrograde stellar rotation, as can be seen in Figure 5.4c. In this case, the rotational motion acts to distort the energy-momentum distribution so that more tightly bound material has a higher orbital angular momentum. This leads to a more compact distribution in e and ℓ, and consequently a smaller spread in velocity for the material that returns to the BH. In this case the specific orbital energy is $e/\Delta e_N \in (-0.3, 0.3)$ and ℓ deviates from ℓ_0 by less than 0.6%. As a result, in this section I will only consider non-spinning stars and those with prograde rotation.

In an effort to quantify this effect on circularization, I start by evolving the full GRHD simulations until well after the star completes pericenter passage, when it travels back out to a distance of $1.5\, r_t$. At this point, I extract discrete particles from each of the fluid cells to be evolved ballistically until they return to the BH and undergo their second pericenter passage after a time $t \approx 10^6\, m_h \approx 60$ days.

I perform the ballistic (geodesic) evolution on a Schwarzchild background in units with $m_h = 1$:

$$ds^2 = -\left(1 - 2/r\right)\, dt^2 + \left(1 - 2/r\right)^{-1}\, dr^2 + r^2\left(d\theta^2 + \sin^2\theta\, d\phi^2\right). \tag{5.6}$$

The radial coordinate r is related to the isotropic simulation coordinates as $r = (2r_i + 1)^2 / 4r_i$. The geodesics are governed by a first order system of differential equations for r, θ, ϕ, and the four components of the four velocity $u^\mu = \frac{dx^\mu}{d\tau}$:

$$\dot{r} = u^r / u^t \tag{5.7}$$

$$\dot{\theta} = u^\theta / u^t \tag{5.8}$$

$$\dot{\phi} = u^\phi / u^t \tag{5.9}$$

$$\dot{u}^t = -2\Gamma^t_{tr} u^r \tag{5.10}$$

$$\dot{u}^r = -\left(\Gamma^r_{tt}(u^t)^2 + \Gamma^r_{rr}(u^r)^2 + \Gamma^r_{\theta\theta}(u^\theta)^2 + \Gamma^r_{\phi\phi}(u^\phi)^2\right) / u^t \tag{5.11}$$

$$\dot{u}^\theta = -\left(2\Gamma^\theta_{r\theta} u^r u^\theta + \Gamma^\theta_{\phi\phi}(u^\phi)^2\right) / u^t \tag{5.12}$$

$$\dot{u}^\phi = -2u^\phi \left(\Gamma^\phi_{r\phi} u^r + \Gamma^\phi_{\theta\phi} u^\theta\right) / u^t \tag{5.13}$$

Here dots indicate time derivatives, and $\Gamma^\sigma_{\mu\nu}$ are the Christoffel symbols for the Schwarzchild metric in Equation 5.6. Some of the geodesics resulting from this evolution process can be seen in Figure 5.5.

With the geodesics for each extracted particle in hand, I then decompose the domain into uniform bins of width Δx. Each of these bins contains a list of velocity vectors $\vec{v}_i$. Whenever a geodesic trajectory crosses one of the bins, I append the velocity of the trajectory during the crossing to the bin. Once I have processed all of the particles in this way, I look at each bin individually and consider each pair of velocities v_i and v_j as a colliding debris stream and calculate the energy lost for each collision.

In order to calculate these collisional energy losses, I use a similar approach to Bonnerot, Rossi, and Lodato [144] and assume that collisions are completely inelastic. I depart from this previous approach by dropping the assumption that the colliding streams have nearly the same speed. While this assumption was appropriate in the original work, the same does not hold true in this context. If the two incoming streams have velocities $\vec{v}_1$ and $\vec{v}_2$, then the

specific energy lost in the collision is given by

$$\Delta e_{ss} = \frac{1}{8}\left(\vec{v}_1 - \vec{v}_2\right)^2 = \frac{1}{8}\left(v_1^2 + v_2^2\right) - \frac{1}{4} v_1 v_2 \cos\Psi_{12}, \tag{5.14}$$

where Ψ_{12} is the angle between $\vec{v}_1$ and $\vec{v}_2$.

As it is defined in Equation 5.14, the numerical value of Δe_{ss} is effectively meaningless. For one, the number of particles that crosses each bin n_p is highly sensitive to both the bin resolution Δx and the original resolution of the GRHD simulation from which the particles were extracted. Furthermore, the particle energy for each geodesic is *not* updated to reflect collisional losses. As a result, any measure of total energy loss derived from Δe_{ss} is meaningless. More importantly, the value of Δe_{ss} does not take into account any temporal information about the particle geodesics. This means that not all of the velocity pairs used in Equation 5.14 represent true collisions. Rather, bins with large values of Δe_{ss} just indicate locations in space that are crossed by debris streams with varying orientations.

To derive meaning from Δe_{ss}, I instead look at the average energy loss *per collision* $\Delta e_{ss}/n_c$, where the number of collisions is given by the number of unique velocity pairs $\vec{v}_i$ and $\vec{v}_j$ $(i, j < n_p)$

$$n_c = \frac{n_p!}{2\,(n_p - 2)\,!}. \tag{5.15}$$

In this way, I avoid ambiguity as to whether or not a collision actually occurs in a bin. Instead, bins with large values of $\Delta e_{ss}/n_c$ show locations in space with high potential for collisional energy loss.

In Figure 5.6 I show the average energy lost per collision for an initially non-spinning star (left) and one with prograde stellar rotation (right). For the non-spinning star, the outline of the resulting accretion disk can be easily seen as the elliptical void centered on the origin with a semi-major axis of $\approx 200\,R_\odot$. In this case, there are two primary regions with large energy losses: at the edge of the accretion disk and along the left edge of the returning debris stream (as seen in Figure 5.5). This is exactly what you would expect if the collisional losses

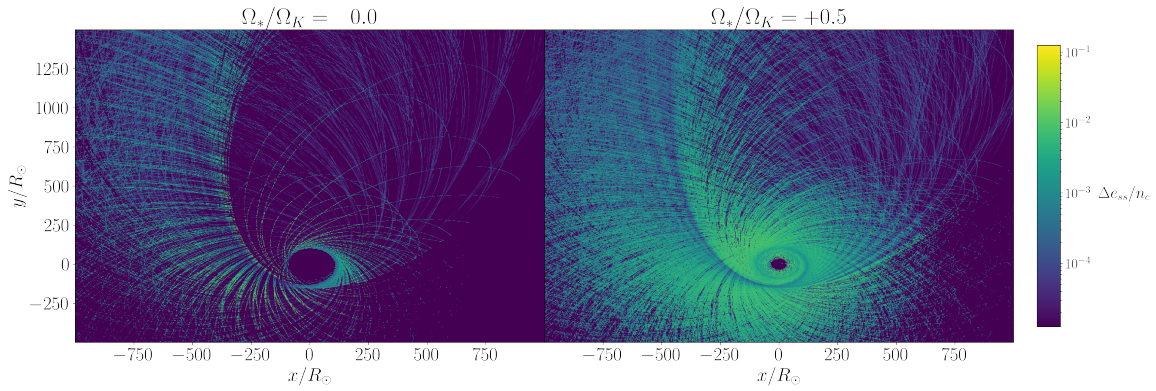

Figure 5.6: Average specific energy loss per collision $\Delta e_{ss}/n_c$ of returning tidal debris. The leftmost panel shows an initially non-spinning star, while the rightmost shows a star with $\Omega_*/\Omega_K = +0.5$.

are largely driven by relativistic precession. The losses near the edge of the disk are caused by the precession of the material in the disk, while those along the returning debris stream are caused by precession of the less tightly bound material.

For the star with prograde rotation, even larger average energy losses can be seen in the same regions as in the non-spinning case. This is also to be expected since, based on the energy-momentum distributions in Figure 5.4, the prograde spinning star has material that is more tightly bound than the non-spinning star, which would undergo more pronounced relativistic precession.

The rotating case departs from the non-spinning most significantly within the returning debris streams. For the non-spinning star in the left panel of Figure 5.6, there is a prominent void in the average energy loss within the streams, which is to be expected if nearby debris streams are primarily traveling in the same direction. For the prograde spinning star, the debris has a larger spread in orbital angular momentum which results in a larger range in the direction of motion for nearby streams and more pronounced collisional energy losses.

5.3 Future work

While the analysis presented in the previous section provides strong indications that stellar rotation may play a significant role in tidal debris circularization, it leaves much to be

desired when it comes to quantitative predictions. The primary source of this deficit is my approximation of the trajectories of the extracted particles as geodesics. This is appropriate before the particles approach the second pericenter passage, since the debris streams are diffuse far from the BH. However, as the debris approaches the BH and is focused into the nozzle, hydrodynamical forces within the fluid are fundamental to understanding the circularization process. Instead of calculating ballistic trajectories, future work should evolve the tidal debris using SPH methods in order to fully quantify the effects of stellar rotation on collisional energy losses.

REFERENCES

[1] J. Aasi *et al.*, "Advanced LIGO," *Class. Quant. Grav.*, vol. 32, p. 074 001, 2015. arXiv: 1411.4547 [gr-qc].

[2] F. Acernese *et al.*, "Advanced Virgo: a second-generation interferometric gravitational wave detector," *Class. Quant. Grav.*, vol. 32, no. 2, p. 024 001, 2015. arXiv: 1408.3978 [gr-qc].

[3] B. Abbott *et al.*, "GWTC-1: A gravitational-wave transient catalog of compact binary mergers observed by LIGO and virgo during the first and second observing runs," *Physical Review X*, vol. 9, no. 3, Sep. 2019.

[4] LIGO Scientific Collaboration and Virgo Collaboration, R. Abbott, T. D. Abbott, *et al.*, "GWTC-2: Compact Binary Coalescences Observed by LIGO and Virgo during the First Half of the Third Observing Run," *Phys. Rev. X*, vol. 11, no. 2, p. 021 053, Jun. 2021.

[5] B. P. Abbott *et al.*, "Observation of Gravitational Waves from a Binary Black Hole Merger," *Phys. Rev. Lett.*, vol. 116, no. 6, p. 061 102, 2016. arXiv: 1602.03837 [gr-qc].

[6] R. Abbott *et al.*, "GW190412: Observation of a Binary-Black-Hole Coalescence with Asymmetric Masses," Apr. 2020. arXiv: 2004.08342 [astro-ph.HE].

[7] B. P. Abbott *et al.*, "GW170817: Observation of Gravitational Waves from a Binary Neutron Star Inspiral," *Phys. Rev. Lett.*, vol. 119, no. 16, p. 161 101, 2017. arXiv: 1710.05832 [gr-qc].

[8] B. P. Abbott, R. Abbott, T. D. Abbott, S. Abraham, F. Acernese, K. Ackley, C. Adams, R. X. Adhikari, V. B. Adya, C. Affeldt, and et al., "Gw190425: Observation of a compact binary coalescence with total mass $\sim 3.4 M_{\odot}$," *The Astrophysical Journal*, vol. 892, no. 1, p. L3, Mar. 2020.

[9] R. Abbott, T. D. Abbott, S. Abraham, *et al.*, "GW190814: Gravitational Waves from the Coalescence of a 23 Solar Mass Black Hole with a 2.6 Solar Mass Compact Object," *ApJL*, vol. 896, no. 2, p. L44, Jun. 2020.

[10] R. Abbott, T. D. Abbott, S. Abraham, *et al.*, "Observation of Gravitational Waves from Two Neutron Star–Black Hole Coalescences," *ApJL*, vol. 915, no. 1, p. L5, Jun. 2021.

[11] P. Amaro-Seoane, H. Audley, S. Babak, J. Baker, E. Barausse, P. Bender, E. Berti, P. Binetruy, M. Born, D. Bortoluzzi, J. Camp, C. Caprini, V. Cardoso, M. Colpi,

J. Conklin, N. Cornish, C. Cutler, K. Danzmann, R. Dolesi, L. Ferraioli, V. Ferroni, E. Fitzsimons, J. Gair, L. G. Bote, D. Giardini, F. Gibert, C. Grimani, H. Halloin, G. Heinzel, T. Hertog, M. Hewitson, K. Holley-Bockelmann, D. Hollington, M. Hueller, H. Inchauspe, P. Jetzer, N. Karnesis, C. Killow, A. Klein, B. Klipstein, N. Korsakova, S. L. Larson, J. Livas, I. Lloro, N. Man, D. Mance, J. Martino, I. Mateos, K. McKenzie, S. T. McWilliams, C. Miller, G. Mueller, G. Nardini, G. Nelemans, M. Nofrarias, A. Petiteau, P. Pivato, E. Plagnol, E. Porter, J. Reiche, D. Robertson, N. Robertson, E. Rossi, G. Russano, B. Schutz, A. Sesana, D. Shoemaker, J. Slutsky, C. F. Sopuerta, T. Sumner, N. Tamanini, I. Thorpe, M. Troebs, M. Vallisneri, A. Vecchio, D. Vetrugno, S. Vitale, M. Volonteri, G. Wanner, H. Ward, P. Wass, W. Weber, J. Ziemer, and P. Zweifel, "Laser Interferometer Space Antenna," *arXiv:1702.00786 [astro-ph]*, Feb. 2017. arXiv: 1702.00786 [astro-ph].

[12] M. Punturo, M. Abernathy, F. Acernese, B. Allen, N. Andersson, K. Arun, F. Barone, B. Barr, M. Barsuglia, M. Beker, N. Beveridge, S. Birindelli, S. Bose, L. Bosi, S. Braccini, C. Bradaschia, T. Bulik, E. Calloni, G. Cella, E. C. Mottin, S. Chelkowski, A. Chincarini, J. Clark, E. Coccia, C. Colacino, J. Colas, A. Cumming, L. Cunningham, E. Cuoco, S. Danilishin, K. Danzmann, G. D. Luca, R. D. Salvo, T. Dent, R. D. Rosa, L. D. Fiore, A. D. Virgilio, M. Doets, V. Fafone, P. Falferi, R. Flaminio, J. Franc, F. Frasconi, A. Freise, P. Fulda, J. Gair, G. Gemme, A. Gennai, A. Giazotto, K. Glampedakis, M. Granata, H. Grote, G. Guidi, G. Hammond, M. Hannam, J. Harms, D. Heinert, M. Hendry, I. Heng, E. Hennes, S. Hild, J. Hough, S. Husa, S. Huttner, G. Jones, F. Khalili, K. Kokeyama, K. Kokkotas, B. Krishnan, M. Lorenzini, H. Lück, E. Majorana, I. Mandel, V. Mandic, I. Martin, C. Michel, Y. Minenkov, N. Morgado, S. Mosca, B. Mours, H. Müller–Ebhardt, P. Murray, R. Nawrodt, J. Nelson, R. Oshaughnessy, C. D. Ott, C. Palomba, A. Paoli, G. Parguez, A. Pasqualetti, R. Passaquieti, D. Passuello, L. Pinard, R. Poggiani, P. Popolizio, M. Prato, P. Puppo, D. Rabeling, P. Rapagnani, J. Read, T. Regimbau, H. Rehbein, S. Reid, L. Rezzolla, F. Ricci, F. Richard, A. Rocchi, S. Rowan, A. Rüdiger, B. Sassolas, B. Sathyaprakash, R. Schnabel, C. Schwarz, P. Seidel, A. Sintes, K. Somiya, F. Speirits, K. Strain, S. Strigin, P. Sutton, S. Tarabrin, A. Thüring, J. van den Brand, C. van Leewen, M. van Veggel, C. van den Broeck, A. Vecchio, J. Veitch, F. Vetrano, A. Vicere, S. Vyatchanin, B. Willke, G. Woan, P. Wolfango, and K. Yamamoto, "The Einstein Telescope: A third-generation gravitational wave observatory," *Class. Quantum Grav.*, vol. 27, no. 19, p. 194 002, Sep. 2010.

[13] B. P. Abbott, R. Abbott, T. D. Abbott, M. R. Abernathy, K. Ackley, C. Adams, P. Addesso, R. X. Adhikari, V. B. Adya, C. Affeldt, N. Aggarwal, O. D. Aguiar, A. Ain, P. Ajith, B. Allen, P. A. Altin, S. B. Anderson, W. G. Anderson, K. Arai, M. C. Araya, C. C. Arceneaux, J. S. Areeda, K. G. Arun, G. Ashton, M. Ast, S. M. Aston, P. Aufmuth, C. Aulbert, S. Babak, P. T. Baker, S. W. Ballmer, J. C. Barayoga, S. E. Barclay, B. C. Barish, D. Barker, B. Barr, L. Barsotti, J. Bartlett, I. Bartos, R. Bassiri, J. C. Batch, C. Baune, A. S. Bell, B. K. Berger, G. Bergmann, C. P. L. Berry, J. Betzwieser, S. Bhagwat, R. Bhandare, I. A. Bilenko, G. Billingsley, J. Birch, R. Birney, S. Biscans, A. Bisht, C. Biwer, J. K. Blackburn, C. D. Blair,

D. G. Blair, R. M. Blair, O. Bock, C. Bogan, A. Bohe, C. Bond, R. Bork, S. Bose, P. R. Brady, V. B. Braginsky, J. E. Brau, M. Brinkmann, P. Brockill, J. E. Broida, A. F. Brooks, D. A. Brown, D. D. Brown, N. M. Brown, S. Brunett, C. C. Buchanan, A. Buikema, A. Buonanno, R. L. Byer, M. Cabero, L. Cadonati, C. Cahillane, J. C. Bustillo, T. Callister, J. B. Camp, K. C. Cannon, J. Cao, C. D. Capano, S. Caride, S. Caudill, M. Cavagli'a, C. B. Cepeda, S. J. Chamberlin, M. Chan, S. Chao, P. Charlton, B. D. Cheeseboro, H. Y. Chen, Y. Chen, C. Cheng, H. S. Cho, M. Cho, J. H. Chow, N. Christensen, Q. Chu, S. Chung, G. Ciani, F. Clara, J. A. Clark, C. G. Collette, L. Cominsky, M. Constancio Jr., D. Cook, T. R. Corbitt, N. Cornish, A. Corsi, C. A. Costa, M. W. Coughlin, S. B. Coughlin, S. T. Countryman, P. Couvares, E. E. Cowan, D. M. Coward, M. J. Cowart, D. C. Coyne, R. Coyne, K. Craig, J. D. E. Creighton, J. Cripe, S. G. Crowder, A. Cumming, L. Cunningham, T. D. Canton, S. L. Danilishin, K. Danzmann, N. S. Darman, A. Dasgupta, C. F. D. S. Costa, I. Dave, G. S. Davies, E. J. Daw, S. De, D. DeBra, W. Del Pozzo, T. Denker, T. Dent, V. Dergachev, R. T. DeRosa, R. DeSalvo, R. C. Devine, S. Dhurandhar, M. C. D'iaz, I. Di Palma, F. Donovan, K. L. Dooley, S. Doravari, R. Douglas, T. P. Downes, M. Drago, R. W. P. Drever, J. C. Driggers, S. E. Dwyer, T. B. Edo, M. C. Edwards, A. Effler, H.-B. Eggenstein, P. Ehrens, J. Eichholz, S. S. Eikenberry, W. Engels, R. C. Essick, T. Etzel, M. Evans, T. M. Evans, R. Everett, M. Factourovich, H. Fair, S. Fairhurst, X. Fan, Q. Fang, B. Farr, W. M. Farr, M. Favata, M. Fays, H. Fehrmann, M. M. Fejer, E. Fenyvesi, E. C. Ferreira, R. P. Fisher, M. Fletcher, Z. Frei, A. Freise, R. Frey, P. Fritschel, V. V. Frolov, P. Fulda, M. Fyffe, H. A. G. Gabbard, J. R. Gair, S. G. Gaonkar, G. Gaur, N. Gehrels, P. Geng, J. George, L. Gergely, A. Ghosh, A. Ghosh, J. A. Giaime, K. D. Giardina, K. Gill, A. Glaefke, E. Goetz, R. Goetz, L. Gondan, G. Gonz'alez, A. Gopakumar, N. A. Gordon, M. L. Gorodetsky, S. E. Gossan, C. Graef, P. B. Graff, A. Grant, S. Gras, C. Gray, A. C. Green, H. Grote, S. Grunewald, X. Guo, A. Gupta, M. K. Gupta, K. E. Gushwa, E. K. Gustafson, R. Gustafson, J. J. Hacker, B. R. Hall, E. D. Hall, G. Hammond, M. Haney, M. M. Hanke, J. Hanks, C. Hanna, M. D. Hannam, J. Hanson, T. Hardwick, G. M. Harry, I. W. Harry, M. J. Hart, M. T. Hartman, C.-J. Haster, K. Haughian, M. C. Heintze, M. Hendry, I. S. Heng, J. Hennig, J. Henry, A. W. Heptonstall, M. Heurs, S. Hild, D. Hoak, K. Holt, D. E. Holz, P. Hopkins, J. Hough, E. A. Houston, E. J. Howell, Y. M. Hu, S. Huang, E. A. Huerta, B. Hughey, S. Husa, S. H. Huttner, T. Huynh-Dinh, N. Indik, D. R. Ingram, R. Inta, H. N. Isa, M. Isi, T. Isogai, B. R. Iyer, K. Izumi, H. Jang, K. Jani, S. Jawahar, L. Jian, F. Jim'enez-Forteza, W. W. Johnson, D. I. Jones, R. Jones, L. Ju, H. K, C. V. Kalaghatgi, V. Kalogera, S. Kandhasamy, G. Kang, J. B. Kanner, S. J. Kapadia, S. Karki, K. S. Karvinen, M. Kasprzack, E. Katsavounidis, W. Katzman, S. Kaufer, T. Kaur, K. Kawabe, M. S. Kehl, D. Keitel, D. B. Kelley, W. Kells, R. Kennedy, J. S. Key, F. Y. Khalili, S. Khan, Z. Khan, E. A. Khazanov, N. Kijbunchoo, C.-W. Kim, C. Kim, J. Kim, K. Kim, N. Kim, W. Kim, Y.-M. Kim, S. J. Kimbrell, E. J. King, P. J. King, J. S. Kissel, B. Klein, L. Kleybolte, S. Klimenko, S. M. Koehlenbeck, V. Kondrashov, A. Kontos, M. Korobko, W. Z. Korth, D. B. Kozak, V. Kringel, C. Krueger, G. Kuehn, P. Kumar, R. Kumar, L. Kuo, B. D. Lackey, M. Landry, J. Lange, B. Lantz, P. D. Lasky, M. Laxen, A. Lazzarini, S. Leavey, E. O. Lebigot, C. H. Lee, H. K. Lee, H. M. Lee,

K. Lee, A. Lenon, J. R. Leong, Y. Levin, J. B. Lewis, T. G. F. Li, A. Libson, T. B. Littenberg, N. A. Lockerbie, A. L. Lombardi, L. T. London, J. E. Lord, M. Lormand, J. D. Lough, H. L"uck, A. P. Lundgren, R. Lynch, Y. Ma, B. Machenschalk, M. MacInnis, D. M. Macleod, F. Magaña-Sandoval, L. M. Zertuche, R. M. Magee, V. Mandic, V. Mangano, G. L. Mansell, M. Manske, S. M'arka, Z. M'arka, A. S. Markosyan, E. Maros, I. W. Martin, D. V. Martynov, K. Mason, T. J. Massinger, M. Masso-Reid, F. Matichard, L. Matone, N. Mavalvala, N. Mazumder, R. McCarthy, D. E. McClelland, S. McCormick, S. C. McGuire, G. McIntyre, J. McIver, D. J. McManus, T. McRae, S. T. McWilliams, D. Meacher, G. D. Meadors, A. Melatos, G. Mendell, R. A. Mercer, E. L. Merilh, S. Meshkov, C. Messenger, C. Messick, P. M. Meyers, H. Miao, H. Middleton, E. E. Mikhailov, A. L. Miller, A. Miller, B. B. Miller, J. Miller, M. Millhouse, J. Ming, S. Mirshekari, C. Mishra, S. Mitra, V. P. Mitrofanov, G. Mitselmakher, R. Mittleman, S. R. P. Mohapatra, B. C. Moore, C. J. Moore, D. Moraru, G. Moreno, S. R. Morriss, K. Mossavi, C. M. Mow-Lowry, G. Mueller, A. W. Muir, A. Mukherjee, D. Mukherjee, S. Mukherjee, N. Mukund, A. Mullavey, J. Munch, D. J. Murphy, P. G. Murray, A. Mytidis, R. K. Nayak, K. Nedkova, T. J. N. Nelson, A. Neunzert, G. Newton, T. T. Nguyen, A. B. Nielsen, A. Nitz, D. Nolting, M. E. N. Normandin, L. K. Nuttall, J. Oberling, E. Ochsner, J. O'Dell, E. Oelker, G. H. Ogin, J. J. Oh, S. H. Oh, F. Ohme, M. Oliver, P. Oppermann, R. J. Oram, B. O'Reilly, R. O'Shaughnessy, D. J. Ottaway, H. Overmier, B. J. Owen, A. Pai, S. A. Pai, J. R. Palamos, O. Palashov, A. Pal-Singh, H. Pan, C. Pankow, F. Pannarale, B. C. Pant, M. A. Papa, H. R. Paris, W. Parker, D. Pascucci, Z. Patrick, B. L. Pearlstone, M. Pedraza, L. Pekowsky, A. Pele, S. Penn, A. Perreca, L. M. Perri, M. Phelps, V. Pierro, I. M. Pinto, M. Pitkin, M. Poe, A. Post, J. Powell, J. Prasad, J. Pratt, V. Predoi, T. Prestegard, L. R. Price, M. Prijatelj, M. Principe, S. Privitera, L. Prokhorov, O. Puncken, M. P"urrer, H. Qi, J. Qin, S. Qiu, V. Quetschke, E. A. Quintero, R. Quitzow-James, F. J. Raab, D. S. Rabeling, H. Radkins, P. Raffai, S. Raja, C. Rajan, M. Rakhmanov, V. Raymond, J. Read, C. M. Reed, S. Reid, D. H. Reitze, H. Rew, S. D. Reyes, K. Riles, M. Rizzo, N. A. Robertson, R. Robie, J. G. Rollins, V. J. Roma, G. Romanov, J. H. Romie, S. Rowan, A. R"udiger, K. Ryan, S. Sachdev, T. Sadecki, L. Sadeghian, M. Sakellariadou, M. Saleem, F. Salemi, A. Samajdar, L. Sammut, E. J. Sanchez, V. Sandberg, B. Sandeen, J. R. Sanders, B. S. Sathyaprakash, P. R. Saulson, O. E. S. Sauter, R. L. Savage, A. Sawadsky, P. Schale, R. Schilling, J. Schmidt, P. Schmidt, R. Schnabel, R. M. S. Schofield, A. Sch"onbeck, E. Schreiber, D. Schuette, B. F. Schutz, J. Scott, S. M. Scott, D. Sellers, A. S. Sengupta, A. Sergeev, D. A. Shaddock, T. Shaffer, M. S. Shahriar, M. Shaltev, B. Shapiro, P. Shawhan, A. Sheperd, D. H. Shoemaker, D. M. Shoemaker, K. Siellez, X. Siemens, D. Sigg, A. D. Silva, A. Singer, L. P. Singer, A. Singh, R. Singh, A. M. Sintes, B. J. J. Slagmolen, J. R. Smith, N. D. Smith, R. J. E. Smith, E. J. Son, B. Sorazu, T. Souradeep, A. K. Srivastava, A. Staley, M. Steinke, J. Steinlechner, S. Steinlechner, D. Steinmeyer, B. C. Stephens, R. Stone, K. A. Strain, N. A. Strauss, S. Strigin, R. Sturani, A. L. Stuver, T. Z. Summerscales, L. Sun, S. Sunil, P. J. Sutton, M. J. Szczepa'nczyk, D. Talukder, D. B. Tanner, M. T'apai, S. P. Tarabrin, A. Taracchini, R. Taylor, T. Theeg, M. P. Thirugnanasambandam, E. G. Thomas, M. Thomas, P. Thomas, K. A. Thorne, E. Thrane, V. Tiwari, K. V. Tokmakov, K.

Toland, C. Tomlinson, Z. Tornasi, C. V. Torres, C. I. Torrie, D. T"oyr"a, G. Traylor, D. Trifir'o, M. Tse, D. Tuyenbayev, D. Ugolini, C. S. Unnikrishnan, A. L. Urban, S. A. Usman, H. Vahlbruch, G. Vajente, G. Valdes, D. C. Vander-Hyde, A. A. van Veggel, S. Vass, R. Vaulin, A. Vecchio, J. Veitch, P. J. Veitch, K. Venkateswara, S. Vinciguerra, D. J. Vine, S. Vitale, T. Vo, C. Vorvick, D. V. Voss, W. D. Vousden, S. P. Vyatchanin, A. R. Wade, L. E. Wade, M. Wade, M. Walker, L. Wallace, S. Walsh, H. Wang, M. Wang, X. Wang, Y. Wang, R. L. Ward, J. Warner, B. Weaver, M. Weinert, A. J. Weinstein, R. Weiss, L. Wen, P. Wessels, T. Westphal, K. Wette, J. T. Whelan, B. F. Whiting, R. D. Williams, A. R. Williamson, J. L. Willis, B. Willke, M. H. Wimmer, W. Winkler, C. C. Wipf, H. Wittel, G. Woan, J. Woehler, J. Worden, J. L. Wright, D. S. Wu, G. Wu, J. Yablon, W. Yam, H. Yamamoto, C. C. Yancey, H. Yu, M. Zanolin, M. Zevin, L. Zhang, M. Zhang, Y. Zhang, C. Zhao, M. Zhou, Z. Zhou, X. J. Zhu, M. E. Zucker, S. E. Zuraw, J. Zweizig, and J. Harms, "Exploring the Sensitivity of Next Generation Gravitational Wave Detectors," *Class. Quantum Grav.*, vol. 34, no. 4, p. 044 001, Feb. 2017. arXiv: 1607.08697.

[14] T. W. Baumgarte and S. L. Shapiro, "Numerical integration of Einstein's field equations," *Physical Review D*, vol. 59, no. 2, p. 024 007, Dec. 1998.

[15] M. Shibata and T. Nakamura, "Evolution of three-dimensional gravitational waves: Harmonic slicing case," *Physical Review D*, vol. 52, no. 10, pp. 5428–5444, Nov. 1995.

[16] M. Campanelli, C. O. Lousto, P. Marronetti, and Y. Zlochower, "Accurate Evolutions of Orbiting Black-Hole Binaries without Excision," *Physical Review Letters*, vol. 96, no. 11, p. 111 101, Mar. 2006.

[17] L. Antón, O. Zanotti, J. A. Miralles, J. M. Martí, J. M. Ibáñez, J. A. Font, and J. A. Pons, "Numerical 3+1 General Relativistic Magnetohydrodynamics: A Local Characteristic Approach," *The Astrophysical Journal*, vol. 637, no. 1, p. 296, Jan. 2006.

[18] T. Goodale, G. Allen, G. Lanfermann, J. Masso, T. Radke, E. Seidel, and J. Shalf, "The Cactus Framework and Toolkit: Design and Applications," in *VECPAVector and Parallel Processing R'2002, 5th International Conference*, Berlin: Springer, 2003.

[19] S. Husa, I. Hinder, and C. Lechner, "Kranc: A Mathematica package to generate numerical codes for tensorial evolution equations," *Computer Physics Communications*, vol. 174, no. 12, pp. 983–1004, Jun. 2006.

[20] R. Haas, R. V. Shcherbakov, T. Bode, and P. Laguna, "Tidal Disruptions of White Dwarfs from Ultra-close Encounters with Intermediate-mass Spinning Black Holes," *The Astrophysical Journal*, vol. 749, no. 2, p. 117, 2012.

[21] C. Evans, P. Laguna, and M. Eracleous, "Ultra-close Encounters of Stars with Massive Black Holes: Tidal Disruption Events with Prompt Hyperaccretion," *The Astrophysical Journal Letters*, vol. 805, no. 2, p. L19, 2015.

[22] M. Clark and P. Laguna, "Bowen-York-type initial data for binaries with neutron stars," *Physical Review D*, vol. 94, no. 6, p. 064 058, Sep. 2016.

[23] K. Jani, J. Healy, J. A. Clark, L. London, P. Laguna, and D. Shoemaker, "Georgia tech catalog of gravitational waveforms," *Classical and Quantum Gravity*, vol. 33, no. 20, p. 204 001, 2016.

[24] M. Babiuc-Hamilton, S. R. Brandt, P. Diener, M. Elley, Z. Etienne, G. Ficarra, R. Haas, H. Witek, M. Alcubierre, D. Alic, G. Allen, M. Ansorg, L. Baiotti, W. Benger, E. Bentivegna, S. Bernuzzi, T. Bode, B. Bruegmann, G. Corvino, R. De Pietri, H. Dimmelmeier, R. Dooley, N. Dorband, Y. El Khamra, J. Faber, T. Font, J. Frieben, B. Giacomazzo, T. Goodale, C. Gundlach, I. Hawke, S. Hawley, I. Hinder, S. Husa, S. Iyer, T. Kellermann, A. Knapp, M. Koppitz, G. Lanferman, F. Löffler, J. Masso, L. Menger, A. Merzky, M. Miller, P. Moesta, P. Montero, B. Mundim, A. Nerozzi, C. Ott, R. Paruchuri, D. Pollney, D. Radice, T. Radke, C. Reisswig, L. Rezzolla, D. Rideout, M. Ripeanu, E. Schnetter, B. Schutz, E. Seidel, E. Seidel, J. Shalf, U. Sperhake, N. Stergioulas, W.-M. Suen, B. Szilagyi, R. Takahashi, M. Thomas, J. Thornburg, M. Tobias, A. Tonita, P. Walker, M.-B. Wan, B. Wardell, M. Zilhão, B. Zink, and Y. Zlochower, *The einstein toolkit*, version The "Mayer" release, ET_2019_10, To find out more, visit http://einsteintoolkit.org, Oct. 2019.

[25] E. Schnetter, S. H. Hawley, and I. Hawke, "Evolutions in 3D numerical relativity using fixed mesh refinement," *Classical and Quantum Gravity*, vol. 21, no. 6, p. 1465, 2004.

[26] E. Schnetter, P. Diener, E. N. Dorband, and M. Tiglio, "A multi-block infrastructure for three-dimensional time-dependent numerical relativity," *Classical and Quantum Gravity*, vol. 23, no. 16, S553, 2006.

[27] J. G. Baker, J. Centrella, D.-I. Choi, M. Koppitz, and J. van Meter, "Gravitational-Wave Extraction from an Inspiraling Configuration of Merging Black Holes," *Physical Review Letters*, vol. 96, no. 11, p. 111 102, Mar. 2006.

[28] Z. B. Etienne, V. Paschalidis, R. Haas, P. Mösta, and S. L. Shapiro, "IllinoisGRMHD: An open-source, user-friendly GRMHD code for dynamical spacetimes," *Classical and Quantum Gravity*, vol. 32, no. 17, p. 175 009, Aug. 2015.

[29] S. Husa, M. Hannam, J. A. González, U. Sperhake, and B. Brügmann, "Reducing eccentricity in black-hole binary evolutions with initial parameters from post-Newtonian inspiral," *Physical Review D*, vol. 77, no. 4, p. 044 037, Feb. 2008.

[30] W. Tichy and P. Marronetti, "Simple method to set up low eccentricity initial data for moving puncture simulations," *Physical Review D*, vol. 83, no. 2, p. 024 012, Jan. 2011.

[31] M. Ansorg, B. Brügmann, and W. Tichy, "Single-domain spectral method for black hole puncture data," *Physical Review D*, vol. 70, no. 6, p. 064 011, Sep. 2004.

[32] J. M. Bowen and J. W. York, "Time-asymmetric initial data for black holes and black-hole collisions," *Physical Review D*, vol. 21, no. 8, pp. 2047–2056, Apr. 1980.

[33] J. Thornburg, "A fast apparent horizon finder for three-dimensional Cartesian grids in numerical relativity," *Classical and Quantum Gravity*, vol. 21, no. 2, p. 743, 2004.

[34] C. Reisswig, N. T. Bishop, D. Pollney, and B. Szilágyi, "Characteristic extraction in numerical relativity: Binary black hole merger waveforms at null infinity," *Classical and Quantum Gravity*, vol. 27, no. 7, p. 075 014, Mar. 2010.

[35] B. P. Abbott *et al.*, "Binary Black Hole Population Properties Inferred from the First and Second Observing Runs of Advanced LIGO and Advanced Virgo," 2018. arXiv: 1811.12940 [astro-ph.HE].

[36] ——, "Astrophysical Implications of the Binary Black-Hole Merger GW150914," *Astrophys. J.*, vol. 818, no. 2, p. L22, 2016. arXiv: 1602.03846 [astro-ph.HE].

[37] S. Stevenson, A. Vigna-Gómez, I. Mandel, J. W. Barrett, C. J. Neijssel, D. Perkins, and S. E. de Mink, "Formation of the first three gravitational-wave observations through isolated binary evolution," 2017, [Nature Commun.8,14906(2017)]. arXiv: 1704.01352 [astro-ph.HE].

[38] A. Einstein, "The Foundation of the General Theory of Relativity," *Annalen Phys.*, vol. 49, no. 7, pp. 769–822, 1916, [Annalen Phys.14,517(2005)].

[39] C. W. Misner, K. Thorne, and J. Wheeler, "Gravitation," 1974.

[40] B. P. Abbott *et al.*, "Tests of General Relativity with the Binary Black Hole Signals from the LIGO-Virgo Catalog GWTC-1," 2019. arXiv: 1903.04467 [gr-qc].

[41] ——, "Tests of general relativity with GW150914," *Phys. Rev. Lett.*, vol. 116, no. 22, p. 221 101, 2016. arXiv: 1602.03841 [gr-qc].

[42] B. P. Abbott, R. Abbott, T. D. Abbott, M. R. Abernathy, F. Acernese, K. Ackley, C. Adams, T. Adams, P. Addesso, R. X. Adhikari, V. B. Adya, C. Affeldt, M. Agathos, K. Agatsuma, N. Aggarwal, O. D. Aguiar, L. Aiello, A. Ain, P. Ajith, B. Allen, A. Allocca, P. A. Altin, S. B. Anderson, W. G. Anderson, K. Arai, M. C. Araya, C. C. Arceneaux, J. S. Areeda, N. Arnaud, K. G. Arun, S. Ascenzi, G. Ashton,

M. Ast, S. M. Aston, P. Astone, P. Aufmuth, C. Aulbert, S. Babak, P. Bacon, and M. K. M. Bader, "Binary black hole mergers in the first advanced ligo observing run," *Phys. Rev. X*, vol. 6, p. 041 015, 4 Oct. 2016.

[43] M. Maggiore, *Gravitational Waves. Vol. 1: Theory and experiments*. Oxford University Press, 2007.

[44] F. Pretorius, "Evolution of binary black hole spacetimes," *Phys.Rev.Lett.*, vol. 95, p. 121 101, 2005. arXiv: gr-qc/0507014 [gr-qc].

[45] E. Berti, V. Cardoso, and A. O. Starinets, "Quasinormal modes of black holes and black branes," *Class. Quant. Grav.*, vol. 26, p. 163 001, 2009. arXiv: 0905.2975 [gr-qc].

[46] R. Owen, "The Final Remnant of Binary Black Hole Mergers: Multipolar Analysis," *Phys. Rev.*, vol. D80, p. 084 012, 2009. arXiv: 0907.0280 [gr-qc].

[47] M. Isi, M. Giesler, W. M. Farr, M. A. Scheel, and S. A. Teukolsky, "Testing the no-hair theorem with GW150914," 2019. arXiv: 1905.00869 [gr-qc].

[48] V. Cardoso, S. Hopper, C. F. B. Macedo, C. Palenzuela, and P. Pani, "Gravitational-wave signatures of exotic compact objects and of quantum corrections at the horizon scale," *Phys. Rev.*, vol. D94, no. 8, p. 084 031, 2016. arXiv: 1608.08637 [gr-qc].

[49] A. Ashtekar and B. Krishnan, "Isolated and Dynamical Horizons and Their Applications," *Living Reviews in Relativity*, vol. 7, no. 1, 10, p. 10, Dec. 2004. arXiv: gr-qc/0407042 [gr-qc].

[50] O. Dreyer, B. Krishnan, D. Shoemaker, and E. Schnetter, "Introduction to isolated horizons in numerical relativity," *Physical Review D*, vol. 67, no. 2, p. 024 018, Jan. 2003.

[51] A. Ashtekar, J. Engle, T. Pawlowski, and C. V. D. Broeck, "Multipole moments of isolated horizons," *Classical and Quantum Gravity*, vol. 21, no. 11, pp. 2549–2570, Apr. 2004.

[52] A. Ashtekar, M. Campiglia, and S. Shah, "Dynamical black holes: Approach to the final state," *Physical Review D*, vol. 88, no. 6, p. 064 045, Sep. 2013.

[53] A. Gupta, B. Krishnan, A. B. Nielsen, and E. Schnetter, "Dynamics of marginally trapped surfaces in a binary black hole merger: Growth and approach to equilibrium," *Physical Review D*, vol. 97, no. 8, p. 084 028, Apr. 2018.

[54] J. L. Jaramillo, R. P. Macedo, P. Moesta, and L. Rezzolla, "Black-hole horizons as probes of black-hole dynamics. II. Geometrical insights," *Physical Review D*, vol. 85, no. 8, p. 084 031, Apr. 2012.

[55] ——, "Black-hole horizons as probes of black-hole dynamics. I. Post-merger recoil in head-on collisions," *Physical Review D*, vol. 85, no. 8, p. 084 030, Apr. 2012.

[56] J. L. Jaramillo, R. P. Macedo, P. Moesta, and L. Rezzolla, "Towards a cross-correlation approach to strong-field dynamics in black hole spacetimes," *AIP Conference Proceedings*, vol. 1458, no. 1, pp. 158–173, Jul. 2012.

[57] V. Prasad, A. Gupta, S. Bose, B. Krishnan, and E. Schnetter, "News from horizons in binary black hole mergers," *arXiv e-prints*, arXiv:2003.06215, arXiv:2003.06215, Mar. 2020. arXiv: 2003.06215 [gr-qc].

[58] A. Ashtekar and B. Krishnan, "Dynamical horizons and their properties," *Physical Review D*, vol. 68, no. 10, p. 104 030, Nov. 2003.

[59] E. Schnetter, B. Krishnan, and F. Beyer, "Introduction to dynamical horizons in numerical relativity," *Physical Review D*, vol. 74, no. 2, p. 024 028, Jul. 2006.

[60] J. L. Jaramillo, M. Ansorg, and N. Vasset, "Application of initial data sequences to the study of Black Hole dynamical trapping horizons," *AIP Conference Proceedings*, vol. 1122, no. 1, pp. 308–311, May 2009.

[61] P. Mösta, L. Andersson, J. Metzger, B. Szilágyi, and J. Winicour, "The merger of small and large black holes," *Classical and Quantum Gravity*, vol. 32, no. 23, p. 235 003, 2015.

[62] D. Pook-Kolb, O. Birnholtz, B. Krishnan, and E. Schnetter, "Existence and stability of marginally trapped surfaces in black-hole spacetimes," *Physical Review D*, vol. 99, no. 6, p. 064 005, Mar. 2019.

[63] S. Brandt and B. Brügmann, "A simple construction of initial data for multiple black holes," *Phys. Rev. Lett.*, vol. 78, pp. 3606–3609, 19 May 1997.

[64] A. Ashtekar and G. J. Galloway, "Some uniqueness results for dynamical horizons," *Advances in Theoretical and Mathematical Physics*, vol. 9, no. 1, pp. 1–30, Jan. 2005.

[65] A. Ashtekar, C. Beetle, and S. Fairhurst, "Mechanics of isolated horizons," *Classical and Quantum Gravity*, vol. 17, no. 2, pp. 253–298, Dec. 1999.

[66] D. R. Brill and R. W. Lindquist, "Interaction Energy in Geometrostatics," *Physical Review*, vol. 131, no. 1, pp. 471–476, Jul. 1963.

[67] R. W. Lindquist, "Initial-Value Problem on Einstein-Rosen Manifolds," *Journal of Mathematical Physics*, vol. 4, no. 7, pp. 938–950, Jul. 1963.

[68] D. Pook-Kolb, O. Birnholtz, B. Krishnan, and E. Schnetter, "Interior of a Binary Black Hole Merger," *Physical Review Letters*, vol. 123, no. 17, p. 171 102, Oct. 2019.

[69] D. Pook-Kolb, "Self-intersecting marginally outer trapped surfaces," *Physical Review D*, vol. 100, no. 8, 2019.

[70] M. Hannam, S. Husa, D. Pollney, B. Brügmann, and N. Ó. Murchadha, "Geometry and Regularity of Moving Punctures," *Physical Review Letters*, vol. 99, no. 24, p. 241 102, Dec. 2007.

[71] B. Bruegmann, "Schwarzschild black hole as moving puncture in isotropic coordinates," *Gen. Rel. Grav.*, vol. 41, pp. 2131–2151, 2009. arXiv: 0904.4418 [gr-qc].

[72] M. Hannam, S. Husa, F. Ohme, B. Brügmann, and N. Ó Murchadha, "Wormholes and trumpets: Schwarzschild spacetime for the moving-puncture generation," *Physical Review D*, vol. 78, no. 6, p. 064 020, Sep. 2008.

[73] L. Blanchet, "Gravitational Radiation from Post-Newtonian Sources and Inspiralling Compact Binaries," *Living Rev. Rel.*, vol. 17, p. 2, 2014. arXiv: 1310.1528 [gr-qc].

[74] E. Berti, V. Cardoso, J. A. Gonzalez, U. Sperhake, M. Hannam, S. Husa, and B. Bruegmann, "Inspiral, merger and ringdown of unequal mass black hole binaries: A Multipolar analysis," *Phys. Rev. D*, vol. 76, p. 064 034, 2007. arXiv: gr-qc/0703053 [GR-QC].

[75] P. B. Graff, A. Buonanno, and B. S. Sathyaprakash, "Missing Link: Bayesian detection and measurement of intermediate-mass black-hole binaries," *Phys. Rev.*, vol. D92, no. 2, p. 022 002, 2015. arXiv: 1504.04766 [gr-qc].

[76] J. Calderón Bustillo, J. A. Clark, P. Laguna, and D. Shoemaker, "Tracking black hole kicks from gravitational wave observations," *Phys. Rev. Lett.*, vol. 121, no. 19, p. 191 102, 2018. arXiv: 1806.11160 [gr-qc].

[77] J. A. Gonzalez, U. Sperhake, and B. Bruegmann, "Black-hole binary simulations: The Mass ratio 10:1," *Phys. Rev.*, vol. D79, p. 124 006, 2009. arXiv: 0811.3952 [gr-qc].

[78] L. Rezzolla, R. P. Macedo, and J. L. Jaramillo, "Understanding the 'anti-kick' in the merger of binary black holes," *Phys. Rev. Lett.*, vol. 104, p. 221 101, 2010. arXiv: 1003.0873 [gr-qc].

[79] J. L. Jaramillo, R. Panosso Macedo, P. Moesta, and L. Rezzolla, "Black-hole horizons as probes of black-hole dynamics I: post-merger recoil in head-on collisions," *Phys. Rev.*, vol. D85, p. 084 030, 2012. arXiv: 1108.0060 [gr-qc].

[80] J. L. Jaramillo, R. P. Macedo, P. Moesta, and L. Rezzolla, "Black-hole horizons as probes of black-hole dynamics II: geometrical insights," *Phys. Rev.*, vol. D85, p. 084 031, 2012. arXiv: 1108.0061 [gr-qc].

[81] J. L. Jaramillo, R. P. Macedo, P. Moesta, and L. Rezzolla, "Towards a cross-correlation approach to strong-field dynamics in Black Hole spacetimes," *AIP Conf. Proc.*, vol. 1458, no. 1, pp. 158–173, 2012. arXiv: 1205.3902 [gr-qc].

[82] R. Owen, J. Brink, Y. Chen, J. D. Kaplan, G. Lovelace, K. D. Matthews, D. A. Nichols, M. A. Scheel, F. Zhang, A. Zimmerman, and K. S. Thorne, "Frame-dragging vortexes and tidal tendexes attached to colliding black holes: Visualizing the curvature of spacetime," *Physical Review Letters*, vol. 106, no. 15, Apr. 2011.

[83] D. A. Nichols, R. Owen, F. Zhang, A. Zimmerman, J. Brink, Y. Chen, J. D. Kaplan, G. Lovelace, K. D. Matthews, M. A. Scheel, and K. S. Thorne, "Visualizing spacetime curvature via frame-drag vortexes and tidal tendexes: General theory and weak-gravity applications," *Physical Review D*, vol. 84, no. 12, Dec. 2011.

[84] F. Zhang, A. Zimmerman, D. A. Nichols, Y. Chen, G. Lovelace, K. D. Matthews, R. Owen, and K. S. Thorne, "Visualizing spacetime curvature via frame-drag vortexes and tidal tendexes. II. stationary black holes," *Physical Review D*, vol. 86, no. 8, Oct. 2012.

[85] D. A. Nichols, A. Zimmerman, Y. Chen, G. Lovelace, K. D. Matthews, R. Owen, F. Zhang, and K. S. Thorne, "Visualizing spacetime curvature via frame-drag vortexes and tidal tendexes. III. quasinormal pulsations of schwarzschild and kerr black holes," *Physical Review D*, vol. 86, no. 10, Nov. 2012.

[86] V. Prasad, A. Gupta, S. Bose, B. Krishnan, and E. Schnetter, *News from horizons in binary black hole mergers*, 2020. eprint: arXiv:2003.06215.

[87] Pycwt*: Continuous wavelet transform library for python*, https://github.com/Unidata/pyCWT.

[88] M. Giesler, M. Isi, M. A. Scheel, and S. A. Teukolsky, "Black hole ringdown: The importance of overtones," *Physical Review X*, vol. 9, no. 4, Dec. 2019.

[89] E. Newman and R. Penrose, "An Approach to gravitational radiation by a method of spin coefficients," *J.Math.Phys.*, vol. 3, pp. 566–578, 1962.

[90] D. Müller, J. Grigsby, and B. Brügmann, "Dynamical shift condition for unequal mass black hole binaries," *Physical Review D*, vol. 82, no. 6, p. 064 004, Sep. 2010.

[91] C. Cutler and É. E. Flanagan, "Gravitational waves from merging compact binaries: How accurately can one extract the binary's parameters from the inspiral waveform?" *Physical Review D*, vol. 49, no. 6, pp. 2658–2697, Mar. 1994.

[92] B. P. Abbott *et al.*, "A guide to LIGO–virgo detector noise and extraction of transient gravitational-wave signals," *Classical and Quantum Gravity*, vol. 37, no. 5, p. 055 002, Feb. 2020.

[93] D. Shoemaker *et al.*, "Advanced ligo anticipated sensitivity curves," *LIGO-T0900288, https://dcc.ligo.org/cgi-bin/DocDB/ShowDocument?docid=2974*, 2010.

[94] K. Chatziioannou, R. Cotesta, S. Ghonge, J. Lange, K. K. Ng, J. C. Bustillo, J. Clark, C.-J. Haster, S. Khan, M. Pürrer, V. Raymond, S. Vitale, N. Afshari, S. Babak, K. Barkett, J. Blackman, A. Bohé, M. Boyle, A. Buonanno, M. Campanelli, G. Carullo, T. Chu, E. Flynn, H. Fong, A. Garcia, M. Giesler, M. Haney, M. Hannam, I. Harry, J. Healy, D. Hemberger, I. Hinder, K. Jani, B. Khamersa, L. E. Kidder, P. Kumar, P. Laguna, C. O. Lousto, G. Lovelace, T. B. Littenberg, L. London, M. Millhouse, L. K. Nuttall, F. Ohme, R. O'Shaughnessy, S. Ossokine, F. Pannarale, P. Schmidt, H. P. Pfeiffer, M. A. Scheel, L. Shao, D. Shoemaker, B. Szilagyi, A. Taracchini, S. A. Teukolsky, and Y. Zlochower, "On the properties of the massive binary black hole merger GW170729," *Physical Review D*, vol. 100, no. 10, Nov. 2019.

[95] T. A. Apostolatos, C. Cutler, G. J. Sussman, and K. S. Thorne, "Spin-induced orbital precession and its modulation of the gravitational waveforms from merging binaries," *prd*, vol. 49, pp. 6274–6297, 12 Jun. 1994.

[96] L. E. Kidder, "Coalescing binary systems of compact objects to (post)5/2-newtonian order. v. spin effects," *Physical Review D*, vol. 52, no. 2, pp. 821–847, Jul. 1995.

[97] S. Gezari, D. C. Martin, B. Milliard, S. Basa, J. P. Halpern, K. Forster, P. G. Friedman, P. Morrissey, S. G. Neff, D. Schiminovich, M. Seibert, T. Small, and T. K. Wyder, "Ultraviolet Detection of the Tidal Disruption of a Star by a Supermassive Black Hole," *The Astrophysical Journal Letters*, vol. 653, no. 1, p. L25, 2006.

[98] S. Gezari, S. Basa, D. C. Martin, G. Bazin, K. Forster, B. Milliard, J. P. Halpern, P. G. Friedman, P. Morrissey, S. G. Neff, D. Schiminovich, M. Seibert, T. Small, and T. K. Wyder, "UV/Optical Detections of Candidate Tidal Disruption Events by GALEX and CFHTLS," *The Astrophysical Journal*, vol. 676, no. 2, p. 944, 2008.

[99] S. Gezari, T. Heckman, S. B. Cenko, M. Eracleous, K. Forster, T. S. Gonçalves, D. C. Martin, P. Morrissey, S. G. Neff, M. Seibert, D. Schiminovich, and T. K.

Wyder, "Luminous Thermal Flares from Quiescent Supermassive Black Holes," *The Astrophysical Journal*, vol. 698, no. 2, p. 1367, 2009.

[100] S. Gezari, R. Chornock, A. Rest, M. E. Huber, K. Forster, E. Berger, P. J. Challis, J. D. Neill, D. C. Martin, T. Heckman, A. Lawrence, C. Norman, G. Narayan, R. J. Foley, G. H. Marion, D. Scolnic, L. Chomiuk, A. Soderberg, K. Smith, R. P. Kirshner, A. G. Riess, S. J. Smartt, C. W. Stubbs, J. L. Tonry, W. M. Wood-Vasey, W. S. Burgett, K. C. Chambers, T. Grav, J. N. Heasley, N. Kaiser, R.-P. Kudritzki, E. A. Magnier, J. S. Morgan, and P. A. Price, "An ultraviolet–optical flare from the tidal disruption of a helium-rich stellar core," *Nature*, vol. 485, no. 7397, pp. 217–220, May 2012.

[101] W. P. Maksym, M. P. Ulmer, and M. Eracleous, "A tidal disruption flare in A1689 from an archival X-ray survey of galaxy clusters," *The Astrophysical Journal*, vol. 722, no. 2, pp. 1035–1050, Sep. 2010.

[102] J. K. Cannizzo, E. Troja, and G. Lodato, "GRB 110328A/Swift J164449.3+573451: The Tidal Obliteration of a Deeply Plunging Star?" *The Astrophysical Journal*, vol. 742, no. 1, p. 32, 2011.

[103] S. B. Cenko, H. A. Krimm, A. Horesh, A. Rau, D. A. Frail, J. A. Kennea, A. J. Levan, S. T. Holland, N. R. Butler, R. M. Quimby, J. S. Bloom, A. V. Filippenko, A. Gal-Yam, J. Greiner, S. R. Kulkarni, E. O. Ofek, F. O. E, Patricia Schady, J. M. Silverman, N. R. Tanvir, and D. Xu, "Swift J2058.4+0516: Discovery of a Possible Second Relativistic Tidal Disruption Flare?" *The Astrophysical Journal*, vol. 753, no. 1, p. 77, 2012.

[104] W. P. Maksym, M. P. Ulmer, M. C. Eracleous, L. Guennou, and L. C. Ho, "A tidal flare candidate in Abell 1795," *Monthly Notices of the Royal Astronomical Society*, vol. 435, no. 3, pp. 1904–1927, Nov. 2013.

[105] D. Donato, S. B. Cenko, S. Covino, E. Troja, T. Pursimo, C. C. Cheung, O. Fox, A. Kutyrev, S. Campana, D. Fugazza, H. Landt, and N. R. Butler, "A Tidal Disruption Event in a nearby Galaxy Hosting an Intermediate Mass Black Hole," *The Astrophysical Journal*, vol. 781, no. 2, p. 59, 2014.

[106] S. van Velzen, G. R. Farrar, S. Gezari, N. Morrell, D. Zaritsky, L. Östman, Mathew Smith, J. Gelfand, and A. J. Drake, "Optical Discovery of Probable Stellar Tidal Disruption Flares," *The Astrophysical Journal*, vol. 741, no. 2, p. 73, 2011.

[107] I. Arcavi, A. Gal-Yam, M. Sullivan, Y.-C. Pan, S. B. Cenko, A. Horesh, E. O. Ofek, A. D. Cia, L. Yan, C.-W. Yang, D. A. Howell, D. Tal, S. R. Kulkarni, S. P. Tendulkar, S. Tang, D. Xu, A. Sternberg, J. G. Cohen, J. S. Bloom, P. E. Nugent, M. M. Kasliwal, D. A. Perley, R. M. Quimby, A. A. Miller, C. A. Theissen, and R. R. Laher, "A

Continuum of H- to He-rich Tidal Disruption Candidates With a Preference for E+A Galaxies," *The Astrophysical Journal*, vol. 793, no. 1, p. 38, 2014.

[108] S. van Velzen, G. E. Anderson, N. C. Stone, M. Fraser, T. Wevers, B. D. Metzger, P. G. Jonker, A. J. van der Horst, T. D. Staley, A. J. Mendez, J. C. A. Miller-Jones, S. T. Hodgkin, H. C. Campbell, and R. P. Fender, "A radio jet from the optical and x-ray bright stellar tidal disruption flare ASASSN-14li," *Science*, vol. 351, no. 6268, pp. 62–65, Jan. 2016.

[109] R. Chornock, E. Berger, S. Gezari, B. A. Zauderer, A. Rest, L. Chomiuk, A. Kamble, A. M. Soderberg, I. Czekala, J. Dittmann, M. Drout, R. J. Foley, W. Fong, M. E. Huber, R. P. Kirshner, A. Lawrence, R. Lunnan, G. H. Marion, G. Narayan, A. G. Riess, K. C. Roth, N. E. Sanders, D. Scolnic, S. J. Smartt, K. Smith, C. W. Stubbs, J. L. Tonry, W. S. Burgett, K. C. Chambers, H. Flewelling, K. W. Hodapp, N. Kaiser, E. A. Magnier, D. C. Martin, J. D. Neill, P. A. Price, and R. Wainscoat, "The Ultraviolet-bright, Slowly Declining Transient PS1-11af as a Partial Tidal Disruption Event," *The Astrophysical Journal*, vol. 780, no. 1, p. 44, 2014.

[110] M. J. Rees, "Tidal disruption of stars by black holes of 10 to the 6th-10 to the 8th solar masses in nearby galaxies," *Nature*, vol. 333, pp. 523–528, Jun. 1988.

[111] E. S. Phinney, "Manifestations of a Massive Black Hole in the Galactic Center," in *The Center of the Galaxy*, M. Morris, Ed., ser. International Astronomical Union Union Astronomique Internationale, Springer Netherlands, 1989, pp. 543–553, ISBN: 978-94-009-2362-1.

[112] C. R. Evans and C. S. Kochanek, "The tidal disruption of a star by a massive black hole," *The Astrophysical Journal Letters*, vol. 346, pp. L13–L16, Nov. 1989.

[113] J. Magorrian and S. Tremaine, "Rates of tidal disruption of stars by massive central black holes," *Monthly Notices of the Royal Astronomical Society*, vol. 309, no. 2, pp. 447–460, Oct. 1999.

[114] B. Carter and J.-P. Luminet, "Tidal compression of a star by a large black hole. I Mechanical evolution and nuclear energy release by proton capture," *Astronomy and Astrophysics*, vol. 121, pp. 97–113, May 1983.

[115] J.-P. Luminet and B. Carter, "Dynamics of an affine star model in a black hole tidal field," *The Astrophysical Journal Supplement Series*, vol. 61, pp. 219–248, Jun. 1986.

[116] J.-P. Luminet and B. Pichon, "Tidal pinching of white dwarfs," *Astronomy and Astrophysics*, vol. 209, pp. 103–110, Jan. 1989.

[117] N. C. Stone, M. Kesden, R. M. Cheng, and S. van Velzen, "Stellar tidal disruption events in general relativity," *General Relativity and Gravitation*, vol. 51, no. 2, p. 30, Feb. 2019.

[118] P. Laguna, W. A. Miller, W. H. Zurek, and M. B. Davies, "Tidal disruptions by supermassive black holes - Hydrodynamic evolution of stars on a Schwarzschild background," *The Astrophysical Journal Letters*, vol. 410, pp. L83–L86, Jun. 1993.

[119] S. Rosswog, E. Ramirez-Ruiz, and W. R. Hix, "Tidally-induced thermonuclear supernovae," *Journal of Physics: Conference Series*, vol. 172, no. 1, p. 012 036, 2009.

[120] G. Lodato, A. R. King, and J. E. Pringle, "Stellar disruption by a supermassive black hole: Is the light curve really proportional to t-5/3?" *Monthly Notices of the Royal Astronomical Society*, vol. 392, no. 1, pp. 332–340, Jan. 2009.

[121] S. Kobayashi, P. Laguna, E. S. Phinney, and P. Mészáros, "Gravitational Waves and X-Ray Signals from Stellar Disruption by a Massive Black Hole," *The Astrophysical Journal*, vol. 615, no. 2, p. 855, Nov. 2004.

[122] K. Kagaya, S. Yoshida, and A. Tanikawa, "Tidal disruptions of rotating stars by a supermassive black hole," *arXiv:1901.05644 [astro-ph]*, Jan. 2019. arXiv: 1901.05644 [astro-ph].

[123] E. C. A. Golightly, E. R. Coughlin, and C. J. Nixon, "Tidal Disruption Events: The Role of Stellar Spin," *The Astrophysical Journal*, vol. 872, no. 2, p. 163, Feb. 2019.

[124] J. Guillochon and M. McCourt, "Simulations of Magnetic Fields in Tidally Disrupted Stars," *The Astrophysical Journal Letters*, vol. 834, no. 2, p. L19, 2017.

[125] P. Anninos, P. C. Fragile, S. S. Olivier, R. Hoffman, B. Mishra, and K. Camarda, "Relativistic Tidal Disruption and Nuclear Ignition of White Dwarf Stars by Intermediate-mass Black Holes," *The Astrophysical Journal*, vol. 865, no. 1, p. 3, Sep. 2018.

[126] G. M. Volkoff and J. R. Oppenheimer, "On Massive Neutron Cores," *Physical Review*, vol. 55, no. 4, pp. 374–381, Feb. 1939.

[127] N. Stergioulas and J. L. Friedman, "Comparing models of rapidly rotating relativistic stars constructed by two numerical methods," *The Astrophysical Journal*, vol. 444, pp. 306–311, May 1995.

[128] N. Stergioulas, "The Structure and Stability of Rotating Relativistic Stars," *Ph.D. Thesis*, Jan. 1996.

[129] ——, *RNS*.

[130] Z. B. Etienne, T. W. Baumgarte, and I. Ruchlin, "$\Mathrm{SENR}/\mathrm{NRPy}+$: Numerical relativity in singular curvilinear coordinate systems," *Physical Review D*, vol. 97, no. 6, p. 064 036, Mar. 2018.

[131] M. Clark, "Bowen-type initial data for simulations of neutron stars in binary systems," Doctoral Dissertation, Georgia Institute of Technology, Atlanta, Georgia, May 2016.

[132] G. B. Cook, S. L. Shapiro, and S. A. Teukolsky, "Rapidly rotating polytropes in general relativity," *The Astrophysical Journal*, vol. 422, pp. 227–242, Feb. 1994.

[133] C. Ridders, "A new algorithm for computing a single root of a real continuous function," *IEEE Transactions on Circuits and Systems*, vol. 26, no. 11, pp. 979–980, Nov. 1979.

[134] J. L. Friedman, J. R. Ipser, and L. Parker, "Rapidly Rotating Neutron Star Models," *The Astrophysical Journal*, vol. 304, p. 115, May 1986.

[135] M. Alcubierre, *Introduction to 3+1 Numerical Relativity*, 1st ed., ser. International Series of Monographs on Physics 140. New York: Oxford University Press, Jun. 2008, ISBN: 978-0-19-920567-7.

[136] M. Thierfelder, "Numerical Simulations of Neutron Stars in General Relativistic Hydrodynamics," Doctoral Dissertation, Friedrich Schiller University Jena, Jena, Thuringia, Germany, Dec. 2011.

[137] J. Guillochon and E. Ramirez-Ruiz, "Hydrodynamical simulations to determine the feeding rate of black holes by the tidal disruption of stars: The importance of the impact parameter and stellar structure," *The Astrophysical Journal*, vol. 767, no. 1, p. 25, Mar. 2013.

[138] G. T. van Belle, "Interferometric observations of rapidly rotating stars," *The Astronomy and Astrophysics Review*, vol. 20, no. 1, p. 51, Mar. 2012.

[139] T. Alexander and P. Kumar, "Tidal Spin-up of Stars in Dense Stellar Cusps around Massive Black Holes," *The Astrophysical Journal*, vol. 549, no. 2, p. 948, Mar. 2001.

[140] R. Cen, "On Post-starburst Galaxies Dominating Tidal Disruption Events," *The Astrophysical Journal*, vol. 888, no. 1, p. L14, Jan. 2020.

[141] J. Guillochon and E. Ramirez-Ruiz, "A Dark Year for Tidal Disruption Events," *The Astrophysical Journal*, vol. 809, no. 2, p. 166, 2015.

[142] J. Guillochon, H. Manukian, and E. Ramirez-Ruiz, "PS1-10jh: The Disruption of a Main-Sequence Star of Near-Solar Composition," *The Astrophysical Journal*, vol. 783, no. 1, p. 23, Feb. 2014.

[143] R. Fitzpatrick, *An Introduction to Celestial Mechanics*. New York: Cambridge University Press, 2012, ISBN: 978-1-107-02381-9.

[144] C. Bonnerot, E. M. Rossi, and G. Lodato, "Long-term stream evolution in tidal disruption events," *Monthly Notices of the Royal Astronomical Society*, vol. 464, no. 3, pp. 2816–2830, Jan. 2017.